Université catholique de Louvain
Faculté de Médecine
Pôle d'Imagerie Moléculaire, Radiothérapie et Oncologie

Université de Douala
Faculté des Sciences
Centre de Physique Atomique Moléculaire et Optique Quantique

CLINICAL EVALUATION OF FAST ELECTRON MONTE CARLO DOSE CALCULATION ALGORITHMS FOR TREATMENT PLANNING SYSTEMS:

VALIDATION WITH EXPERIMENTAL MEASUREMENTS AND EGSnrc MONTE CARLO SIMULATION

Paul EDIMO

September 11
2012

Dissertation submitted in fulfillment of the requirements for the Degree of "Docteur en Sciences Médicales – Orientation : Physique Médicale"

Promoter
Prof. Stefaan Vynckier — Université catholique de Louvain

Co-Promoter
Prof. Moïse Kwato Njock — Université de Douala

Promoter

Prof. Stefaan Vynckier	Université catholique de Louvain

Co-Promoter

Prof. Moïse Kwato Njock	Université de Douala, Cameroun

Doctoral guidance committee

Prof. Stefaan Vynckier	Université catholique de Louvain
Prof. Moïse Kwato Njock	Université de Douala, Cameroun
Prof. Pierre Scalliet	Université catholique de Louvain
Prof. Vincent Grégoire	Université catholique de Louvain
Prof. Bernard Piraux	Université catholique de Louvain
Dr. Nick Reynaert	Centre Oscar Lambret, Lille-France

President of the examination committee

Prof. Vincent Grégoire	Université catholique de Louvain

Examination committee

Prof. Stefaan Vynckier	Université catholique de Louvain
Prof. Moïse Kwato Njock	Université de Douala, Cameroun
Prof. Pierre Scalliet	Université catholique de Louvain
Prof. Bernard Piraux	Université catholique de Louvain
Prof. Carlos De Wagter	Université de Gand
Dr. Nick Reynaert	Centre Oscar Lambret, Lille-France

TABLE OF CONTENTS

Acknowledgments v
Dedication ix
Abstract xi
Résumé xv
List of abbreviations xix
list of figures xxvi
list of tables xxviii

1 Introduction **1**
1.1 Brief History 1
1.2 Outline of the thesis 2
1.3 Quality assurance and Quality control for TPSs 3
1.3.1 Quality assurance 3
1.3.2 Quality control 4
1.4 Brief overview of the problematic of electron dose calculation 4
1.5 Thesis organization 6
1.6 **Bibliography** 7

2 Theory **11**
2.1 Radiation interaction with matter 11
2.1.1 Photon interactions 11
2.1.2 Attenuation coefficients 15
2.1.3 Electron interactions 16
2.2 Stopping power 19

2.3 Radiation dosimetry 20
2.3.1 Particle fluence and Energy fluence 20
2.3.2 Kerma (Indirectly ionizing radiations) 21
2.3.3 Energy fluence and kerma (Photons) 22
2.3.4 Cema (Directly ionizing radiations) 23
2.3.5 Absorbed dose 23
2.3.6 Kerma and dose (Charge Particle Equilibrium) 24
2.3.7 Cema and dose (Electrons) 24
2.3.8 Fluence and dose (Electrons) 25
2.4 Electron beam characteristics 25
2.4.1 General shape of depth dose curve 26
2.4.2 Beam quality index specification 28
2.4.3 Beam energy determination 29
2.4.4 Output factors for electron beams 30
2.4.5 Profiles and off-axis ratios 31
2.4.6 Flatness and symmetry 31
2.5 Radiation TPP: A step by step description 32
2.5.1 Volume definition 32
2.5.2 Steps in the radiation therapy planning process 34
2.6 Dose calculation algorithms 37
2.6.1 Convolution/superposition (Photons) 37
2.6.2 Pencil beam algorithms (Electrons) 38
2.6.3 Generalized Pencil beam algorithms 45
2.7 MC simulation in radiation therapy 45
2.7.1 Photon transport 48
2.7.2 Electron transport mechanism 50
2.8 General Purpose MC in radiation therapy 50
2.8.1 EGS user code 50
2.8.2 BEAMnrc 51
2.8.3 PENELOPE 52
2.8.4 GEANT4 53
2.9 Fast MC dose calculation engine for TPS 53

2.9.1 Voxel MC (VMC) . . . 53
2.9.2 X-ray Voxel MC (XVMC) . . . 56
2.9.3 VMC++ . . . 56
2.10 **Bibliography** . . . 58

3 Publication 1: Evaluation of a commercial VMC++ MC-based TPS 63
3.1 Introduction . . . 65
3.2 Materials and methods . . . 67
3.2.1 Dosimetry measurement . . . 67
3.2.2 Monte Carlo simulation . . . 70
3.2.3 Oncentra MasterPlan dose calculation . . . 74
3.3 Results . . . 76
3.3.1 Homogeneous water phantom calculations . . . 76
3.3.2 Heterogeneous thorax phantom calculations . . . 80
3.4 Discussion . . . 84
3.5 Conclusions . . . 86
3.6 **Bibliography** . . . 89

4 Publication 2: Validation of XiO eMC-based TPS 93
4.1 Introduction . . . 95
4.2 Materials and methods . . . 96
4.2.1 Measurements . . . 96
4.2.2 Monte Carlo simulations . . . 98
4.2.3 XiO Electron Monte Carlo dose calculation . . . 99
4.2.4 User control parameters affecting the accuracy of XiO eMC dose calculation . . . 102
4.3 Results . . . 102
4.3.1 Homogeneous water phantom calculations . . . 102
4.3.2 Heterogeneous thorax phantom calculations . . . 108
4.4 Discussion and conclusion . . . 115
4.5 **Bibliography** . . . 119

5 Discussion-conclusion and Future prospects 123
5.1 Discussion 123
5.1.1 Homogeneous water phantom validation 124
5.1.2 Heterogeneous phantom validation 125
5.1.3 Hounsfield values to relative electron densities conversion file 127
5.1.4 Measurements with KODAK EDR2 film 128
5.2 Conclusion 129
5.3 Future prospects 129
5.4 **Bibliography** 131

Acknowledgments

The work described in this thesis has been performed under the co-supervision of the Université catholique de Louvain (UCL, Belgium) and the CEPAMOQ Centre of the University of Douala (Cameroon). All measurements have been carried out on an ELEKTA SL25 medical linear accelerator in the Radiotherapy Department of Saint-Luc University Hospital.

First of all, I would like to express my sincere gratitude to my Ph.D. advisors, **Prof. Stefaan Vynckier** and **Prof. M. G. Kwato Njock** for their supervision, support, interest and help during the course of this project.

The UCL department of radiotherapy, with advanced equipments and strong scientific background, is an excellent treatment centre. I would like to acknowledge Prof. Pierre Scalliet and Prof. Vincent Grégoire for welcoming me in University Saint-Luc Hospital and helping when I needed it the most.

Special thanks to all the examination committee members who agreed to evaluate this work, namely: Prof. Vincent Grégoire, Prof. Stefaan Vynckier, Prof. Moïse Kwato Njock, Prof. Pierre Scalliet, Prof. Bernard Piraux, Prof. Carlos De Wagter and Dr. Nick Reynaert.

This work was partly supported by The Abdus Salam International Centre for Theoretical Physics (ICTP, Trieste-Italy) through CEPAMOQ (OEA-project-71) at the University of Douala (Cameroon) and the Fellowships

Program of the "Agence Universitaire de la Francophonie (AUF)". I sincerely appreciate the financial support from these two organizations.

I would also like to thank all the physicists and engineering teammates who gave me great support whenever I needed it. For the physics team, I would like to express my warmest thanks to Jean-Marc Denis and Antoine Delor for their technical help in the measurements performed in the water phantom. For the engenering team, my keen appreciation goes to Vincent Roosen, Simon Vanderbrecht and especially, Maxime Coevoet for their technical support during the entire work.

Special thanks to all my family, particularly my dad, mom and uncle, **Michel Ndjocke**, **Rosine Moukoussa** and **Eugène Ndjaka II**, respectively, for supporting me (I should say "suffering for me"). I am also indebted to my two elder sisters, **Grâce** and **Félicité**, who gave me their fraternal framing throughout my studies. I also warmly appreciate the generosity and understanding of my extended family.

Special thanks of course to my colleagues in my office who have already defended their Ph.D. thesis, namely: Dr. Fadi Abboud and Dr. Edmond Sterpin. I had some constructive discussions with them during the entire work.

Furthermore, I also cannot escape from acknowledging all my colleagues of the CEPAMOQ Centre, namely: Dr. Celsius Bouri, Dr. Alix Dehayem, Dr. Brice Malonda, Dr. Falama Souley, Dr. Marcel Ngoko, Dr. Saidou, Dr. Olivier Waffeu and Dr. Yvette Siaka. I am thinking of the years in M.Sc. program we followed together under an atmosphere of conviviality and fraternity.

Finally, I would like to express special thanks to my wife **Clémentine Sibomana**. She always kept me away from some of my family responsi-

bilities, encouraged me to concentrate on completing this dissertation and she was the first level of revising this manuscript. To end, this research experience was nothing compared to the pleasure of sharing each day of my life with her.

Thesis submitted in fulfillment of the requirements for the degree of "Docteur en Sciences Médicales - Orientation : Physique Médicale" - september 11, 2012.

Michel Edimo

&

Kevin G. Sibomana

Abstract

The goal of radiotherapy is to deliver enough radiation to the target volume while maintaining the dose to surrounding healthy tissues as low as possible. The International Commission on Radiation Units and Measurements (ICRU) recommends a target dose uniformity within +7% and -5% of the dose delivered to a well defined prescription point within the target. The radiation treatment planning process consists of many steps and each step introduces an uncertainty and errors carried through the entire treatment process. In this context, the accuracy of the dose calculation engine implemented in the treatment planning system (TPS) plays an important role to achieve the above objective. The electron beam dose distributions calculated in the presence of inhomogeneous tissue is still challenging due to the limitations of analytical algorithms to accurately compute dose distribution in the heterogeneous media. Pencil beam algorithms which are the most popular electron dose calculation engine implemented into TPSs have some limitations in the dose calculation when tissues inhomogeneities such as bone, lung and air cavities are encountered within the treatment volume and, in the interface of tissues of different densities (e.g. of interface tissues-air cavities). This is essentially due to changes in electrons scattering properties of the above different tissues. Monte Carlo (MC) methods in radiation therapy have been shown to be the must accurate way for computing radiotherapy dose. In the past, however, the available computer power has been the major drawback for the clinical implementation of full MC simulations in clinical practice. This led to the development of "fast MC" algorithms

Thesis submitted in fulfillment of the requirements for the degree of "Docteur en Sciences Médicales - Orientation : Physique Médicale" - september 11, 2012.

which implement several approximations and simplifications to speed up the calculations. The clinical implementation of such MC based TPSs involves design compromises with a possibility of error. It is important, therefore, to perform independent validation under conditions similar to those found in the clinic.

In the present study, we present the clinical validation of the two commercial electron MC based TPS, Oncentra MasterPlan TPS (OMTPS) and XiO eMC. We present a new approach on the commissioning process based on, (a) homogeneous water phantom validation, (b) heterogeneous phantom validation with film measurements and, (c) Full MC validation.

As a first step, MC models of electron beams (4, 8, 12 and 18 MeV) from an Elekta SL25 medical linear accelerator were build using the popular EGSnrc/BEAMnrc user MC code. The calculated dose distributions were benchmarked by a comparison with the measurements made in the water phantom for a wide range of open field size and insert combination, at a single source to surface distance (SSD) of 100 cm. These BEAMnrc models were used to evaluate the accuracy of OMTPS (respectively XiO eMC) for two energies 4 and 12 MeV (respectively for 4, 8, 12 and 18 MeV) in a homogeneous water phantom. Moreover, output factors were measured in the water phantom and compared against BEAMnrc simulation, OMTPS and XiO eMC calculations. In the must cases, the overall agreement between predicted and measured output factors was comparable between BEAMnrc simulation and OMTPS on the one hand, and between BEAMnrc simulation and XiO eMC on the other hand, except for a few asymmetric and/or small insert cutouts, where larger deviations were recorded.

As a second step, the accuracy of both TPSs has been evaluated by comparing dose distributions in a heterogeneous phantom containing ribs structures. Dose distributions in the lung and non-lung tissue predicted from BEAMnrc simulation were compared with those computed with OMTPS and XiO eMC. In the case of OMTPS calculations, differences between BEAMnrc simulation and measurements range from 0.5%-2.0% between two ribs and 0.6%-1.0% below the ribs, whereas the range difference between OMTPS

and measurements was the same (0.5-4.0%) in both areas. BEAMnrc models have been set as reference in the case of XiO eMC computation and the overall agreement between the two schemes lies under 2.5% for the most tested dose distributions at 8, 12 and 18 MeV and is better than the 4 MeV one. At this lower energy, BEAMnrc and XiO eMC results exhibit percent deviations from 2.0 to 3.5% between two ribs as well as below the ribs. Calculations performed with several voxel sizes shown that the accuracy of XiO eMC increases when voxel size decreases. Large deviations (discrepancies up to 4.5% between two ribs as well as beneath the ribs) between BEAMnrc and XiO eMC have been found for calculations performed with voxel sizes of $0.45\times0.45\times0.45$ cm^3 and $0.55\times0.55\times0.55$ cm^3 for all energies involved.
The present work demonstrates the added value of MC TPS compared to pencil beam algorithms. Results show that OMTPS and XiO eMC can predict dose perturbation induced by high-density heterogeneities for the electron beam energies investigated, except at 4 MeV electron beam energy in which significant deviations have been found with both algorithms. This demonstrates that caution is necessary in using both TPSs at low energies.

Résumé

L'objectif de la radiothérapie est de détruire les cellules cancéreuses (cellules tumorales) par irradiation en bloquant leur capacité à se multiplier tout en épargnant les tissus sains périphériques. La Commission internationale des unités et mesures radiologiques (ICRU) recommande une uniformité entre +7% et -5% de la dose prescrite en un point bien défini dans le volume cible. Le processus de planification de traitement en radiothérapie se subdivise en plusieurs étapes et chacune de ces étapes introduit une incertitude et des erreurs qui s'accumulent sur l'incertitude globale sur la dose délivrée durant tout le processus de traitement. Dans ce contexte, la précision des algorithmes de calcul de dose mis en œuvre dans les systèmes de planification de traitement (TPS) joue un rôle important pour atteindre l'objectif ci-dessus. Le calcul prévisionnel des distributions de dose avec les faisceaux d'électrons en présence des hétérogénéités reste toujours un défi en raison des limitations que présentent les algorithmes analytiques pour calculer la dose dans un milieu hétérogène. Les algorithmes de type "Pencil beam" qui sont généralement les plus utilisés dans les TPSs pour le calcul de distribution de dose avec les faisceaux d'électrons présentent des limitations lorsque les hétérogénéités telles que les structures osseuses, les poumons et les cavités d'air sont rencontrés dans le volume cible à traiter et, aux interfaces des tissus de densités différentes (par exemple aux interfaces tissus-cavités d'air). Cela est essentiellement dû au fait que ces différents tissus ont des propriétés différentes dans la diffusion des électrons. Les calculs Monte Carlo (MC) se sont révélés être la technique la plus précise pour le calcul de distri-

Thesis submitted in fulfillment of the requirements for the degree of "Docteur en Sciences Médicales - Orientation : Physique Médicale" - september 11, 2012.

bution de dose en radiothérapie. Par le passée, la puissance des ordinateurs disponibles ne permettait pas l'intégration de ces algorithmes dans les TPSs pour le calcul de dose en routine clinique. Cela a conduit au développement des algorithmes de type MC rapides "Fast MC" qui mettent en œuvre plusieurs approximations et simplifications visant à accélérer la vitesse des calculs. La mise en œuvre clinique de tels TPSs implique donc des compromis de conception avec une possibilité d'erreur. Il est donc important de procéder à leur validation dans les conditions similaires à celles rencontrées en routine clinique.

Ce travail porte sur la validation clinique de deux TPSs pour les faisceaux d'électrons, Oncentra MasterPlan TPS (OMTPS) et XiO eMC. Nous présentons une nouvelle approche dans ce processus de commissionnement basé sur, (a) la validation dans un fantôme homogène d'eau, (b) la validation dans un fantôme hétérogène simulant la paroi thoracique du patient à partir des mesures effectuées avec les films dosimétriques et, (c) La validation par simulation MC complète.

Dans un premier temps, les modèles MC de faisceaux d'électrons (4, 8, 12 et 18 MeV) générés par un accélérateur linéaire médical Elekta SL25 ont été construits en utilisant le code EGSnrc/BEAMnrc. Les distributions de dose calculées avec ces modèles ont été validées par comparaison avec les mesures effectuées dans le fantôme d'eau pour plusieurs tailles du champ ouverts et plusieurs "inserts" à une distance source surface (SSD) de 100 cm. Ces modèles ont été utilisés pour évaluer la précision des calculs des deux TPSs, OMTPS (respectivement XiO eMC) pour les deux énergies de 4 et 12 MeV (respectivement de 4, 8, 12 et 18 MeV) dans un fantôme d'eau homogène. En outre, les "facteurs output" ont été mesurés dans l'eau et comparés à ceux prédits par les modèles MC (BEAMnrc) et les deux TPSs (OMTPS, XiO eMC). Dans la plus part des cas, l'accord global entre les "facteurs output" calculés et mesurés était comparable entre les prévisions des modèles MC et le TPS OMTPS d'une part, et entre les prévisions des modèles MC et le TPS XiO eMC d'autre part, à l'exception de quelques petits "inserts" et/ou les "inserts" asymétriques pour lesquels de grandes déviations ont été

enregistrées.
Dans un deuxième temps, la précision de calcul des deux TPSs a été évaluée en comparant les distributions de dose dans un fantôme hétérogène contenant des structures osseuses (côtes). La distribution de dose dans les poumons et dans d'autres tissus non pulmonaires, prédite à partir des modèles MC a été comparée avec celle calculée avec les deux TPSs, OMTPS et XiO eMC. Dans le cas des calculs avec OMTPS, les différences entre les modèles MC et les mesures varient entre 0.5%-2.0% entre deux côtes et 0.6%-1.0% en dessous des côtes, tandis que les différences entre OMTPS et les mesures sont les mêmes (0.5-4.0%) dans les deux zones. Les modèles MC ont été fixés comme référence pour les calculs avec XiO eMC et l'accord global entre les deux régions se situe en dessous de 2.5% pour la plupart des distributions de dose étudiées pour les énergies de 8, 12 et 18 MeV. Les résultats sont moins bons à 4 MeV, i.e. à basse énergie. Pour cette énergie, les calculs avec les modèles MC et ceux obtenus avec le TPS XiO eMC présentent des déviations de 2.0 à 3.5% aussi bien entre deux côtes qu'en dessous des côtes. Les calculs effectués avec plusieurs tailles de "voxel" ont montré que la précision de calcul de XiO eMC augmente lorsque la taille de "voxel" diminue. De grandes déviations (écarts jusqu'à 4.5%) aussi bien entre deux côtes qu'en dessous des côtes ont été observées entre les modèles MC et le TPS XiO eMC avec des tailles de "voxel" de 0.45×0.45×0.45 cm^3 et 0.55× 0.55×0.55 cm^3 pour toutes les énergies étudiées.
Ce travail démontre la valeur ajoutée des algorithmes MC mis en œuvre dans les TPSs par rapport aux algorithmes de type "pencil beam". Les différents résultats montrent clairement que les deux TPSs, OMTPS et XiO eMC peuvent prédire les perturbations de la dose induite par la présence des hétérogénéités de haute densité pour les énergies de faisceaux d'électrons étudiées. Cependant, les écarts significatifs trouvés avec ces deux TPSs à l'énergie de 4 MeV montrent qu'une prudence doit être de mise dans l'utilisation de ces deux TPSs à basse énergie.

List of abbreviations

3D	Three-Dimensional
BCA	Boundary Crossing Algorithm
BEAMnrc	an EGSnrc/PRESTAII Monte Carlo user code
CH	Condensed History
CM	Component Module
CPE	Charged-Particle Equilibrium
C/S	Convolution/Superposition
CPU	Central Processing Unit
CTV	Clinical Target Volume
DCS	Differential Cross-Section
DOSXYZnrc	an EGSnrc-based Monte Carlo simulation code
DVH	Dose-Volume Histogram
ECMSSG	ELEKTA CMS SOFTWARE group
eMC	electron Monte Carlo
EGS	Electron Gamma Shower (a Monte Carlo code)
FWHM	Full Width at Half Maximum
GEANT4	GEometry ANd Tracking (a Monte Carlo code, version 4)
GPBA	Generalize Pencil beam algorithm
GTV	Gross Tumor Volume
ICRU	International Commission on Radiation Units and Measurements
ICTP	International Centre for Theoretical Physics
IEC	International Electrotechnical Commission

ITV	Internal target volume
MC	Monte Carlo
MU	Monitor Unit
NCS	Netherlands Commission on Radiation Dosimetry
NTCP	Normal Tissues Control Probabilities
NRC	National Research Council of Canada
OAR	Organ At Risk
OMTPS	Oncentra MasterPlan Treatment Planning System
OF	Output factor
PBA	Pencil Beam Algorithm
PDD	Percentage depth dose
PC	Personal Computer
PMMA	Polymethyl Methacrylate
PENELOPE	PENetration and Energy LOss of Positron and Electrons
PDF	Probability Distribution Function
PTV	Planning Target Volume
QA	Quality Assurance
QC	Quality Control
SAD	Source Axis Distance
SSD	Source Surface Distance
TCPE	Transient Charged-Particle Equilibrium
TPP	Treatment Planning Process
TPS	Treatment Planning System
TCP	Tumor Control Probabilities
VMC	Voxel Monte Carlo (MC algorithm for electrons)
VMC++	MC algorithm based on VMC and XVMC
XVMC	MC algorithm for photons based on VMC

List of Figures

2.1 Schematic representation of the photoelectric process. In this diagram, the incoming photon ejects the photoelectron, followed by the movement of an outer orbital electron (from the L or M shell) into the vacancy created. A florescent photon is emitted with an energy K_α or K_β if the electron filling the vacancy comes from the L or M shell, respectively. 12

2.2 Representation of partial and total mass attenuation coefficients for two materials as function of energy: water on the left and lead on the right (from Salvat et *al.* [1]). 16

2.3 Representation of Coulomb interaction between an electron with mass m_e, velocity v and charge e^- and an atom. b is the impact parameter, a is the atomic radius and θ the scattering angle. 18

2.4 Typical electron PDD curve illustrating the definition of R_q, R_p, R_{100}, R_{50}, D_x, D_s and R_{90} for a 8 MeV electron beam from an ELEKTA SL25 medical linear accelerator. Field zise 10×10 cm^2 at a SSD of 100 cm. 27

2.5 Central axis depth dose curves from an ELEKTA SL25 Medical linear accelerator. Field size 10×10 cm^2, energies (starting from left to right) 4, 8, 12 and 18 MeV for a 100 cm SSD. The normalization has been performed at the depth of maximum dose along the central axis. 28

2.6 Illustration of the reference depth, Z_{ref} of a plane-parallel and cylindrical ionization chambers for the measurement of percentage depth ionization curve. 29

2.7 Representation of a typical dose profile for four field sizes of 6×6, 10×10, 14×14 and 20×20 cm^2 open applicator. The small profile corresponds to the 6×6 cm^2 field size. Electron beam energy is 8 MeV from an ELEKTA SL25 medical accelerator. 32

2.8 Representation of different volumes of interest and how they are related to each other (from P. Andreo et *al.*[12]), as defined in ICRU Reports No. 50 and 62 [17, 18]. 33

2.9 Illustration of the C/S method. The dose distribution is obtained from the primary energy fluence convolved with the pre-calculated MC kernels. 38

2.10 Representation of a broad beam into a matrix of a finite number of narrow discrete beams with Gaussian distribution in both space and angle 39

2.11 Schematic view of the Hogstrom PBA showing that it was modelling beam collimation, air gap (l_0) and internal patient heterogeneity (from Hogstrom et *al.* [24]). 40

2.12 Schematic representation in the x-z plane of a model electron beam incident on a stack of infinite slabs of different material. The configuration corresponds to those inhomogeneities underlying the central ray of the pencil beam drawn in figure 2.11. 42

2.13 Illustration of errors introduced by PBA models in the presence of inhomogeneities, from Nahum [27]. 46

3.1 Graphic representation of the thorax phantom. It consists of three layers of different tissue equivalent materials: adipose tissue (polyethylene, density 0.96 g/cm^3), striated muscle (PMMA, density 1.18 g/cm^3) in which a series of equidistant solid Teflon cylinders (simulating ribs), with a mass density of 2.13 g/cm^3 and an 8 mm diameter (center-to-center distance of 20 mm), are embedded. The third layer (16 cm-thick) is composed of cork material (cork, density 0.25 g/cm^3) simulating lung tissue. 69

3.2 Schematic representation of the MC model for the SL25 linear accelerator as simulated with the BEAMnrc code. Indicated are the exit window, primary scattering foil, primary collimator, secondary flattening foil, monitor chamber, mirror, upper and lower jaws, Mylar screen and applicator. The BEAMnrc CMs that were used in the model are given between brackets. 72

3.3 Central axis depth dose curves for 6×6 cm^2 (a), 10×10 cm^2 (b) and 20×20 cm^2 (c) field size for 4, 12 and 18 MeV at 100 cm SSD. Comparison between measurements (Meas) and treatment planning system (OMTPS) calculations (4 and 12 MeV) on the one hand and between Meas and BEAMnrc calculations (4, 12 and 18 MeV) on the other hand. Dose normalization is performed at the depth of maximum dose along the central axis. Agreement (difference between calculations and measurements) of R_{50} between each other was better than 1 mm. 77

3.4 Off-axis profiles (inplane direction, normalized at the central axis dose) for three open field sizes 6×6 cm^2, 10×10 cm^2 and 20×20 cm^2 at 100 cm SSD. Comparison between measurements (Meas), BEAMnrc simulation and treatment planning system (OMTPS) for 4 MeV electron beam energy (a), 12 MeV electron beam energy (b) and 18 MeV electron beam energy (c). The depth of comparison in the water phantom is the depth of maximum dose along the central axis and data were normalized at this depth. 79

3.5 Off-axis profiles (inplane direction) for an open field size of 6×6 cm^2 at 100 cm SSD. Comparison between measurements (Meas), BEAMnrc simulation and treatment planning system (OMTPS) for 12 MeV electron beam. Depth from the lung surface: 1 cm (a), 2 cm (b) and 3 cm (c). 85

3.6 Off-axis profiles (inplane direction) for an open field size of 6×6 cm^2 at 100 cm SSD. Comparison between measurements (Meas), BEAMnrc simulation and treatment planning system (OMTPS) for 4 MeV electron beam. Depth from the lung surface: 0.5 cm (a), 1 cm (b) and 1.5 cm (c). 87

4.1 Graphic representation of the thorax phantom. It consists of three layers of different tissue-equivalent materials: adipose tissue (polyethylene), striated muscle (PMMA) in which are embedded a series of seven equidistant solid Teflon (ribs), and lung tissue (cork). The radiation beam is interring on the top surface at 100 cm SSD and the beam axis is perpendicular to the central rib axis. 200 MU have been used for all computations and the statistical uncertainty was less than 1% for each calculation. 100

4.2 Central axis depth dose curves for 10×10 cm^2 (a) and 14×14 cm^2 (b) field size for 4, 8, 12 and 18 MeV at 100 cm SSD. Measurements (Meas) are compared to XiO TPS (XiO eMC) and BEAMnrc values. The normalization has been performed at the depth of maximum dose along the central axis. 105

4.3 Off-axis profiles (crossplane direction) for four open field sizes of 6×6 cm^2, 10×10 cm^2, 14×14 cm^2 and 20×20 cm^2 at 100 cm SSD. Comparison between measurements (Meas), BEAMnrc simulation and XiO eMC for 4 MeV (a) and 8 MeV (b) electron beam energies. The depth of comparison in the water phantom is the depth of maximum dose along the central axis. Data have been normalized at this depth. 106

4.4 Comparison of central axis depth dose curves in the heterogeneous phantom for 4 MeV (a) and 18 MeV (b). Field size 10×10 cm^2. Data have been normalized at the depth of maximum dose along the central axis for 4 MeV. For the 18 MeV, data have been normalized relative to the maximum dose along the central axis in the homogeneous water phantom of the corresponding field size. 109

4.5 Off-axis profiles in the muscle tissues (1.2 cm-thick of PMMA) in the crossplane direction at 100 cm SSD. Comparison between BEAMnrc simulation and XiO eMC for 8 MeV and 10×10 cm^2 field size (a), 12 MeV and 14×14 cm^2 field size (b). 114

4.6 Off-axis profiles in the lung tissue, in the crossplane direction for an open field size of 10×10 cm^2 at 100 cm SSD. XiO eMC and BEAMnrc are compared for 8 MeV electron beam energy. Depths from the lung surface are 0.6 cm (a) and 1.2 cm (b). . 115

5.1 Off-axis profiles in the crossplane direction for an open field size of 10×10 cm^2 at 100 cm SSD. PBA is compared to XiO eMC and BEAMnrc for 8 MeV electron beam energy in the non-lung tissue (1.2 cm-thick of PMMA) at -0.6 cm from the lung surface. 127

List of Tables

3.1 Energy spectrum parameters of electron beams used for the simulation. FWHM=full width at half maximum. Parameters of smaller peaks sometimes introduced in the spectrum are omitted here. 74

3.2 Comparison of measured (Meas) and calculated R_{50} values. Diff.1=(Meas-BEAMnrc) and Diff.2=(Meas-OMTPS). Agreement with measurements was found to be less than 1 mm for both OMTPS and BEAMnrc calculations. 80

3.3 Comparison between measured (Meas) and calculated output factors for 4, 12 and 18 MeV electron beams. Diff.1=[(Meas-OMTPS)/Meas], and Diff.2=[(Meas-BEAMnrc)/Meas]. . . . 83

4.1 Energy spectrum parameters of electron beams used for the BEAMnrc simulation. FWHM = full width at half maximum. Parameters of smaller peaks sometimes introduced in the spectrum are omitted here. 101

4.2 Absolute dose per monitor units (MU) calculated with XiO eMC in the homogeneous water phantom in the reference conditions. Computations have been performed for a standard field size of 10×10 cm^2 at 100 cm SSD. 104

4.3 Comparison of R_{50} between BEAMnrc/XiO eMC values and measurements (Meas) at 100 cm SSD. Diff.1=(Meas-BEAMnrc) and Diff.2 =(Meas-eMC). Good coincidence was achieved between BEAMnrc computations measurements as well as between XiO eMC calculations and measurements. 107
4.4 Comparison between measured (Meas) and calculated output factors for 4 and 8 MeV electron beams. Dif.1=[(Meas-BEAMnrc)/Meas], Dif.2=[(Meas-XiO eMC)/Meas] and Field Z.=field size. 108
4.5 Comparison between measured (Meas) and calculated output factors for 12 and 18 MeV electron beams. Dif.1=[(Meas-BEAMnrc)/Meas], Dif.2=[(Meas-XiO eMC)/Meas] and Field Z.=field size. 108
4.6 Comparison of CPU times in hours (h) between BEAMnrc and XiO eMC calculations in the heterogeneous phantom for the entire dose distribution (PDD and lateral dose profile) with a voxel size of $0.25\times0.25\times0.25$ cm^3 and a treatment distance of 100 cm SSD. 113

5.1 Comparison between measured (Meas) and calculated output factors for 4 and 12 MeV electron beams. Dif.1=[(Meas-OMTPS)/Meas], Dif.2=[(Meas-PBA)/Meas] and PBA=HELAX-TMS. 125
5.2 Comparison between measured (Meas) and calculated output factors for 4 and 8 MeV electron beams. Dif.1=[(Meas-XiO eMC)/Meas], Dif.2=[(Meas-PBA)/Meas] and Field Z.=field size. 126
5.3 Comparison between measured (Meas) and calculated output factors for 12 and 18 MeV electron beams. Dif.1=[(Meas-XiO eMC)/Meas], Dif.2=[(Meas-PBA)/Meas] and Field Z.=field size. 127

Chapter 1

Introduction

1.1 Brief History

The discovery of X-rays by Roentgen in 1895 followed by the radioactivity by Becquerel in 1896 and the isolation of radium by Curies in 1898 were two events that revolutionized medical diagnosis and treatment. The first therapeutic uses of X-rays in cancer quickly followed this initial discovery. Early radiotherapy has been performed with low voltage generation producing X-rays (100-400 kV) with little penetrating power, which limited their application to the treatment of superficial skin cancers. In the late 1930s and the early 1940s, the development of Van de Graaff and betatron accelerators made possible megavoltage radiation therapy. The Van de Graaff generator was one of the first machines used for electron beam radiation therapy as reported by Trump [1]. Electron beams produced by these machines were limited to a few MeV, while betatrons were able to accelerate electrons up to tens of MeV which was useful in producing megavoltage x-ray beams. These machines became the accelerators of choice after the World War II and besides producing high-energy x-ray beams, they were able to produce electron beams in the energy ranging from 5 to approximately 30 MeV, which were of great interest for radiation therapy applications. Major advances in the development of medical linear accelerators have made them today

Thesis submitted in fulfillment of the requirements for the degree of "Docteur en Sciences Médicales - Orientation : Physique Médicale" - september 11, 2012.

an equipment of choice for radiation therapy treatment. Electron beam treatment has been an important radiation therapy modality for over 50 years. They can be used to deliver a reasonable uniform dose from the patient surface to a given depth, after which the dose falls off rapidly to a zero value. Using electron beam allows disease, within approximately 6 cm depth, to be accurately treated while sparing deeper normal tissues. Many type of cancer can be concerned, namely: (1) skin (eyelids, nose, ear, scalp and limbs) and lips, (2) upper-respiratory and digestive tract (floor of mouth and salivary glands), (3) Breast (chest-wall irradiation following mastectomy, nodal irradiation and boost to the surgical bed) and other sites like (4) retina, orbit, spine (craniospinal irradiation), pancreas and other abdominal structures. In the case of electron beams used in the chest wall irradiation, the ribs and lungs of the patients represent high and low-density structures that perturb the dose distribution. The reproduction of dose perturbation due to ribs heterogeneties, wich are narrow compared to the field size is a good and severe test that can be performed to evaluate the accuracy of treatment planning algorithms.

1.2 Outline of the thesis

The purpose of this thesis was the validation of two commercial Monte Carlo (MC) based treatment planning systems (TPSs) as a commissioning step before the clinical implementation. Commissioning is one of the most important steps of the entire quality assurance program (QA) for TPSs. One of the important goal in the commissioning process involves the verification and validation of the ability of the dose calculation algorithms to reproduce measured dose distribution in the reference and the conditions that are found in the clinic. Our approach for the commissioning process combines both experimental measurements and Full MC simulation using the BEAMnrc [2] user code. BEAMnrc is a general purpose MC simulation system developed at the National Research Council (NRC) of Canada for modeling radiotherapy units. It is based on the EGSnrc package [3] for MC simula-

tion of coupled electron-photon transport. The two MC based TPSs are, Oncentra MasterPlan TPS (OMTPS) version 1.4 and XiO eMC TPS developed and commercialized by MasterPlan Nucletron and ELEKTA CMS Software Group, respectively. Electron beam of 4, 8, 12 and 18 MeV involved in this project are from an ELEKTA SL25 Medical linear accelerator of the radiotherapy department of St-Luc University Hospital.

1.3 Quality assurance and Quality control for TPSs

1.3.1 Quality assurance

Quality assurance (QA) is an important point in radiation therapy for a safe and accurate dose delivery to the target volume while reducing complication and recurrence rates. A well-established QA program reduces uncertainties and errors in dosimetry, treatment planning, equipment performance and treatment delivery and thereby, improves radiotherapy outcomes. Our work falls under a quality assurance program specific for TPSs. The definition of the QA can be found bellow as stated by the World Health Organization [4].

- General definition

"Quality assurance" is all those planned and systematic actions necessary to provide adequate confidence that a product or service will satisfy the given requirements for quality [4]. As such it is wide ranging, covering all relevant procedures, activities and actions. Therefore, all groups of staff are involved in the process under consideration.

- QA assurance in radiotherapy

"Quality assurance in radiotherapy" is all procedures that ensure consistency of the medical prescription, and safe fulfilment of that prescription, as regards to the dose to the target volume, together with minimal dose to normal tissue, minimal exposure of personnel and adequate patient monitoring aimed at determining the end result of the treatment. Again, it must

be stressed that quality assurance in radiotherapy is concerned with all aspects of the radiotherapy process and should involve all groups of staff in a cooperative approach, since quality activities are interdependent. The commissioning process of TPS is one part of a well established QA program. The purpose of the commissioning process is to enhance the QA of the TPS and planning process.

1.3.2 Quality control

QA does not end once the TPS has been commissioned, an ongoing QA program must be maintained in order to minimize the risk of error in the patient dose delivery.

"Quality control" is the regulatory process through which the actual quality performance is measured, compared with existing standards, and the actions necessary to keep or regain conformance with the standards. Quality control is one part of overall quality assurance. It is concerned with operational techniques and activities used, namely:

(1) To check that quality requirements are met;

(2) To adjust and correct performance if the requirements are found not to have been met.

1.4 Brief overview of the problematic of electron dose calculation

The aim of radiotherapy is to deliver enough radiation to the tumor so as to destroy it while maintaining the dose to the surrounding tissues as low as possible. Patient treatment planning process involves several steps starting from the localization of the tumor and important normal tissues that could be affected by the radiation treatment, to the actual dose delivery. Uncertainties are introduced during each step, accumulating to an overall

uncertainty for the entire process of dose delivery. TPSs are used to determine the absorbed dose distribution that will result in the patient body for a selected incident beams arrangements. The overall uncertainty on the dose delivery can be reduced by improving the quality of TPS dose calculation engine. Before the introduction of MC simulation in the radiotherapy computation, the electron dose calculations engines implemented in clinical radiotherapy TPS were pencil beam algorithms (PBA) that are based upon the generalized Fermi-Eyges theory [5-8]. The Fermi-Eyges theory relied on assumptions such as: (a) small angle scattering approximation, (b) the scattering medium is represented in slab geometry, (c) no electron absorption event occurs during the scattering process, (d) the secondary electrons set in motion by primary incident electron beam are ignored, and (e) the bremsstrahlung events of the electron beam are ignored. Under the above approximations which predict that the spatial and angular distribution of particles undergoing multiple scattering event are represented by a Gaussian distribution functions, it is expected that PBA will lead to the inaccuracy of the predicted dose calculation for radiotherapy applications. Several investigations have reported discrepancies up to 40% in the calculated dose distributions [9-14] with respect to measurements or MC computations, especially when the irradiated volume contains tissues and cavities that are radiologically different from water such as lungs, air cavities, bones structures, or in the interface of tissues with different densities (e.g. of interface tissues-air cavity).The above differences can mainly be explained from changes in electrons scattering properties of the above different tissues. MC methods applying detailed phase-space information of electron beams, including energy, charge, angular and spatial distribution, have proven to be among the best tools for computing radiotherapy dose [15-18]. A number of groups have attempted to model various linear accelerators by using this technique for many purposes [19-24] thus, demonstrating the rationale of MC simulation in radiation therapy. As the MC method is by its nature very time consuming and impractical for radiotherapy applications, a number of approximations and simplifications, to speed up calculations, have

been included in the commercial MC dose calculation engines, leading to the development of "fast MC" algorithms [25-30] implemented in some TPS for patients dose computation. Traditionally, the clinical implementation of every MC based TPS involves design compromises with possible errors. As TPSs are used to determine the absorbed dose distribution for patient treatments, the commissioning process is a mandatory step before their clinical use, as required by a numbers of published reports on that matter [31-33].

1.5 Thesis organization

The present work is organized in five main parts. The first part is the general introduction. The second part is focused on the review of some basic dosimetric concepts. For completeness also, photon interactions and dosimetry definitions are presented beside electron interactions, TPS algorithms and MC simulations in radiation therapy that are treated in more detail. The commissioning of the TPSs OMTPS and XiO eMC are presented in third and fourth chapters, respectively. the fifth part is focused on the discussion, conclusion and future prospects. In this part, we first consider one of the most conflicting situations in electron dose calculation, namely the use of highly asymmetric cutouts by comparing output factors, between OMTPS and PBA on the one hand, and between XiO eMC and PBA on the other hand, providing a proof of the added value of MC simulation. Second, a discussion is presented on the accuracy of both TPSs in the heterogeneous phantom compared to PBA. Third, a comparison between both TPSs is presented for two energies 4 and 12 MeV in order to highlight the strong and weak points of each one and we end with a brief conclusion followed by future prospects.

1.6 Bibliography

[**1**] Trump JG. Radiation for therapy: in retrospect and prospect. Am J Roentgenol Radium Ther Nucl Med 1964:91;22-30.

[**2**] Rogers DWO, Faddegon BA, Ding GX, Ma CM, We J, Mackie TR. BEAM: a Monte Carlo code to simulate radiotherapy treatment units. Med Phys 1995;22:503-24.

[**3**] Kawrakow I. Accurate condensed history Monte Carlo simulation of electron transport. I. EGSnrc, the new EGS4 version. Med Phys 2000;27:485-98.

[**4**] World Health Organisation. Quality Assurance in radiotherapy. WHO, Geneva,1-14, 1988.

[**5**] Fermi E. The ionization loss of energy in gases and in condensed materials. Phys Rev 1940;57:485-93.

[**6**] Rossi B, Greisen K. Cosmic-ray theory. Rev Mod Phys 1941;13:265-8.

[**7**] Eyges L. Multiple scattering with energy loss. Phys Rev 1948;74:1534-35.

[**8**] Brahme A. Geometric parameters of clinical electron beams. Acta. Radiol. Suppl. 1983;364:11-19.

[**9**] Almon SS, Kenneth RH. Pencil-beam redefinition algorithm for electron dose distributions. Med Phys 1991;18:7-18.

[**10**] Cygler J, Battista JJ, Scrimger JW, et al. Electron dose distributions in experimental phantoms: a comparison with 2D pencil beam calculations. Phys Med Biol 1987;32:1073-86.

[**11**] Mah E, Antolak J, Scrimger JW, et al. Experimental evaluation of 2D and 3D electron pencil beam algorithm. Phys Med Biol 1989;34:1174-94.

[**12**] Hogstrom KR, Mills MD, Almond PR. Electron beam dose calculations. Phys Med Biol 1981;26:445-59.

[**13**] Hogstrom KR, Mills MD, Meyer JA, et al. Dosimetric evaluation of a pencil-beam algorithm for electrons employing a two-dimensional heterogeneity correction. Int J Radiat Oncol Biol Phys 1984;10:561-69.

[**14**] Ostwald PM, Metcalfe PE, Denham JW, et al. A comparison of three electron planning algorithms for a 16 MeV electron beam. Int J Radiat Oncol Biol Phys 1994;28:731-40.

[**15**] Mackie TR. Applications of the Monte Carlo method in radiotherapy. In: The Dosimetry of Ionizing Radiation 3, editors Kase KR, Bjamgard BE, Attix FH (San Diego, CA: Academic); 1990. p. 541-620.

[**16**] Mohan R, Antolak J. Monte Carlo techniques should replace analytical methods for estimating dose distributions in radiotherapy treatment planning. Med Phys 2001;28:123-26.

[**17**] Rogers DWO, Bielajew AF. Monte Carlo techniques of electron and photon transport for radiation dosimetry. In: The Dosimetry of Ionizing Radiation 3, editors Kase KR, Bjamgard BE, Attix FH (San Diego, CA: Academic); 1990. p. 427-539.

[**18**] Rogers DWO. The role of Monte Carlo simulation of electron transport in radiation dosimetry. Int J Radiat Appl Instrum 1991;A42:965-74.

[**19**] Ma CM, Faddegon BA, Rogers DWO, et al. Accurate characterization of Monte Carlo calculated electron beams for radiotherapy. Med Phys 1997;24:401-16.

[**20**] Zhang GG, Rogers DWO, Cygler JE, et al. Monte Carlo investigation of electron beam output factors versus size of square cutout. Med Phys 1999;26:743-50.

[**21**] Kapur A, Ma CM, Mok EC, at al. Monte Carlo calculations of electron beam output factors for a medical linear accelerator. Phys Med Biol 1998;43:3479-94.

[**22**] Julius VT, Brett DS, Damian AB, et al. Monte Carlo calculations of output factors for clinically shaped electron fields. Journal of Applied

Clinical Medical Physics. 2004;5:42-62.

[**23**] Pavon EC, Sanchez-Doblado F, Leal A, et al. Total skin electron therapy treatment verification: Monte Carlo simulation and beam characteristics of large non-standard electron fields. Phys Med Biol 2003;48:2783-96.

[**24**] Popescu IA, Shaw CP, Zavgorodni SF, et al. Absolute dose calculations for Monte Carlo simulations of radiotherapy beams. Phys Med Biol 2005;50:3375-92.

[**25**] Kawrakow I, Fippel M. VMC++, a fast MC algorithm for radiation treatment planning. In: XIII international conference on the use of computers in radiation therapy. Heidelberg, Germany: Springer-Verlag; 2000. p. 126-8.

[**26**] Kawrakow I. VMC++, electron and photon Monte Carlo calculations optimized for radiation treatment planning. In: Kling LA, Barao F, Nakagawa M, Tavora L, Vaz P, editors. Advanced Monte Carlo for radiation physics, particle transport simulation and applications: proceeding of the Monte Carlo 2000 meeting. Berlin: Springer; 2001. p. 229-36.

[**27**] Kawrakow I, Fippel M. Investigation of variance reduction techniques for Monte Carlo photon dose calculation using XVMC. Phys Med Biol 2000;45: 2163-83.

[**28**] Fippel M, Kawrakow I, Friedrich K. Electron beam dose calculations with the VMC algorithm and the verification data of the NCI working group. Phys Med Biol 1997;42:501-20.

[**29**] Fippel M. Fast Monte Carlo dose calculation for photon beams based on the VMC electron algorithm. Med Phys 1999;26:1466-75.

[**30**] Ma CM, Li JS, Pawlicki T, Jiang SB, Deng J, Lee MC, et al. A Monte Carlo dose calculation tool for radiotherapy treatment planning. Phys Med Biol 2000;47:1671-89.

[**31**] Bruinvis IAD, Keus RB, Lenglet WJM, Meijer GJ, Mijnheer BJ, Van't Veld AA, et al. Quality assurance of 3-D treatment planning systems for

external photon and electron beams: Practical guidelines for acceptance testing, commissioning and periodic quality control of radiation therapy treatment planning systems. NCS Report 15:2006.

[**32**] Fraass BA, Doppke KP, Hunt MA, Kutcher GJ, Starkschall G, Stern RL, et al. Task Group 53: Quality assurance for clinical radiotherapy treatment planning, Med Phys 1998;25:1773-29.

[**33**] Van Dyk J, Barnett RB, Cygler JE, Shragge PC. Commissioning and quality assurance of treatment planning computers. Int J Radiat Oncol Biol Phys 1993;26:261-73.

Chapter 2

Theory

2.1 Radiation interaction with matter

The absorbed dose distribution in the patient is a result of several interaction mechanisms of radiations with patient body. When they are moving through the medium, high-energy photons, electrons and positrons suffer multiple interactions by which energy is transferred to the atoms and molecules of the material. The related transfer mechanisms involved will be described in these subsections below.

2.1.1 Photon interactions

Photons are electromagnetic radiation with zero mass and electrically neutral. When they move through the matter, their energy transfer is governed statically by interaction probabilities which depend on energy and the medium. The different types of photon interactions will be described below.

- **Photoelectric effect**

The photoelectric effect is a process in which a photon with initial energy E, undergoes an interaction with absorber atom and completely disappears.

This interaction is only possible when the incoming photon has sufficient energy to overcome the binding energy and remove the electron from the atom. The photoelectron ejected from one of the bound shells (mostly the K or L shells) of the atom has an energy given by

$$E_e = E - U_i \tag{2.1}$$

where U_i represents the bounding energy of the photoelectron in its original

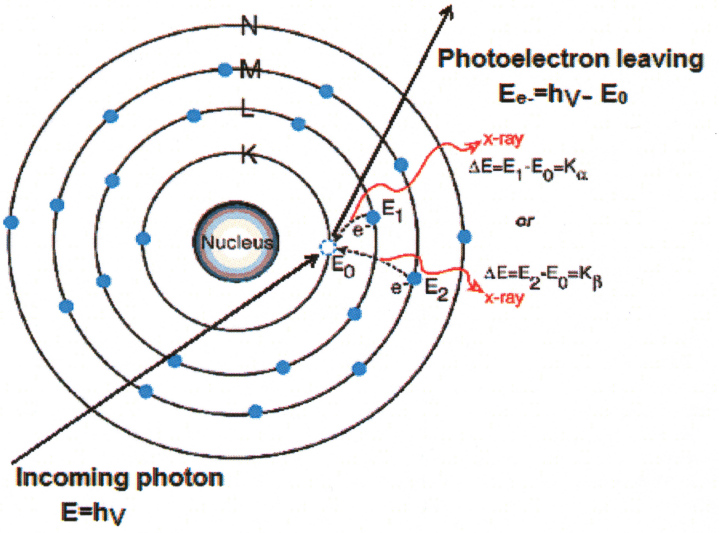

Figure 2.1. Schematic representation of the photoelectric process. In this diagram, the incoming photon ejects the photoelectron, followed by the movement of an outer orbital electron (from the L or M shell) into the vacancy created. A florescent photon is emitted with an energy K_α or K_β if the electron filling the vacancy comes from the L or M shell, respectively.

shell. The injection of the photoelectron leaves an ionized absorber atom with a vacancy in the bound shell which is quickly filled through one of the two mechanisms: (a) capture of a free electron from the medium, (b) rearrangement of electrons from other shells of the atom. As illustrated in Fig. 2.1 above, the process (b) leads to the generation of one or more characteristic X-ray photons. The energy transfer mechanism is then a two-

step process. In the first step, a portion energy of the incoming photon is used to overcome the electron's binding energy and in the second step, the remaining energy transferred to the electron, as kinetic energy, is deposited in the surrounding matter. A rough approximation of the probability of the photoelectric absorption effect (symbolized τ), is

$$\tau \propto \frac{Z^2}{E^3} \tag{2.2}$$

- **Incoherent scattering**

In the incoherent scattering, also known as Compton effect, a portion of the incoming photon energy E is transferred to an recoil electron which is assumed to be initially in rest. The incoming photon leaves the interaction site in the direction different from the original one. In this case of scattering by free electrons at rest, the conservation of energy and momentum leads to the following relation between the energy E' of the scattered (Compton) photon and the scattering angle θ

$$E' = \frac{E}{1 + \kappa\,(1 - cos\theta)} \tag{2.3}$$

where $\kappa = E/m_e c^2$ stands for the incoming photon energy in units of the electron rest energy. The Klein and Nishina formula [2] of the differential cross-section (DCS) derived according to Dirac's relativistic theory of the electron is given by

$$\frac{d\sigma}{d\Omega} = \frac{r_e^2}{2} f(\kappa,\theta)^2 \left[f(\kappa,\theta) + f(\kappa,\theta)^{-1} - sin^2\theta \right] \tag{2.4}$$

where $f(\kappa,\theta) = 1/\left[1 + \kappa(1 - cos\theta)\right]$ and $\kappa = E/m_e c^2$, as before. C is the velocity of light.

- **Coherent Scattering**

This type of scatter also referred by a variety of names, including Thompson, Rayleigh, classical and elastic, is a pure scattering process in which the in-

coming photon is deflected from its original direction without loss of energy. This type of photon interaction does not contribute to the absorbed dose to the patient. The scattering is qualified as "coherent" because it arises from the interference between secondary electromagnetic waves coming from different parts of the atomic charge. The atomic DCS [3] distribution describing this physical process is given approximately by

$$\frac{d\sigma_{Ra}}{d\Omega} = \frac{d\sigma_T}{d\Omega}\left[F(q,Z)\right]^2 \tag{2.5}$$

where

$$\frac{d\sigma_T(\theta)}{d\Omega} = r_e^2 \frac{1+cos^2\theta}{2} \tag{2.6}$$

is the classical Thomson DCS for scattering by a free electron at rest, θ is the polar scattering angle and F(q, Z) is the atomic form factor. The quantity r_e is the classical electron radius and q is the magnitude of the momentum transfer given by

$$q = 2(E/c)sin(\theta/2) = (E/c)\left[2(1-cos\theta)\right]^{1/2} \tag{2.7}$$

The atomic form factor is derived from the Fourier transform of the atomic electron density $\rho(r)$ which, for a spherically symmetrical atom, can be simplified as

$$F(q,Z) = 4\pi \int_0^\infty \rho(r) \frac{sin(qr/\hbar)}{qr/\hbar} r^2 dr \tag{2.8}$$

- **Electron-positron pair production**

This is a threshold photon-matter interaction that occurs only with photons with energies in excess of $2m_ec^2$. In this process, the incoming photon interacts with atomic nucleus and its energy is converted into matter. This interaction produces a pair of particles, an electron and positron with the same mass, each equivalent to a rest mass energy of m_ec^2. In the case where this phenomenon occurs in the field of an electron, the target electron

recoils after the event with appreciable kinetic energy. This type of interaction which is known as "triplet production" occurs with a threshold energy of $4m_ec^2$ (assuming the electron is at rest). The high-energy DCS for this process, for arbitrary screening, was derived by Bethe and Heitler from the Born approximation [4, 5]. This Bethe-Heitler DCS for any incoming photon of energy E to create an electron-positron pair, in which the electron has a kinetic energy of $E_- = \epsilon E - m_ec^2$, can be expressed as

$$\frac{d\sigma_{pp}}{d\epsilon} = r_e^2 \alpha Z \left[Z + \eta\right] \left\{ \left[\epsilon^2 + (1-\epsilon)^2\right] (\Phi_1 - 4f_C) + \frac{2}{3}\epsilon(1-\epsilon)(\Phi_2 - 4f_C) \right\} \tag{2.9}$$

where $\epsilon = (E_- + m_ec^2)/E$ stands for the fraction of the photon energy that is taken away by the electron. Φ_1 and Φ_2 are the screening functions given by integrals that involve the atomic form factor [5, 6] and f_C is the high-energy Coulomb correction of Davies, Bethe and Maximon [7].

2.1.2 Attenuation coefficients

When a photon moves through a medium, there is no way to predict how far it will travel before it undergoes an interaction and which type of interaction will occur. In radiotherapy applications, we are usually concerned with a large number of photons and in most instances, we are interested in the overall rate at which photons interact as they move through a given material. The interactions described above remove some photons from the beam in a process referred to as attenuation. The linear attenuation coefficient is the actual fraction of photon per unit thickness of material. It indicates, for each interaction type, the rate at which photons interact as they move through a given medium and it is related to the inverse mean free path before interacting. In the case of the photoelectric absorption process, this attenuation coefficient is given by

$$\mu_{ph} = \frac{N_A \rho}{A_M} \sigma_{ph} \tag{2.10}$$

where N_A is the Avogadro's number and A_M the molar mass, respectively. The total mass attenuation coefficient can then be expressed as

$$\frac{\mu}{\rho} = \frac{N_A}{A_M}\left(\sigma_{Ra} + \sigma_{ph} + \sigma_{Co} + \sigma_{pp}\right) \tag{2.11}$$

The Fig. 2.2 below illustrates the magnitude of the different processes described above as a function of energy, for two materials, water and lead respectively.

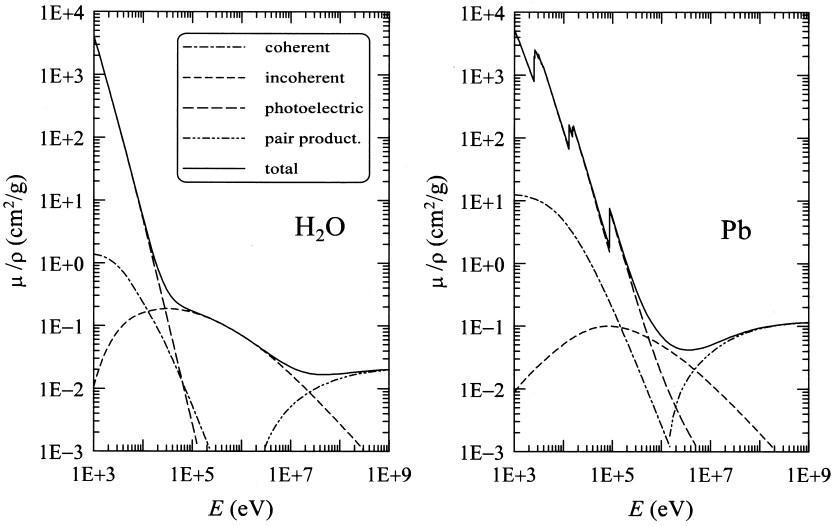

Figure 2.2. Representation of partial and total mass attenuation coefficients for two materials as function of energy: water on the left and lead on the right (from Salvat et *al.* [1]).

2.1.3 Electron interactions

Electrons are a class of charged particles that experience coulomb-force interactions with atomic orbital electrons and the atomic nuclei when they move through a medium. For a particular atom of radius a, these interactions can be classified, depending of the magnitude of the classical impact parameter b (Fig. 2.3), as: (i) Coulomb-force interactions with the extremal nuclear field for b $\ll$ a, (ii) hard collisions for b $\approx a$, and (iii) soft collisions for b

$\gg$ a. Due to the large mass of the target ($\approx 3600 Z m_e$), the average energy lost by the projectile is a very small fraction of its initial energy. Therefore, electrons experience a large number of interactions before coming to rest. In each interaction, the electron is deflected from its original direction (scattering) and transfers a fraction of its kinetic energy to the medium (collisional loss) or to the photon (radiative loss). The radiative and collisional loss are described by stopping power relationships and the scattering is governed by electron scattering laws. This section deals with the description of the above phenomena.

- **Electron scattering in the nuclear Coulomb field**

When the impact parameter b is much smaller in comparison to the size a of the atomic absorber (b $\ll$ a), the incoming electron experiences a coulomb interaction mainly between the incident electron with the nucleus. The electron-nucleus (e-n) interaction can happen through two physical processes, namely: the elastic and inelastic scattering. The latter process occurs only in about 2-3% of the electron-nucleus encounters and leads to the emission of the bremsstrahlung photon (in addition to a deflection in direction) with an energy spectrum between zero and the incident electron kinetic energy. The energy of the emitted bremsstrahlung photon depends on the magnitude of the impact parameter b; the smaller the impact parameter is, the higher the energy of the bremsstrahlung photon will be. In most of the electron-nucleus interactions, the incident electron undergoes an inelastic collision, i.e., no emission of photon and no excitation of the nucleus. In this case, the electron transfers a significant amount of its kinetic energy necessary to satisfy the conservation of momentum. The DCS for this physical process, taking into account the screened nuclear potential, can been expressed by the equation (2.12) bellow

$$\frac{d\sigma_{en}}{d\Omega} = \left(\frac{1}{4\pi\epsilon_0}\right)^2 \left\{\frac{2m_e Z e^2}{\hbar^2(4k^2 sin^2\theta/2 + a^{-2})}\right\}^2 \tag{2.12}$$

where the wave number k=$2\pi/\lambda$ and λ is the L. De Broglie wavelength.

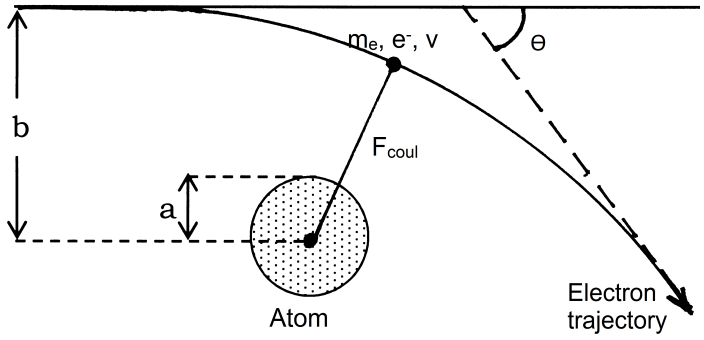

Figure 2.3. Representation of Coulomb interaction between an electron with mass m_e, velocity v and charge e^- and an atom. b is the impact parameter, a is the atomic radius and θ the scattering angle.

- **Electron scattering by atomic electrons**

In the case where the impact parameter b is in the order of magnitude compared to the atomic size a ($b \approx a$), the electron will undergo a hard collision with an orbital electron and an appreciable fraction of its kinetic energy will be transferred to the orbital electron. This type of interaction is known as hard collisions because the electron may loss up to 50% of its initial kinetic energy. This physical process has been studied non relativistically by Mott and relativistically by Mϕller. The Mϕ11er's DCS describing this phenomenon in the interval of scattering angles θ and $\theta + d\theta$ [8, 9] is given by equation (2.13) in which $\gamma = \left(1 - \frac{v^2}{c^2}\right)^{-1/2}$.

$$\left(\frac{d\sigma}{d\Omega}\right)_{ee} = \pi D_{ee}^2 \left\{ \frac{4(\gamma+1)}{(1-x^2)^2} - \frac{3(\gamma+1)}{(1-x^2)} + \frac{(\gamma-1)(\gamma^2-1)}{4\gamma^2} \left(\frac{5-x^2}{1-x^2}\right) \right\} \frac{dx}{d\Omega} \tag{2.13}$$

where

$$x = \frac{2-(\gamma+3)sin^2\theta}{2+(\gamma-1)sin^2\theta} \tag{2.14}$$

$$dx = \frac{2(\gamma+1)cos\theta sin\theta d\theta}{[cos^2\theta + (1/2)(\gamma+1)sin^2\theta]^2} \tag{2.15}$$

and

$$D_{ee} = \frac{e^2}{a\pi\epsilon_0(m_e v^2/2)}. \tag{2.16}$$

with ϵ_0 the permitivity of free space ($8.89 \times 10^{-12} CV^{-1}m^{-l}$), Z is the atomic number of the nucleus. m_e and v are the total mass and velocity of the electron, respectively.

- **Soft collisions**

In the latter case corresponding to b $\gg$ a, the electron will undergo a soft collision with the whole atom and only a small amount of energy will be transferred from the incident electron to orbital electrons with essentially no change in the direction. Those collisions are, by far, the most type of electron interactions with the medium and account for around half of the energy loss. The other half is transferred through excitation processes (transfer of an orbital electron of the absorber atom from an allowed orbit to a higher allowed orbit) of the atom to the higher energy level and ionization processes, i.e. ejecting the valence shell electron. Atomic excitations and ionizations result in collisional energy losses and are characterized by collision (ionization) stopping powers.

2.2 Stopping power

The inelastic collision of an electron traveling through a medium with density ρ is characterized by the total mass-energy stopping power $(S/\rho)_{tot}$, defined as the average kinetic energy loss by an electron E_e per unit path length x, divided by the density of the medium ρ. $(S/\rho)_{tot}$ is expressed as follows

$$\left(\frac{S}{\rho}\right)_{tot} = -\frac{1}{\rho}\frac{dE_e}{dx} \tag{2.17}$$

$(S/\rho)_{tot}$ can be split into two components, (a) the mass collision stopping power $(S/\rho)_{col}$, resulting from the electron-orbital electron interactions (atomic excitations and ionizations), and (b) the mass radiative stopping power $(S/\rho)_{rad}$, which represents the contribution of electron-nucleus interactions (bremsstrahlung production), as

$$\left(\frac{S}{\rho}\right)_{tot} = \left(\frac{S}{\rho}\right)_{col} + \left(\frac{S}{\rho}\right)_{rad} \tag{2.18}$$

$(S/\rho)_{tot}$ plays an important role in radiation dosimetry, since it is used to compute the dose to the medium as well as to calculate the electron range R.

2.3 Radiation dosimetry

First of all, the radiation dosimetry deals with methods for a quantitative determination of energy deposited in a given medium by directly or indirectly ionizing radiations. As this thesis deals with the dosimetry of electron beam, before we proceed any further, it is important to start first with the presentation of some basic quantities and units used for the description of a monoenergetic and polyenergetic ionizing radiation beam.

2.3.1 Particle fluence and Energy fluence

The particle fluence, Φ, is defined as the ratio of incident particles dN on a sphere of cross-sectional area dA as follows

$$\Phi = \frac{dN}{dA} \tag{2.19}$$

The unit of this quantity is m^{-2}. In this definition, one considers an area dA perpendicular to the direction of each particle and hence insures the independence of particle fluence with the incident angle of the radiation beam. In the same manner, the energy fluence Ψ expressed in unit of J/m^2 is the quotient of dE by dA, where dE is the radiant energy incident on a

sphere of cross-sectional area dA according to the following relation

$$\Psi = \frac{dE}{dA} = \frac{dN}{dA}E = \Phi E \tag{2.20}$$

where E is the energy of the particle and dN represents the number of particles with energy E. In radiation therapy, all beams are polyenergetic, thus, the above concepts need to be applied for such beams as follows

$$\Phi_E(E) = \frac{dN}{dA}(E) \tag{2.21}$$

and

$$\Psi_E(E) = \frac{d\Psi}{dE}(E) = \frac{d\Phi}{dE}(E)E \tag{2.22}$$

in which $\Phi_E(E)$ and $\Psi_E(E)$ represent the particle fluence spectrum differential and the energy fluence spectrum differential, respectively. Particle fluence rate and energy fluence rate can be derived from equations (2.19) and (2.20) by dividing these equations by dt. Their units are $m^{-2}s^{-1}$ and $Jm^{-2}s^{-1}$, respectively.

2.3.2 Kerma (Indirectly ionizing radiations)

This concept is applied to indirectly ionizing radiations such as photons and neutrons. Kerma is an acronym for kinetic energy released per unit mass. The energy transferred to matter by photons is a two-step process. In the first step, the incoming photon transfers its energy to the electrons through various photon interactions described previously. In the second step, electrons transfer their energy to the medium through atomic excitations and ionizations. In this context, the kerma is defined as the mean energy $d\overline{E}_{tr}$ transferred from the indirectly ionizing radiation to charged particles (electrons) in the medium per unit mass dm as follows

$$K = \frac{d\overline{E}_{tr}}{dm} \tag{2.23}$$

The unit of the Kerma is (J/kg) and is called the Gray (Gy).

2.3.3 Energy fluence and kerma (Photons)

As already stated in section 2.2, the energy transferred to electron from photon interactions can be expended through collision interactions (soft collisions and hard collisions) or through radiative interactions (bremsstrahlung and electron-positron annihilation). The total Kerma can be therefore split into a collision kerma, K_{col} part and a radiation kerma, K_{rad} part as follows

$$K = K_{col} + K_{rad} \tag{2.24}$$

From the average radiative fraction $\overline{g} = (K_{rad}/K)$, one can derive a frequently used relation between collision kerma K_{col} and total kerma in the form

$$K_{col} = K(1 - \overline{g}) \tag{2.25}$$

For a particular beam with given energy spectrum, the collision kerma at a given point of interest is obtained by

$$K_{col} = \int_0^{Emax} \Psi_E(E) \left(\frac{\mu_{en}}{\rho}\right) dE = \Psi \left(\frac{\bar{\mu}_{en}}{\rho}\right) \tag{2.26}$$

where Ψ given in equation (2.26) is the total energy fluence integrated through the spectrum and determined by the equation (2.27) below

$$\Psi = \int_0^{E_{max}} \Psi_E(E) dE \tag{2.27}$$

and $(\bar{\mu_{en}}/\rho)$, the mass-energy absorption coefficient for the medium averaged over the energy fluence spectrum which is given by the following equation

$$\left(\frac{\overline{\mu}_{en}}{\rho}\right) = \frac{1}{\Psi} \int_0^{E_{max}} \Psi_E(E) \frac{\mu_{en}}{\rho}(E) dE \tag{2.28}$$

2.3.4 Cema (Directly ionizing radiations)

An analogous quantity called Cema was introduced in the case of directly ionizing radiations such as electrons and protons. Cema is the acronym for converted energy per unit mass. It is defined by the ration of dE_c by dm, where dE_c is the energy lost by charged particles, except secondary electrons, in collisions in a mass dm of a material. The unit of this quantity is (J/kg) and is called the Gray (Gy).

$$C = \frac{dE_c}{dm} \tag{2.29}$$

These two quantities differs from the fact that, Cema involves the energy lost by incoming charged particles in their collisions with the atomic electrons, whereas, kerma is the kinetic energy transferred to outgoing charged particles by indirectly ionizing radiations. In the definition of Cema, one needs to exclude secondary electron fluence, which is difficult in certain cases.

2.3.5 Absorbed dose

The absorbed dose [10, 11] is a physical quantity applicable to both directly and indirectly ionization radiations. It is defined as the mean energy $\bar{\epsilon}$ imparted by ionizing radiation to matter of mass m in a limitingly small volume at the point of interest by

$$D = \frac{d\bar{\epsilon}}{dm} \tag{2.30}$$

The energy imparted $\bar{\epsilon}$ is the total energy entering the volume of interest minus the sum of the energy leaving the volume, taking into account any mass-energy conversion within the volume. Pair production, for example, decreases the energy by 1.022 MeV, while electron-positron annihilation increases the energy by the same quantity. The unit of absorbed dose is joule per kilogram (J/kg) and it is called the Gray (Gy).

2.3.6 Kerma and dose (Charge Particle Equilibrium)

The concept of charged-particle equilibrium (CPE) is useful in radiation physics as a mean of relating certain basic quantities. CPE is usually described as the balance on incoming and outgoing electrons at the boundary of a given small volume. In the volume preceding the CPE region, one can establish that the dose is less than the collision kerma. The two quantities equally when CPE is achieved. Another concept known as transient charged particle equilibrium (TCPE) was introduced to account for the more realistic situation in which photons are attenuated and scattered in the medium. In the TCPE conditions, the collision kerma underestimates the dose, but there is constant relation between each of them. In the special case in which true CPE exists (at the depth of maximum dose in the medium), the relation between absorbed dose D and total kerma K is given by

$$D = K_{col} = K(1 - \overline{g}) \tag{2.31}$$

2.3.7 Cema and dose (Electrons)

The derivation of Cema is obtained by integrating the unrestricted linear energy transfer, L(E), over the energy fluence of the primary electrons, $\Psi_E(E)$, as follows

$$C = \frac{1}{\rho} \int_{E_{min}}^{E_{max}} \Psi_E(E) L(E) dE \tag{2.32}$$

In practice, it may be difficult to distinguish between the fuence of primary and secondary electron, therefore, a modified concept of reduced Cema has been introduced in order to circumvent this difficulty. To this end, a suitable cutoff energy Δ of electrons needs to be defined. Hence, in this reduced quantity, C_Δ, one excludes from the radiation, electrons bellow this cutoff energy, as if their energy is dissipated on the spot. However, rather than disregarding the energy of secondary electrons, one disregards all electrons having an energy bellow the Δ value. In particular, all secondary electrons below the cutoff value of Δ are assumed to be absorbed locally, and those

above it, not absorbed locally. In the limit where $\Delta \approx 0$, the reduced Cema corresponds closely to the absorbed dose according to the following relation

$$C = \frac{1}{\rho} \sum \int_{E_{min}}^{E_{max}} \Psi_E(E) \Lambda_0(E) dE \;\approx\; D \tag{2.33}$$

The summation in the equation (2.33) extends to all kind of particles in the radiation field and Λ_0(E) stands for the energy expended per unit distance by a particle (of specified type and energy) against the binding energy. Usually, the contribution of uncharged particles can be neglected, therefore, Λ_0 can be taken to be the linear collision stopping power of charged particles minus the kinetic energy of electrons released per unit length.

2.3.8 Fluence and dose (Electrons)

In the case of electron beams, the absorbed dose in the medium can be predicted from the following equation

$$D_{med} = \Phi_{med} \left(\frac{S_{col}}{\rho} \right)_{med} \tag{2.34}$$

In equation (2.34), $(S_{col}/\rho)_{med}$ is the unrestricted mass collision stopping power of the medium at the energy of the electron and Φ_{med} is the electron fluence in the medium. This equation is valid under the conditions for which, (a) radiative photons escape the volume of interest and, (b) secondary electrons are absorbed on the spot (or there is a CPE of secondary electrons).

2.4 Electron beam characteristics

Electron beams have been used over 50 years as a radiation therapy modality for patient treatment of superficial cancers and diseases. This type of treatment modality provides an accurate dose delivery to the tumour whereas limiting it to the surrounding normal tissues and structures, something usually not possible with X-ray therapy. Produced by medical linear accelerators, electron beams in the range of approximately 4-25 MeV are

principally used in the treatment of (a) skin and lip cancers, (b) chest-wall and neck (elective post-surgery and recurrent disease) cancers, (c) upper respiratory and digestive-tract lesions from 1 to 5 cm in depth (using the electron beam alone, in combination with photon beams, in association with interstitial therapy or as a boost treatment to primary lesions), and (d) boost treatment to lymph nodes, operative scars and residual tumour. The rational of selecting electron beams for the treatment of the above diseases is due to their physical characteristics that we describe below.

2.4.1 General shape of depth dose curve

The general shape of percentage depth dose (PDD) for an electron beam is quite different from a photon beam. As depicted in figure 2.4, an electron central-axis depth dose curve is characterized by several parameters [12] and each of these parameters ($\%D_s$, $\%D_x$, R_t, R_{100}, R_{50}, R_p and G_0) is of clinical importance and can be affected by small differences in energy, scattering foils, collimation and source-to-surface distance (SSD). The above parameters have the following meaning: (1) D_s is the relative surface dose which is defined at 0.5 mm depth. (2) D_x is dose due to the X-ray component and should be as low as possible. (3) R_t is the therapy range, it is a measure of the clinically useful portion of the depth dose profile and is usually taken as the deepest 90% dose level. (4) The range parameters R_{100}, R_{50} and R_p are the depth of the dose maximum, D_{max}, in water, the depth of the 50% dose level and the practical range, respectively. R_{50} and R_p are used in range energy given by equations (2.35-2.37). (5) R_q is the depth at which the tangent to the depth dose curve at the point of inflection meets the level of D_{max}. (6) G_0=$R_p/(R_p$-$R_q)$ is the normalized dose gradient. This parameter is a measure of the steepness of the descending portion of the depth dose curve and it is much steeper at lower electron energies than that for higher electron energies. This is due to large scattering angle electrons experience at lower energy away from their initial directions.
In the Buildup region, i.e. $0 \leq Z \leq Z_{max} = R_{100}$, the dose increases rapidly due to the scattering interactions that the electrons experience with atoms

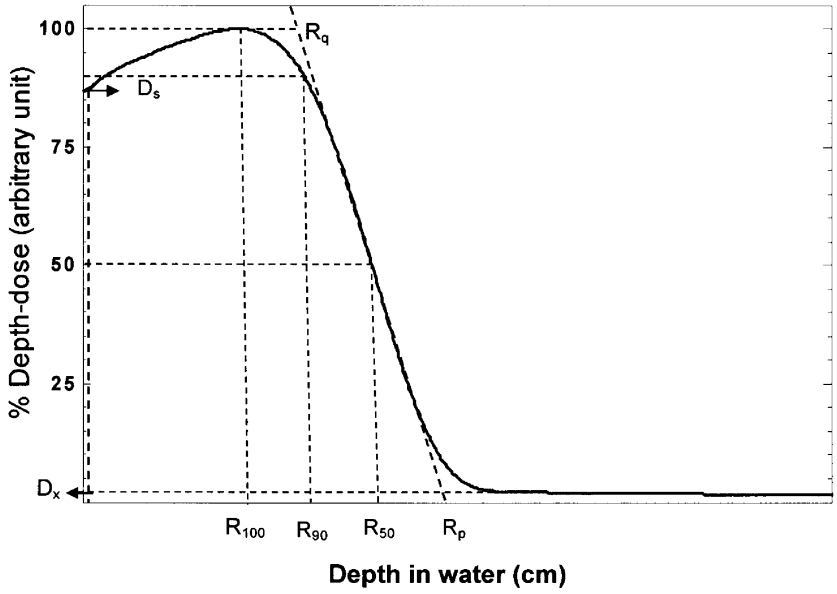

Figure 2.4. Typical electron PDD curve illustrating the definition of R_q, R_p, R_{100}, R_{50}, D_x, D_s and R_{90} for a 8 MeV electron beam from an ELEKTA SL25 medical linear accelerator. Field zise 10×10 cm^2 at a SSD of 100 cm.

of the absorber. Compared with megavoltage photon beams, the electron central axis depth dose curve exhibits a high surface dose, This is due to the electron scattering in the medium. At lower energies, electrons are scattered more easily and through larger angles with regard to their original direction. This causes the dose to build up more rapidly and over a shorter distance. Beyond the depth of maximum dose, Z_{max}, electron scattering and continuous energy loss process are the two physical phenomenons responsible for the sharp drop-off in the electron dose at depths beyond this depth. Bremsstrahlung photons produced in the head of the accelerator, in the air between the accelerator window and the patient, and in the irradiated medium are responsible for the tail in the depth dose curve. Fig. 2.5 shows depth dose curves for various electron beam energies. One can see that all the depth dose parameters previously discussed are different from

one clinical energy to another.

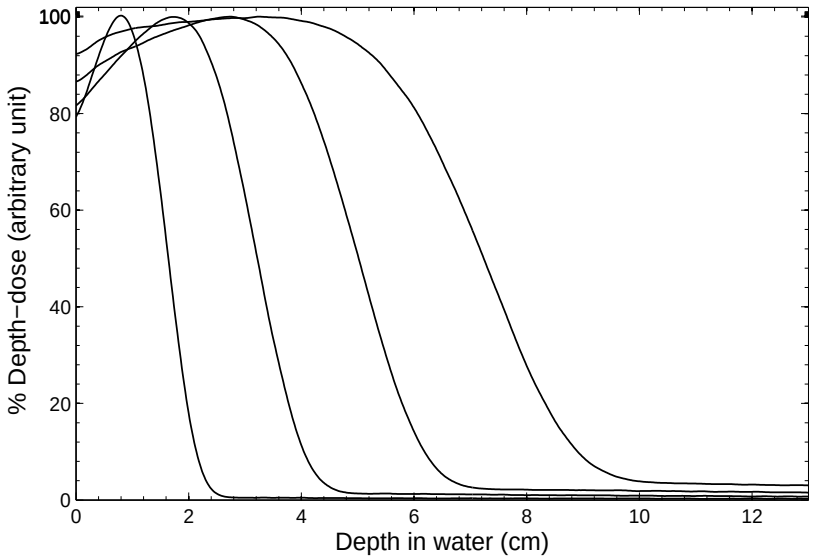

Figure 2.5. Central axis depth dose curves from an ELEKTA SL25 Medical linear accelerator. Field size 10×10 cm^2, energies (starting from left to right) 4, 8, 12 and 18 MeV for a 100 cm SSD. The normalization has been performed at the depth of maximum dose along the central axis.

2.4.2 Beam quality index specification

For high energy electron beams produced by clinical linear accelerators, the beam quality is specified by R_{50}, the depth in water in cm at which the absorbed dose falls by 50% of the maximum dose for a beam which has a field size on the phantom surface $\geq 10 \times 10$ cm^2 ($\geq 20 \times 20$ cm^2 for $R_{50} \succ 8.5$ cm, i.e., $E \succ 20$ MeV) at a source-to-surface distance (SSD) of 100 cm. This parameter can be determined either from a depth dose curve or from a depth ionization curve. The recommended device for depth ionization curves measurement is a plane-parallel ionization chamber, with the reference point of the chamber taken as the center of the inner surface of its front window. If a cylindrical chamber would be used, the reference point has to be taken as 0.5 times the inner radius of the chamber in front of the geometrical center

as depicted in Fig. 2.6 below. The beam quality index is measured under the following conditions: (1) the recommended medium of measurement is the water phantom, (2) constant SSD of 100 cm and, (3)the field size at the phantom surface must at least 10×10 cm^2 or 20×20 cm^2 if $R_{50,dos}$ is larger than 7 cm. $R_{50,dos}$ can been derived from the $R_{50,ion}$ according to the two following equations [12]

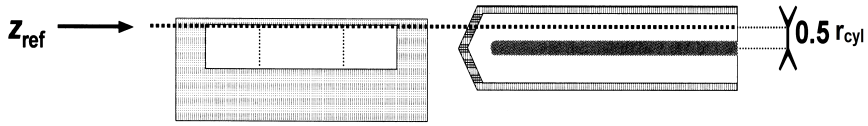

Figure 2.6. Illustration of the reference depth, Z_{ref} of a plane-parallel and cylindrical ionization chambers for the measurement of percentage depth ionization curve.

$$R_{50} = 1.029 R_{50,ion} - 0.06 \ \left(g/cm^2\right) \left(R_{50,ion} \leq 10 \ g/cm^2\right) \tag{2.35}$$

$$R_{50} = 1.059 R_{50,ion} - 0.37 \ \left(g/cm^2\right) \left(R_{50,ion} \succ 10 \ g/cm^2\right) \tag{2.36}$$

A direct determination of the beam quality index is to perform the conversion of the measured depth ionization curve into the depth dose by multiplying the ionization charge at each measurement depth with the corresponding ratio of the mass stopping power of water to air, which were determined by Berger using ETRAN and that can been found in ICRU Report 35 [11]. However, more accurate values were determined from realistic clinical electron beams by Ding et *al.* [13] and serve as the basis for conversion of ionization to dose.

2.4.3 Beam energy determination

Due to the complexity of the energy spectrum at the phantom surface, there is no single energy parameter that can be used to fully characterize an electron beam. Owing R_{50}, other parameters are used such as the most probable (kinetic) energy $E_{p,0}$ on the phantom surface and the mean energy $\overline{E}_0$. The most probable energy $E_{p,0}$ in MeV on the phantom surface is empirically

related to the practical range R_p in cm in water as follows [12]

$$E_{p,0} = 0.22 + 1.09R_p + 0.0025R_p^2 \tag{2.37}$$

and the mean energy $\overline{E}_0$ in MeV (mean incident energy) at the phantom surface is related to the beam quality index by the following relation

$$\overline{E}_0 = 0.656 + 2.059R_{50} + 0.022R_{50}^2 \tag{2.38}$$

Electron dosimetry calculations often require knowledge of beam energy at depth, Z, which can be estimated from the Harder's [14] equation given by

$$E_z = E_0(1 - Z/R_p) \tag{2.39}$$

where R_p stands for the practical range in cm given by [14]

$$R_p = 1.271R_{50} - 0.23 \tag{2.40}$$

2.4.4 Output factors for electron beams

The electron beam output, i.e., the dose per monitor unit, for all clinical applications must be measured with high accuracy. An important parameter that determines the electron beam output is the collimator jaw setting. When an electron applicator (cone) is inserted into the linear accelerator head, upper and lower jaws are automatically opened to a field size preset by the manufacturer and these settings are energy and applicator size dependent. The jaw openings are generally larger than the field size defined by the applicator. Such an arrangement minimizes the variation of collimator scatter and therefore the output variation with field size is kept reasonably small. Measurements of electron beam output as a function of field size are needed for each combination of open applicator, energy and SSD. Because the square field defined by the applicator does not adequately shield all normal tissues in most clinical situations, collimating blocks fabricated from lead or a low melting point alloy are routinely inserted into the end of the

applicator to shape the fields. Therefore, output factors referred as cutouts factors should also be measured for the above collimating blocks and other patient-specific irregular shaped fields. In this work, output factors (OF) in unit of gray per monitor unit (Gy/MU) are defined as

$$OF = \frac{D_{max}(E, S, SSD)}{D_{max}(E, 10 \times 10\ cm^2, SSD)} \tag{2.41}$$

where $D_{max}(E, S, SSD)$ is the maximum dose along the central axis of the field of interest for a given beam energy E, field size S and SSD. The factor in the denominator has the same meaning and the 10×10 cm^2 open applicator has been set for the normalization.

2.4.5 Profiles and off-axis ratios

Fig. 2.7 represents an example of dose profile for 8 MeV from an ELETKA SL25 medical linear accelerator. The depth of measurement is the depth of maximum dose along the central axis, for four field sizes of 6×6, 10×10, 14×14 and 20×20 cm^2 open applicator. The off-axis ratio (OAR) relates the dose at any point in a plane perpendicular to the beam direction to the dose on the central axis in that plane. A plot of the OAR against the distance from the central axis is referred to as a dose profile.

2.4.6 Flatness and symmetry

Beam flatness and symmetry have been defined by the International Electrotechnical Commission (IEC) [16]. Flatness is defined at a reference plane parallel to the surface of the phantom and perpendicular to the central axis. To be considered as acceptable, according to the IEC, the flatness specified at the depth of maximum dose, z_{max}, must fulfill two requirements. (1) The distance between the 90% dose level and the geometrical beam edge should not exceed 10 mm along the major axes and 20 mm along the diagonals, (2) the maximum value of the absorbed dose anywhere within the region bounded by the 90% isodose contour, should not exceed 1.05 times the absorbed dose on the central axis of the beam at the same depth. For the

symmetry, let us consider two arbitrary points "-x" and "+x" symmetric with respect to the beam axis. The specification for the symmetry of an electron beams according to the IEC at z_{max} is that the cross-beam profile should not differ by more than 3% for any pair of the two selected points.

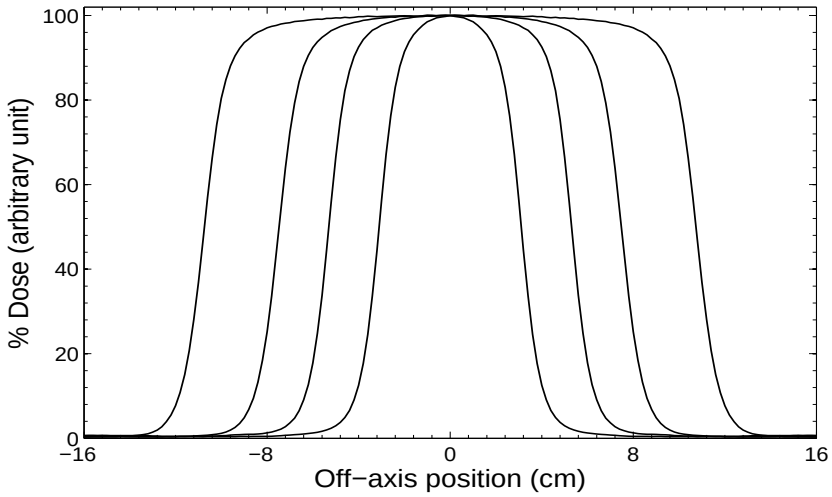

Figure 2.7. Representation of a typical dose profile for four field sizes of 6×6, 10×10, 14×14 and 20×20 cm^2 open applicator. The small profile corresponds to the 6×6 cm^2 field size. Electron beam energy is 8 MeV from an ELEKTA SL25 medical accelerator.

2.5 Radiation TPP: A step by step description

2.5.1 Volume definition

One of the important steps of the radiation treatment planning process is the definition of the target that will receive a high radiation dose. It is a prerequisite for meaningful three dimensional (3-D) treatment planning, for accurate dose reporting and provide a mean of comparison of treatment outcomes. These volumes illustrated in Fig. 2.8 are defined in the ICRU Rep. 50 [17] as follows

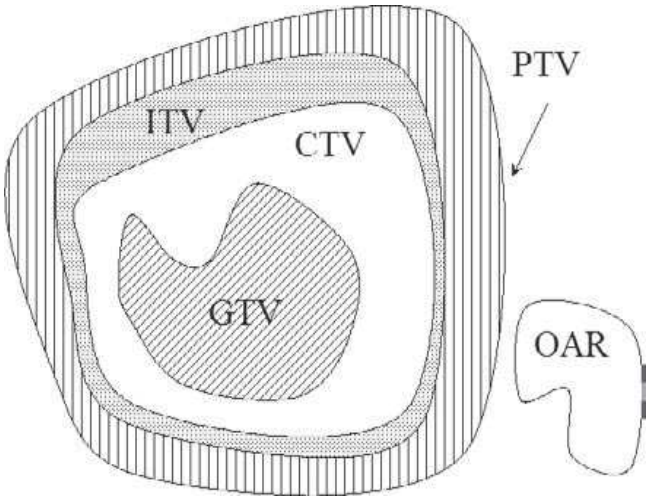

Figure 2.8. Representation of different volumes of interest and how they are related to each other (from P. Andreo et *al.*[12]), as defined in ICRU Reports No. 50 and 62 [17, 18].

- **Gross tumor volume**

The Gross tumor volume (GTV) is the tumor that is visible on imaging data (e.g. in CT). As stated in ICRU report 62 [18], It is the"*gross demonstrable extent and location of the malignant growth*"

- **Clinical target volume**

The clinical target volume (CTV) is the tissue that contains the GTV and/or sub-clinical microscopic malignant disease, which has to be eliminated. It is generally a (GTV + a fixed of variable margin).

- **Internal target volume**

The Internal target volume (ITV) consists of the CTV plus an internal margin. The internal margin is designed to take into account the variations in the size and position of the CTV relative to the patient's reference frame (usually defined by the bony anatomy); i.e., variations due to organ motions such as breathing and bladder or rectal contents [18].

- **Planning target volume**

The planning target volume (PTV) is a volume describing the region that should be planned to receive a high dose. This is typically an expansion of the CTV to compensate for patient set-up errors and organ motion. It is a geometric concept introduced in order to ensure that the prescribed dose is delivered to the CTV.

2.5.2 Steps in the radiation therapy planning process

Treatment planning systems (TPSs) are used in radiation therapy to generate beam optimal shape and directions on the patient with the intent to achieve a uniform dose distribution inside the target volume and as low as possible a dose in healthy tissues surrounding the target. The radiation treatment planning process consists of many steps including patient diagnosis, tumor staging, image acquisition for treatment planning, the localization of tumor and normal tissue volumes, optimal beam or source placement, and treatment simulation and optimization. Each of the above step introduces an uncertainty and errors carried through the entire treatment process. Therefore, reducing uncertainty of each step will increase the accuracy of dose delivery. ICRU Report No. 50 [17] recommends a target dose uniformity within +7% and -5% of the dose delivered to a well defined prescription point within the target. The dose delivery can be carried out under one of two set-up conventions: a constant SSD for all beams or an isocentric set-up with a constant source to axis distance (SAD). In a SSD set-up, the distance from the source to patient surface is kept constant during the treatment, while in the SAD set-up, the centre of the target volume is placed at the machine isocentre. In the case of electron beam treatment, the SSD set-up is usually recommended.

- **Patient diagnostic**

The first step in the treatment planning process is the diagnostic performed by a radiation oncologist physician. After this step, if the decision on whether

to treat with radiation is emitted, one can move forward with the process using a particular technique, protocol or set-up.

- **Patient positioning and immobilization (simulation)**

The second step after the decision to treat with radiation is the simulation. In this step, the radiation oncologist and radiation therapist plan out the course of treatment. The patient is move to the simulation (A simulator uses diagnostic X-rays) in order to visualize patient's internal organs and correctly determine the treatment fields. Depending on the part of the body that is treated, an immobilization device may be necessary to prevent any movement during the treatment and is custom made to fit the patient's body. sometimes one place wires on the skin or use a radio-opaque contrast to help define the normal tissues. Marks placed on the skin are to be used as daily references points, therefore, they need to remain in place during the course of treatment.

- **Patient anatomical data acquisition**

This step is focused on the derivation of anatomical informations data generated from some sophisticated imaging modality such as CT or MRI with the intent to determine the target volumes and normal tissues to be sparing. Also, informations derived from nuclear medicine procedures such as single photon emission computed tomography (SPECT) or PET may be used to achieve this goal.

- **Definition of constraints**

In the ICRU 50 [17], developing an optimum treatment plan, with maximum tumor control and minimum normal tissue complications requires a target dose uniformity within +7% and -5% of the dose delivered to a well defined prescription point within the target. To satisfy the above constraints, one needs to define the goals of the plan. Usually, a physician defines the dose to be delivered to the tumor, perhaps with a range of acceptability, e.g., 70 Gy with upper and lower limits of the ICRU stated above.

- **Dose calculation and plan evaluation**

In this step, the dose distribution is calculated in the tissues within the body using relevant information about the patient and the radiation beam. The optimal plan at the end of this stage will be the one that best meets the criteria defined by the radiation oncologist, i.e., the constraints of the plan. In this step known as forward planning, the treatment planner (physicist or dosimetrist) manually optimizes the plan by making some specific adjustments to the treatment variables, such as beam directions, shapes, beam weight and bolus compensator. After the dose distributions are calculated, the plan is evaluated by the radiation oncologist. For a particular treatment, the plan evaluation consists of verifying the treatment portals (through simulation radiographs or DRRs) to ensure that the PTV is targeted adequately and the isodose distribution to ensure that target coverage is adequate and that critical structures surrounding the PTV are well spared. The tools usually used to evaluate a planned dose distribution are Isodose curves, orthogonal planes and isodose surfaces, dose distribution statistics, differential dose volume histogram (DVHs) and cumulative DVHs. Some TPS allow the use of radiobiological model to evaluate tumor control probabilities (TCPs) and normal tissues control probabilities (NTCPs) which lead to an estimation of the quality of the plan.

- **Plan implementation**

In this step, the plan is implemented after an approval by a radiation oncologist. This includes the simulation (plan verification), the monitor unit calculation and the transfer plan to the treatment machine.

- **Treatment plan verification**

This is the last step before dose delivery. When the medical team has completed the treatment plan for the patient, one move to the simulation to confirm the plan specifications. The parameters of the plan are verified prior to the first day of radiation treatment. After the verification is completed, an appointment for the patient's first radiation treatment is scheduled.

2.6 Dose calculation algorithms

The most important component of a TPS is the dose calculation engine incorporated into it. In the past before the incorporation of "fast MC" algorithms as dose calculation engine in the commercial TPS, calculations were relied heavily on analytic, semi-analytic and empirical algorithms. In this section, we limit ourselves to the description of the kernel-based algorithms (convolution/superposition algorithms) and pencil beam algorithms.

2.6.1 Convolution/superposition (Photons)

convolution/superposition (C/S) algorithms also referred as Kernel-based algorithms introduced in 1980s [19-22] separate the effects of primary photons incident upon the patient from the effects of secondary radiations generated by interactions of the primary photons within the patient. Fundamentally, this class of algorithms are based on the general equation bellow [23]

$$D(\vec{r}) = \int \frac{\mu}{\rho}(\vec{s})\Psi(\vec{r}-\vec{s})k(\vec{r}-\vec{s})d^3\vec{s} \tag{2.42}$$

where $\frac{\mu}{\rho}(\vec{s})$ and $\Psi(\vec{r}-\vec{s})$ are the mass attenuation coefficient and the primary photon energy fluence at the interaction point, respectively. The product of $\frac{\mu}{\rho}(\vec{s})$ and $\Psi(\vec{r}-\vec{s})$ given by equation (2.43) represents the total amount of radiation energy available at point $\vec{s}$ for deposition at position $\vec{r}$. This product is known in the acronym of TERMA (Total radiation Energy Released per MAss). $k(\vec{r}-\vec{s})$ is the energy deposition kernel that describes the distribution of the scatter from a primary interaction.

$$T(\vec{r}) = \frac{\mu}{\rho}(\vec{r})\Psi(\vec{r}) \tag{2.43}$$

The total dose distribution is then obtained from a two steps calculation process summarized in the Fig. 2.9:

- In the first step, the total energy released per unit mass (TERMA) from primary photon interactions within the patient is computed. For

the TERMA calculation, inhomogeneities are usually handled from some density scaling methods according to the following relation

$$D(\vec{r}) = \int T(\vec{s}.\rho_{\vec{s}})k(\vec{r}.\rho - \vec{s}.\rho_{\vec{s}})d^3\vec{s} \tag{2.44}$$

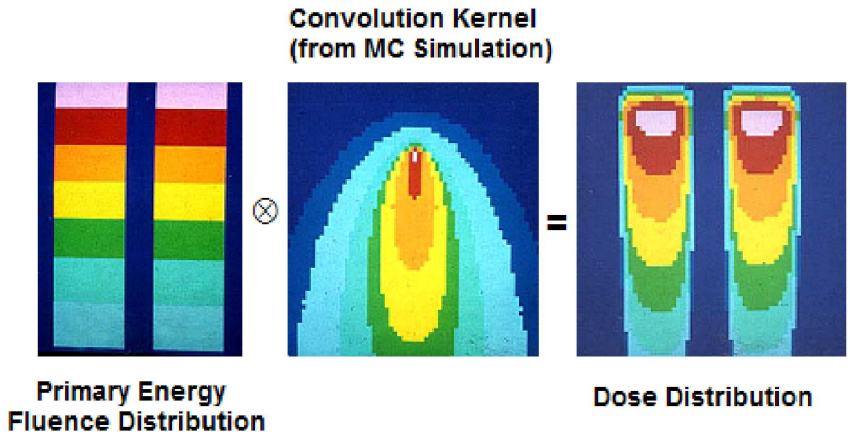

Figure 2.9. Illustration of the C/S method. The dose distribution is obtained from the primary energy fluence convolved with the pre-calculated MC kernels.

- In the second step, precomputed secondary energy spread kernels are then convolved with the TERMA.

The problem with this method is the long time consuming. Therefore, it is usually only applied to compute the final dose distribution at the end of optimization.

2.6.2 Pencil beam algorithms (Electrons)

Before the clinical implementation of MC engines in the commercial TPS to calculate the dose in the patients, most TPSs have been used pencil beam algorithms (PBA) [24, 25] . This class of algorithm is based on the Fermi-Eyges [26] multiple scattering theory. The incoming broad electron beams emerging from the accelerator head is described as a superposition of a number of narrow pencil beams. Mathematically as illustrated in Fig. 2.10,

a broad beam corresponds to a grid or matrix of a finite number of narrow discrete beams with Gaussian distribution in both space and angle. With this

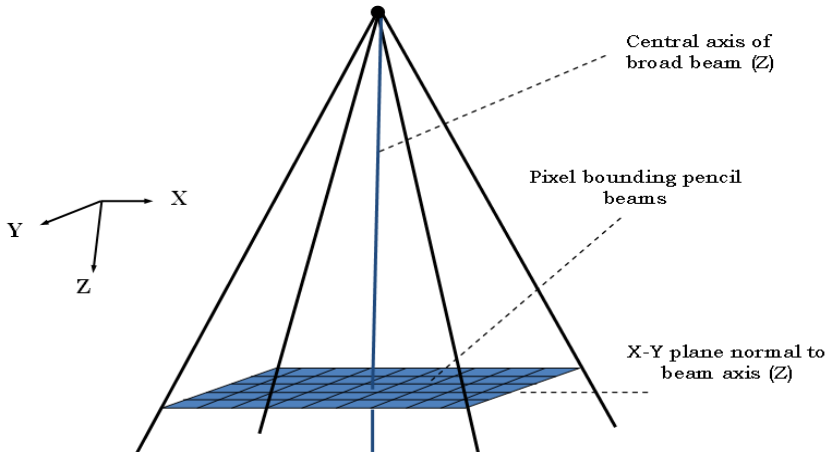

Figure 2.10. Representation of a broad beam into a matrix of a finite number of narrow discrete beams with Gaussian distribution in both space and angle

geometrical representation, each pencil beam is considered to be composed of a particle of passing through an infinitesimal area $\delta x \delta y$. Particles in the narrow symmetric pencil beam have an average angular divergence θ_x and θ_y in both x and y direction, respectively $\left(\theta = \sqrt{\theta_x^2 + \theta_y^2}\right)$. Let be σ_{θ_x} and σ_{θ_y} the average mean square deflection on both θ_x and θ_y. The total dose distribution can then be obtained by summing all contribution of each pencil beam according to the following equation

$$D(x, y, z) = \int \int S(x', y') d(x' - x, y' - y, z) dx' dy' \tag{2.45}$$

In this equation, $S(x', y')$ corresponds to relative strength of the pencil beam at x', y' and $d(x' - x, y' - y, z)$ is the dose contribution at (x, y, z) from the pencil beam at x', y'. The above equation was evaluated by the authors by assuming the incident beam to be a collection of parallel pencil beams incident normally to the collimation plane. The Fig. 2.11 shows a schematic representation in the x-z plane of a therapeutic electron beam incident on a

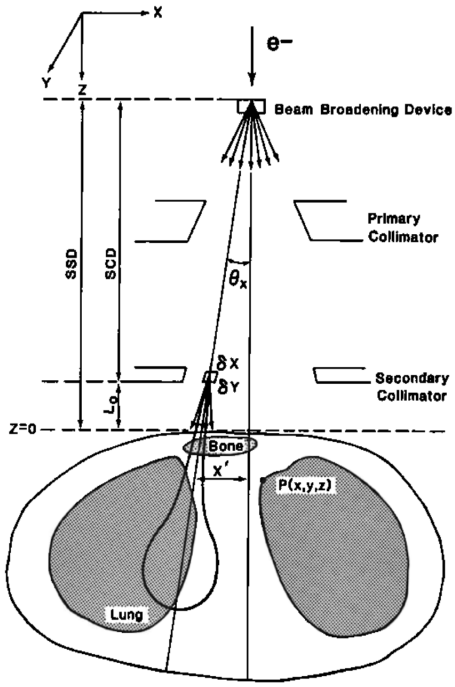

Figure 2.11. Schematic view of the Hogstrom PBA showing that it was modelling beam collimation, air gap (l_0) and internal patient heterogeneity (from Hogstrom et *al.* [24]).

patient.

- **Slab heterogeneities correction**

To account for patient heterogeneities, the authors replaced Fig. 2.11 by a stack of inhomogeneous slabs as pictured in Fig. 2.12, each slab being homogeneous, but of a different material. The dose distribution, d(x, y, z), due to a pencil beam incident normally on that configuration, can be expressed as a product of two components, a central-axis term g(z) and an off-axis term h(x, y, z) as follows

$$d(x, y, z) = h(x, y, z)g(z) \tag{2.46}$$

The off-axis term h(x, y, z), corresponding to the lateral flux distribution due to thick-target multiple Coulomb scattering (MCS) as formulated by the Fermi-Eyges theory and applied to electrons, is given by

$$h(x,y,z) = \frac{1}{2\pi\sigma^2_{MCS}} \exp\left(-\frac{x^2+y^2}{2\sigma^2_{MCS}}\right) \tag{2.47}$$

In the equation (2.47) above, σ^2_{MCS} is the Root Mean Square (RMS) of the lateral distribution which is given by

$$\sigma^2_{MCS} = \frac{1}{2}\int_{-l_0}^{z} (z-z')^2 \frac{d\sigma^2_{MCS}}{dz'} dz' \tag{2.48}$$

where $(d\sigma^2_{MCS}/dz')$ is the linear angular scattering power evaluated at electron energy $E_{z'}$ corresponding to the mean energy of the electron beam at the depth z'. $E_{z'}$ is given by a relation similar to equation (2.39) in which the depth z is replaced by the effective depth, z_{eff}, in the water as follows

$$E(z') = E_0\left(1 - \frac{z_{eff}(z')}{R_p}\right) \tag{2.49}$$

where z_{eff} is given by

$$z_{eff}(z) = \int_{-l_0}^{z} \frac{(dE/dz')}{(dE/dz')_{water}} dz' \tag{2.50}$$

The equation (2.50) was derived from the assumption that the linear stopping power, dE/dz, of the material at z relative to that of water is relatively independent of electron energy for normal body tissues. Due to multiple scattering of electron beam on the different components of the accelerator head (vacuum windows, scatter foils, primary collimator, beam monitors, air, etc), prior to reaching the secondary collimator, each pencil beam has an angular spread at any point in space that is Gaussian according to the Fermi-Eyges theory [24] with an RMS projected scattering angle given by

$$\sigma^2_{\theta_x} = \sigma^2_{\theta_y} = B_0 - B^2/B_2 \tag{2.51}$$

where B_i is the *ith* moment of linear angular scattering power given by equation (2.52) below

$$B_i = \frac{1}{2}\int_0^{SCD}(SCD - z')^i \frac{d\sigma^2_{MCS}}{dz'}dz' \tag{2.52}$$

This RMS angular spread is projected into a lateral spread at depth equal

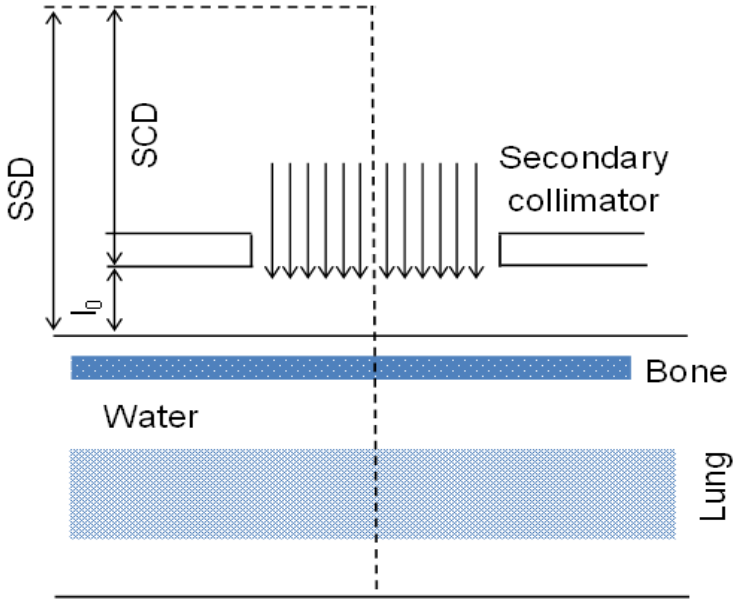

Figure 2.12. Schematic representation in the x-z plane of a model electron beam incident on a stack of infinite slabs of different material. The configuration corresponds to those inhomogeneities underlying the central ray of the pencil beam drawn in figure 2.11.

to $\sigma_{air} = (z + l_0)\sigma_{\theta x}$. The convolution of that Gaussian, σ_{air}, with that due to MCS, σ_{MSC}, gives

$$h(x, y, z) = \frac{1}{2\pi\sigma^2}\exp -\frac{x^2 + y^2}{2\sigma^2} \tag{2.53}$$

where

$$\sigma^2 = \sigma^2_{air} + \sigma^2_{MCS} \tag{2.54}$$

after corrected for the effective depth and inverse square, the depth-dose term of equation (2.46) is assumed to be related to the same depth-dose term in water, g_0, as follows

$$g(z) = g_0(z_{eff})\left[(SSD + z_{eff})/(SSD + z)\right]^2 \tag{2.55}$$

In the case of a uniform incident beam (S = l), g_0 can be obtained from a measured depth-dose curve in a water phantom, D_0, by substituting equations (2.53) and (2.55) into equation (2.45) and where the double integral is evaluated at collimation at z.

$$D_0(x,y,z) = \left(\frac{1}{2\pi\sigma_0^2}\int\int exp - \frac{(x-x')^2 + (y-y')^2}{2\sigma_0^2}dx'dy'\right) \times g_0(z) \tag{2.56}$$

The dose distribution, D(x, y, z), can be calculated for rectangular fields of dimension wx by wy at a given SSD, by solving equations (2.45), (2.53) and (2.55) and assuming a uniform incident beam (S=1) as follows

$$\begin{aligned} D(x,y,z) = \frac{1}{4}&\left(erf\frac{wxz/2 - x}{\sqrt{2}\sigma} + erf\frac{wxz/2 + x}{\sqrt{2}\sigma}\right) \\ &\times\left(erf\frac{wyz/2 - y}{\sqrt{2}\sigma} + erf\frac{wyz/2 + y}{\sqrt{2}\sigma}\right) \\ &\times g_0(z_{eff})\left(\frac{SSD + z_{eff}}{SSD + z}\right)^2 \end{aligned} \tag{2.57}$$

In the equation (2.57) above, wxz and wyz correspond to the projected collimator sizes at z given by wxz =wx(1+ z/SSD) and wyz= wy(1+ z/SSD). $g_0(z)$ is determined from equation (2.56) and measurements of central-axis depth-dose curve $D_0(0,0,z)$ for a square field size $wx\phi$. We then obtain

$$D(x,y,z) = \frac{1}{4}\left(erf\frac{wxz/2-x}{\sqrt{2}\sigma} + erf\frac{wxz/2+x}{\sqrt{2}\sigma}\right) \times \left(erf\frac{wyz/2-y}{\sqrt{2}\sigma} + erf\frac{wyz/2+y}{\sqrt{2}\sigma}\right) \times D_0(0,0,z_{eff})\left(erf\frac{wx\phi z/2}{\sqrt{2}\sigma_0}\right)^{-2}\left(\frac{SSD+z_{eff}}{SSD+z}\right)^2 \tag{2.58}$$

Similarly, in the case of irregular field, one obtains D(x, y, z) from equations (2.45), (2.53) and (2.56) as follows

$$D(x,y,z) = \left(\frac{1}{2\pi\sigma^2}\int\int S(x',y')exp - \frac{(x-x')^2+(y-y')^2}{2\sigma^2}dx'dy'\right) \times D_0(0,0,z_{eff})\left(erf\frac{wx\phi z/2}{\sqrt{2}\sigma_0}\right)^{-2}\left(\frac{SSD+z_{eff}}{SSD+z}\right)^2 \tag{2.59}$$

- **Patient dose calculation**

To compute dose distribution in the patient which is normally an inhomogeneous medium, the authors assumed that the dose contribution from a pencil beam at x', y' to each point of calculation can be made considering the inhomogeneity structure along that ray to be infinite in lateral extent, i.e., they assumed the geometry in Fig. 2.12 for calculating the contribution from the ray drawn in Fig. 2.11 to the dose at every point. Therefore, the equation (2.58) must be modified since σ becomes a function of lateral position (x, y) as well as the depth z, as follows

$$D(x,y,z) = \int\int S_{air}(x'',y'',z)\frac{1}{2\pi\sigma_{MCS}^2}exp - \frac{(x-x'')^2+(y-y'')^2}{2\sigma_{MCS}^2} \times D_0(0,0,z_{eff})\left(erf\frac{wx\phi z/2}{\sqrt{2}\sigma_0}\right)^{-2} \times \left(\frac{SSD+z_{eff}}{SSD+z}\right)^2 dx''dy'' \tag{2.60}$$

where $S_{air}(x'',y'',z)$ given by equation (2.61) represents the flux at depth z in air in the absence of all matter below the collimator.

$$S_{air}(x'', y'', z) = \frac{1}{2\pi\sigma_{air}^2} \int\int S_{air}(x', y') exp - \frac{(x' - x'')^2 + (y' - y'')^2}{2\sigma_{air}^2} \times dx'dy' \tag{2.61}$$

2.6.3 Generalized Pencil beam algorithms

An alternative to the model of Hogstrom et *al.* [24], also based on the Fermi-Eyges theory was developed by Lax et *al.* [28]. Known as Generalized Pencil beam algorithm (GPBA), the developed model gives more accurate results compared to PBA, specially in the penumbra region. Other variants of PB algorithms were developed with the intent to improve patient dose calculation with electron beam [29, 30]. Although each variant of PB leads to an improvement in the patient dose calculation, the major drawbacks of these variants remains the heterogeneities correction and the calculation speed. Fig. 2.13 illustrates errors introduced in the PBA in the presence of inhomogeneities. This can be solved with high accuracy by introducing MC simulation in the TPS as patient dose calculation engine.

2.7 MC simulation in radiation therapy

The MC method in computational physics is possibly one of the most important numerical approaches to study problems spanning all thinkable scientific disciplines. The term MC method was coined in the 1940s by physicists S. Ulam, E. Fermi, J. von Neumann, and N. Metropolis working on the nuclear weapons project at Los Alamos National Laboratory. For the radiation therapy calculations purpose, the MC method can be understood as a numerical solution to a problem that models objects interacting with other objects or their environment based upon simple object-object or object-environment relationships (although there are other uses of the Monte Carlo method for purely mathematical reasons). Therefore, this approach attempts

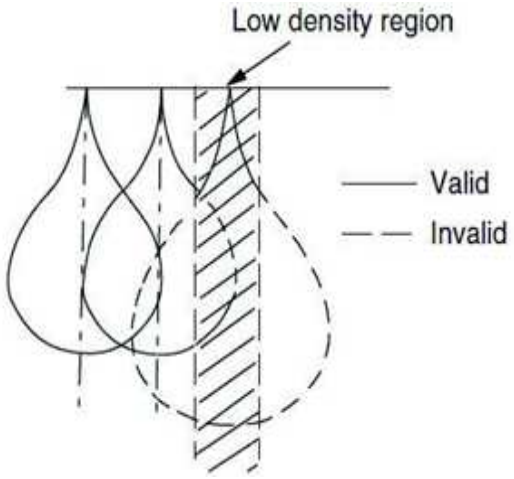

Figure 2.13. Illustration of errors introduced by PBA models in the presence of inhomogeneities, from Nahum [27].

to model nature through direct simulation of the essential dynamics of the system in question. Independently to the problem to be solved, MC methods are stochastic techniques by nature which are based on the use of random numbers generator and a set of basic physics interaction probabilities distributions to sample parameter values for calculating a possible solution to the problem for a single "case" or "event". By simulating the above "case" or "event", reliable average values can be obtained. Every MC result is associated with a standard deviation which expresses the uncertainty due to the fact that the number of "events" or "cases" simulated are not infinite. In the MC simulation of radiation transport, the history (track) of each particle is viewed as a random sequence of free flights that end with an interaction event where the particle changes its initial direction of movement, loses energy and, sometimes, produces secondary particles. For a given experimental arrangement (e.g. an electron beam, coming from an accelerator and impinging on a water phantom), the simulation process consists of the numerical generation of random histories. These histories are simulated from the differential cross sections (DCS) for the relevant interaction mechanisms. The DCSs determine the probability distribution functions (PDFs) of the random variables

that characterize a track. The basic flow of a Monte Carlo simulation for each history can be summarized as follows:

(1) Sample the particle's initial energy, position, and direction from a source PDF;

(2) Sample the distance to the particle's next collision, based on the material(s) through which the particle is being transported. If the distance places the particle outside of the geometry of interest, terminate the particle history (this depends on the voxel dimension in which the interaction occurs);

(3) Sample the interaction from the PDF corresponding to the surrounding material and the particle energy. If the sampled collision results in the particle being absorbed, terminate the particle history. If the particle is not absorbed, sample its outgoing direction and energy. If the particle's outgoing energy is below a cutoff energy, terminate the particle history. If the sampled collision produces a new particle, store the new particle on a stack for its own sampling later. Score a correct deposition of dose in the voxel in which the particle interacted;

(4) Repeat steps two through four until the particle is absorbed or leaves the geometry of interest;

(5) For every extra particle created by a collision in step three, cycle from steps two through five for the new particle until its history is terminated;

(6) Add together all depositions of dose for particles existing in the current history;

(7) Calculate the sum of all history scores, along with respective absolute uncertainties, defined as

$$S_{\overline{x}} = \sqrt{\frac{1}{N-1}\frac{\sum_{i=1}^{N} X_i^2}{N} - \left(\frac{\sum_{i=1}^{N} X_i}{N}\right)^2} \tag{2.62}$$

where N is the number of primary histories and X_i the contribution to the scored dose by independent history i.

(8) Repeat steps one through eight for a total number of histories or until a desired uncertainty is obtained.

The accomplishment of the above steps for each particle requires a long computer time calculation. Due to the limitation of computers power in the past, MC techniques for routine TPS were never a realistic option in a clinical setting and they were mainly used for verification of results obtained with conventional methods, as pointed out by a number of pioneers workers in that matter [23, 31, 32]. Recently, vendors of commercial clinical treatment planning systems have nevertheless started to offer MC dose engine as option for patient dose calculations. However, available computing power may still not allow for full MC simulations in clinical practice. Approximations and simplifications to speed up the calculations is therefore necessary. This led to the development of "fast MC" code for which some of them are based (or partially based) on the available general purpose MC codes, like EGSnrc, PENELOP, GEANT4 and others. We will therefore start with a short description of the above "full MC" codes before the presentation of "fast MC" algorithms available for routine TPS with electron beam. This will be presented next to the following two subsections devoted to the description of photons and electrons transport mechanism.

2.7.1 Photon transport

In general, photon transport modeling is quite similar in the above systems, although different cross section data are used. The important differences, however, appear in the electron transport mechanism, which strongly influences the speed and accuracy of the codes [33]. Let us start with the simulation of the distance that a photon travels before it goes through an interaction. Its probability of traveling a distance l without interacting is given by $\exp(-\mu l)$, whereas μdl is the probability to interact in the interval dl. The two probabilities are related to the probability of the photon un-

dergoing an interaction between l and l + dl by $\mu \exp(-\mu l)dl$. A cumulative probability distribution P(l) for the location of first interaction site is then given by

$$P(l) = \int_0^l \mu \exp(-\mu s)ds = 1 - \exp(-\mu l) \tag{2.63}$$

μ is the attenuation coefficient of the medium. As this cumulative probability distribution of travel distance is between 0 and 1, we can now choose a random number r_1 to extract analytically a traveled distance l as follows

$$r_1 = 1 - \exp(-\mu l) \Rightarrow l = -\frac{1}{\mu} \lg(1 - r_1) = -\frac{1}{\mu} \lg(r') \tag{2.64}$$

This means that the travel distance is distributed between 0 and ∞ with an average of $1/\mu$. To choose the type of interaction, we assume to simplify the description by dealing with low photon beams in which the main interactions are taken as the photoelectric and Compton events. We can then pick a second random number r_2, if $r_2 \succ \mu_{ph}/\mu$ the photon is Compton scattered. Other random number generations are then required to obtain the scatter parameters for further transport. The simulation of this selected interaction is performed using the well-known theories describing this type of interaction. In the case of Compton interaction for example, this requires a sampling over the direction and the energy of the scattered photon. For the photoelectron set in motion in this process, its energy and angular deflection are calculated first before placed into a stack for later transport. When the primary photon is finally fully transported (its energy is completely lost or it has escaped the region of interest), then the other secondary particles are transported further before a new history is started. In the case where the transport is performed on a heterogeneous medium, some frequent situations can occur where the sampled distance to the next interaction exceeds the distance of the nearest boundary materials. In such situations, the photon is first transported to the boundary. Then, the distance to the next interaction in the medium, where the photon is entering, is sampled using the relevant cross section whilst

keeping spatial and energy coordinates. Photon transport can be performed very fast due to their low number of discrete interactions per particle track.

2.7.2 Electron transport mechanism

The electron transport mechanism is different from the photon one. The main difference lies on the fact that electrons undergo a very high number of Coulomb interactions with electrons and atomic nuclei of the medium. Simulation of every individual interaction would be computationally extremely intensive. Therefore, electron transport is performed on a so-called "condensed history" (CH) approach [34]. In this CH scheme, an electron track is divided into a serie of short track segments, usually called "steps". Instead of simulation of every individual interaction along each step, the cumulative angular deflection and energy loss are sampled once per step. The sampling of angular deflection is governed by the so-called multiple-scattering formalism. The sampling of energy loss may be performed on different ways. A distinction is commonly made between so-called class I and class II algorithms [34, 35]. In CH scheme (class I algorithm) the primary electron is not directly influenced by the generation of a secondary electron, whereas in the class II code (e.g. EGS), the energy loss and angular deflection of the primary electron are directly affected by the generation of the secondary electron. The main advantage of this approach is that the creation of knock-on electrons is simulated in a way that is analogous to reality. The reader is referred to the ref. [34, 35] for more detail.

2.8 General Purpose MC in radiation therapy

2.8.1 EGS user code

The EGS (Electron−Gamma−Shower) system of computer codes is a general purpose package for the MC simulation of the coupled transport of electrons and photons in an arbitrary geometry for particles in the wide range of energies (from a few keV up to several hundreds of GeV). The first version of

EGS was developed in the early 1970's by Ford and Nelson. It was then benchmarked against various experiments and compared to other MC results, and found to have good agreement. Since then, the code has been successively improved by several pioneers workers [36, 37], and in 2000 the EGSnrc code was released By Kawrakov and Rogers [38] as a successor to the EGS4 version. In the EGS4 version [36], the Molière multiple scattering theory is used, which is only valid for small scattering angle, while in the EGSnrc, an improved multiple scattering theory based on screened Rutherford elastic scattering is used. Additionally, this code uses PRESTAII. The main changes from PRESTA to PRESTAII is the introduction of a single scattering model of electron transport, making it possible to reduce the electron step length to very small values near material boundaries.

2.8.2 BEAMnrc

BEAMnrc [39] is a general purpose MC simulation system developed at the National Research Council of Canada for modeling radiotherapy units. BEAMnrc is based on the EGSnrc code system for modeling coupled electron and photon transport. The design philosophy of the code is that, the accelerator head has to be broken into a series of individual component modules (CMs). Each CM operates completely independently of each other and occupies a slab at right angle to the beam axis. For the simulation of the ELEKTA SL25 medical linear accelerator, the accelerator head was broken into eleven component modules (CMs), which represent the exit window (SLABS), primary scattering foil (SLABS), primary collimator (CONS3R), secondary flattening foil (CONESTAK), monitor chamber (CONESTAK), mirror (MIRROR), upper jaws (MLCQ), lower jaw (Jaw), Milar screen (SLABS), and applicator (APPLICAT and BLOCK). The BEAMnrc CMs used for the simulation are indicated into brackets. For each CM, the dimensions, materials and transport parameters have be defined in an input file. The output from BEAMnrc simulation is the phase space file created at the so-called "scoring plane". This phase space contains information about the position (X,Y,Z), direction (U,V,W), energy, type and origin (LATCH)

of each particle crossing it. Such files can then be used as input for further BEAMnrc simulations or for dose calculations within a phantom or patient (derived from a CT dataset) using the other pre-programmed user code, designated DOSXYZnrc [40]. In this code, CT data can be imported and translated into voxels with a certain material composition and density using a stand-alone program CTCREATE. Material and mass density data are derived from the Hounsfield number within each voxel. Several CT data set formats are supported, including DICOM.

2.8.3 PENELOPE

The code PENELOP which is an acronym for PENetration and Energy LOss of Positron and Electrons has ben introduced in 1990s [41] and later by Salvat et *al.* [1]. PENELOP was developed for the simulation of coupled transport of electrons, positron and photons with energies ranging from a few hundred eV to about 1 GeV. The code is capable of handling complex geometries and static electromagnetic fields. A lot of efforts were made to make the simulation of electron transport as accurate as possible. Photon transport is simulated by means of the standard, detailed simulation scheme. Compared to the EGSnrc system, the code uses a mixed scheme of single and multiple scattering which are based on the Goudsmit-Saunderson theory. In the implementation of multiple scattering in PENELOPE, the angular deflection and the lateral displacement for each electron step are accounted for using the so-called random hinge method. This is known to be a simple and fast method for obtaining an accurate geometric representation of the electron track. As stated in the two previous subsection, EGS and PENELOPE simulate the coupled transport of photons, electrons and positrons. Other particles such as neutrons or protons are not taken into account. This means that, during their development, all attention has been focused on the particles of interest for radiotherapy dose planning. This is a limitation of the above codes since, at high energy photon beams (18 MV and higher), the production of neutrons and protons in the accelerator head may impact (the biological effect) the physical dose distribution in the patient, espe-

cially in bone where even alpha particles have a non-negligible contribution as pointed out by Chibani et *al.* [42].

2.8.4 GEANT4

GEANT4 (GEometry ANd Tracking) [43] was originally developed as a toolkit for high energy detector simulations and therefore, for high energy physics processes for electromagnetic, hadronic and optical interactions. Its was also expanded towards low energy physics which make it useful for radiation therapy applications. GEANT4 consists of a broad collection of C++ class libraries delivering very high exibility for its users. It is equipped with geometry tools which also permit the use of computer aided design tools. Some benchmarks of this code against other MC codes or measurements have shown good agreement for photons [44, 45] while fair agreements were reported for electrons [44, 46]. Another drawback of GEANT4 is the calculation speed, which is relatively slower compared to EGSnrc.

2.9 Fast MC dose calculation engine for TPS

A fast and accurate treatment planning system is essential for radiation therapy if one needs to reduce as much as possible the overall uncertainty in the patient dose delivery. As already pointed out, the general purpose MC codes presented in the previous sections are not suitable for TPS despite their high accuracy. This is due to their computer time consuming. This has motivated the development of the so-called Fast MC in which several variance reduction techniques, approximations and simplifications, are included in order to reduce computing time while maintaining a reasonable level of accuracy.

2.9.1 Voxel MC (VMC)

The VMC (Voxel Monte Carlo) algorithm was originally developed for electron transport by Kawrakow et *al.* [47]. This algorithm applies some approximations and simplifications into the electron transport process. One

of the main approximations of VMC is a simplified treatment of multiple scattering compared to EGSnrc. The VMC code is very fast and produces good results and it has been improved from its original version [48]. The significant speed improvements are due to an efficient boundary crossing algorithm, variance reduction techniques such as particle splitting, Russian roulette and history repetition. The use of other optimized transport parameters like the electron cut-off, maximum electron energy step size, photon energy cut-off and a cut-off for kerma approximation can further improve the efficiency defined as follows

$$\epsilon = \frac{1}{\sigma^2 T} \tag{2.65}$$

where T is the computing time and σ the statistical uncertainty. Briefly, the VMC algorithm can be described as follows:
The simulation of the accelerator head need a fluence distribution on the patient surface, $F(E, \vec{\beta}_0, \vec{r}_0)$, for a given energy and adjustment of collimator, applicator, tube, SSD, etc. F can be obtained from full MC simulation. However, the simulation of the accelerator head prior to dose calculation would require a lot of computing time or memory. An alternative approach has been applied by the authors to solve the problem. They assumed that F can be split into two independents components, an energy component $F_1(E)$ and angle and spatial component $F_2(\vec{\beta}_0, \vec{r}_0)$ such as

$$F(E, \vec{\beta}_0, \vec{r}_0) = F_1(E) F_2(\vec{\beta}_0, \vec{r}_0) \tag{2.66}$$

From this assumption, the calculated dose distribution in the water can be obtained by the following equation

$$D(\vec{r}) = D_\gamma(\vec{r}) + \int dE F_1(E) \tilde{D}(E; \vec{r}) \tag{2.67}$$

where $\tilde{D}(E; \vec{r})$ represents the dose distribution of a monoenergetic broad beam described by F_2, and $D_\gamma(\vec{r})$, the dose resulting from the photons escaping the accelerator and produced in the water phantom. The energy

spectrum function $F_1(E)$ is fixed from the requirement that the deviations between the calculated and the measured dose, D_{exp}, become as small as possible. A suitable estimation of the deviation can be determined from the following equation

$$\chi^2 = \sum_{i=1}^{N} [D(z_i) - D_{exp}(z_i))]^2 \tag{2.68}$$

The sum in the above equation covers the range of all measured depth dose values. The energy spectrum of the accelerator is thus fixed from the minimization of χ^2. The authors used a very simple form of $F_1(E)$ given by equation (2.69)

$$F_1(E) = A\left[\alpha\left(1 + \frac{E}{E_{min}}\right) + \frac{1}{(E_X - E)^2}\right], \quad E_{min} \leq E \leq E_p \tag{2.69}$$

where α, E_{min}, E_p and E_X are the free parameters obtained from the χ^2 minimization. A is a normalization coefficient resulting from the condition

$$\int_{E_{min}}^{E_p} dE F_1(E) = 1 \tag{2.70}$$

The photon background was described by a simple model given by the following equation

$$D_\gamma(z) = a_\gamma(z - z_0) + b_\gamma \tag{2.71}$$

where a_γ and b_γ are fixed from the measured depth dose for $z \succ R_p + 1$ cm. The distribution function, F_2, was determined assuming a point source uniformly distributed radiation. For a given SSD of d_{SSD} and field size a_x and a_y, F_2 is given by

$$F_1(\theta_x, \theta_y, x_0, y_0) = \frac{\delta(x_0 - d_{SSD}tan\theta_x)\delta(y_0 - d_{SSD}tan\theta_y)}{4\theta_x^{max}\theta_y^{max}} \tag{2.72}$$

where δ denotes the Dirac delta function, $\theta_x^{max} = atan\,(a_x/2d_{SSD})$ and $\theta_y^{max} = atan\,(a_y/2d_{SSD})$.

2.9.2 X-ray Voxel MC (XVMC)

As stated in the previous subsection, the VMC algorithm was originally developed for electrons transport and then extended to photons transport and named XVMC [49]. XVMC was further optimized by Kawrakov and Fippel [50] in 2000. In XVMC, the photon transport mechanism is speed up using several variance reduction techniques and the beam collimating devices are handled by Full MC transport (although electrons transport are modeled from the continuous slowing down approximation (CSDA) approach). Originally, by using the cut-off parameter, the energy of an electron was deposited locally when its energy was less than the cut-off value. A new approach was introduced in which the track-end electrons instead are transported by their residual range in a single "normal" condensed history step. Although this modification increases the computing time, it allows higher cut-off energies, so that on balance, the speed is increased. This XVMC algorithm has been introduced in the commercial XiO eMC TPS developed by ELEKTA CMS SOFTWARE group (ECMSSG). To be used as eMC dose engine in the XiO TPS, the base code was modified by ECMSSG in order to greatly extend its modeling capabilities. For instance, a flexible and expandable set of primary source modeling routine was developed to provide accurate reproduction of broad variety of incident electron beam's characteristics. An electron fluence function was included in order to account for electron scattering in air.

2.9.3 VMC++

VMC++ was introduced by Kawrakow [51] in 2000 with the C++ programming language using an object oriented design. VMC++ is a package for the class II CH MC simulation of coupled electron-photon transport optimized for three dimensional patient dose calculations. All variance reduction techniques of VMC and XVMC are conserved and several improvements in the

modeling of underlying physical processes have been included, namely:

- The use of the exact multiple elastic scattering theory employed in EGSnrc;
- The use of STOPS technique, a newly developed variance reduction technique, instead of history repetition;
- The use of quasi-random sequences for radiotherapy class MC simulations already discussed by Kawrakow and Matthias [50] for photon beams was extended to electron beams and to the transport of electrons set in motion by photons (in external photon beams or bremsstrahlung photons);
- The refinements in the simulation of various scattering processes such as Compton scattering.

To speed up calculations, the code uses also the so-called directional radiative splitting (DRS). This technique is an advanced particle splitting method which consists to split bremsstrahlung photons generated in the target into N sub-particles. Photons that are not pointed to a pre-defined region of interest are handled with Russian roulette, hence the technique ensures that less calculation time is spent on photons (and corresponding secondary electrons) that will not reach the patient. VMC++ has been implemented as a dose calculation engine in the commercial TPS, Oncentra MasterPlan (OMTPS), developed by Nucletron for patient dose computation with electron beams.

2.10 Bibliography

[**1**] Salvat F, Fernández-Varea JM, Sempau J. Penelope - A code system for Monte Carlo simulation of electron and photon transport, Workshop Proceedings, Issy-les-Moulineaux, France, 7-10 July, 2003.

[**2**] Klein O, Nishina T. Über die Streuung von Strahlung durch freie Elektronen nach der neuen relativistischen Quantendynamik von Dirac. Z Phys 1929;52:853-69.

[**3**] Born M. Atomic Physics (Blackie and Son, London), 1969.

[**4**] Motz JW, Olsen HA, Koch HW. Pair production by photons. Rev Mod Phys 1969;41:581-639.

[**5**] Tsai YS. Pair production and bremsstrahlung of charged leptons. Rev Mod Phys 1974;46:815-51.

[**6**] Schiff LI. Quantum Mechanics, 3rd edition (McGraw-Hill Kogakusha Ltd., Tokyo), 1968.

[**7**] Davies H, Bethe HA, Maximon LC. Theory of bremsstrahlung and pair production. II. Integral cross section for pair production. Phys Rev 1954;93: 788-95.

[**8**] Møller C. Zur Theorie des Durchgands Schneller Elektronen Durch Materie. Ann Physik 1932;14:531-85.

[**9**] Mott NF, Massey HSW. The theory of atomic collisions, 3rd edition, (Oxford University Press) 1965: p. 817.

[**10**] Johns HE, Cunningham JR. The Physics of Radiology. Thomas, Illinois, 4th edition, 1983.

[**11**] ICRU. Report 35. Radiation dosimetry: Electron beams with energies between 1 and 50 MeV. International Commission on Radiation Units and Measurement, 1984.

[**12**] Radiation Oncology Physics: A Handbook for Teachers and Students

Radiation Oncology Physics, edited by Podgorsak EB. (IAEA Vienna, 2005)

[**13**] Ding GX, Rogers DWO, Mackie TR. Calculation of stopping-power ratios using realistic clinical electron beams. Med Phys 1995;22:489-501.

[**14**] Harder D. Energiespektren schneller Elekronen in verschiedenen Tiefen Symp. On High-Energy Electrons edited by A. Zuppinger and G. Poretti (Berlin: Springer, 1965), p 260.

[**15**] Gerbi BJ, Antolak JA, Deibel FC, Followill DS, Herman MG et al. Recommendations for clinical electron beam dosimetry: Supplement to the recommendations of Task Group 25. Med Phys 2009;36:3239-79.

[**16**] Prescribing, Recording and Reporting Photon Beam Therapy, Rep. 50, ICRU, Bethesda, MD (1993).

[**17**] Prescribing, Recording and Reporting Photon Beam Therapy, Rep. 50, ICRU, Bethesda, MD (1993).

[**18**] Prescribing, Recording and Reporting Photon Beam Therapy (Supplement to ICRU Report 50), Rep. 62, ICRU, Bethesda, MD (1999).

[**19**] Mackie TR, Scrimger JW, Battista JJ. A convolution method of calculating dose for 15-MV x rays. Med Phys 1985;12:188-96.

[**20**] Boyer A, Mok E. A photon dose distribution model employing convolution calculations. Med Phys 1985;12:169-77.

[**21**] Mohan R, Chui C, Lidofsky L. Differential pencil beam dose computation model for photons. Med Phys 1986;13:64-73.

[**22**] Ahnesjo A. Collapsed cone convolution of radiant energy for photon dose calculation in heterogeneous media. Med Phys 1989;16:577-92.

[**23**] Ahnesj*ö* A, Aspradakis MM. Dose calculations for external photon beams in radiotherapy Phys Med Biol 1999;44:R99-155.

[**24**] Hogstrom KR, Mills MD, Almond PR. Electron beam dose calcula-

tions. Phys Med Biol 1981;26:445-59.

[**25**] Brahme A. Current algorithms for computed electron beam dose planning. Radiother Oncol 1985;3:347-62.

[**26**] Eyges L. Multiple scattering with energy loss. Phys Rev 1948;74:1534-5.

[**27**] Nahum AE. Overview of photon and electron Monte Carlo in Monte Carlo Transport of Electrons and Photons, edited by Jenkins TM, Nelson WR, Rindi A, Nahum AE and Rogers DWO (Plenum Press, New York,1988), p. 3-20.

[**28**] Lax I, Brahme A, Andreo P. Electron beam dose planning using Gaussian beams. Improved radial dose profiles. Acta Radiol Suppl 1983;364:49-59.

[**29**] Electron beam dose planning using Gaussian beams. Energy and spatial scaling with inhomogeneities.Acta Radiol Suppl 1985;24:75-85.

[**30**] Shiu AS, Hogstrom KR. Pencil-beam redefinition algorithm for electron dose distributions. Med Phys 1991;18:7-18.

[**31**] Mackie TR. New developments in radiotherapy dose planning Proc. 17th Int. Cong. Radiology, Paris, p. 30.

[**32**] Ahnesj*ö* A, Aspradakis MM. Topical Review: Dose calculations for external photon beams in radiotherapy Phys Med Biol 1999;44:99-155.

[**33**] Reynaert N, Van der Marck S, Schaart D, Van der Zee W, Tomsej M, van Vliet-Vroegindeweij C, Jansen J, Coghe M, De Wagter C, Heijmen B. Monte Carlo treatment planning: an introduction. Report 16 of the Netherlands Commission on Radiation Dosimetry (NCS). Delft: NCS. 2006.

[**34**] Berger MJ. Monte Carlo calculations of the penetration and diffusion of fast charged particles. Methods in Computational Physics, Academic Press, New York. 1963;1:135-215.

[**35**] Rogers DWO, Bielajew AF. Monte Carlo transport of electrons and

photons. In: Jenkins, T.M., Nelson, W.R., Rindi, A. (Eds.), A Comparison of EGS and ETRAN Monte Carlo Transport of Electrons and Photons. Plenum Press, New York. 1988: p. 323-344.

[**36**] Nelson WR, Hirayama H, Rogers DWO. The EGS4 Code System, Report SLAC-265, Stanford Linear Accelerator Center, Stanford, California, 1985.

[**37**] Bielajew AF, Hirayama H, Nelson WR, Rogers DWO. History, overview and recent improvements of EGS4. National Research Council of Canada Report PIRS-0436, 1994.

[**38**] Kawrakow I, Rogers DWO. The EGSnrc Code System: Monte Carlo simulation of electron and photon transport, Technical Report PIRS-701, National Research Council of Canada, Ottawa, Canada, 2000.

[**39**] Rogers DWO, Faddegon BA, Ding GX, Ma CM, We J, Mackie TR. BEAM: a Monte Carlo code to simulate radiotherapy treatment units. Med Phys 1995;22:503-24.

[**40**] Walters BRB, Rogers DWO. DOSXYZnrc User Manuel, National Research Council of Canada, Ottawa, NRCC Report No. PIRS-794 rev A: 2004.

[**41**] Sempau J, Acosta E, Baro J, Fernandez-Varea JM, Salvat F. An algorithm for Monte Carlo simulation of coupled electron-photon transport, Nucl Instrum Methods B 1997;132:377-90.

[**42**] Chibani O, Ma CM. Photonuclear dose calculations for high-energy photon beams from Siemens and Varian Linacs. Med Phys. 2003: 30; 1990-00.

[**43**] Agostinelli S, Allison J, Amako K et al. GEANT4 A simulation toolkit. Nucl Instr Meth Phys Res A 2003; 506:250-303.

[**44**] Carrier JF, Archembault L, Beaulieu L. Validation of GEANT4, an object-oriented Monte Carlo toolkit for simulations in medical physics. Med Phys 2004;31:484-92.

[**45**] Rodrigues P, Trindade A, Peralta L, Alves C, Chaves A, Lopes MC. Application of GEANT4 radiation transport toolkit to calculations in anthropomorphic phantoms. Applied Radiation and Isotopes. 2004;61:1451-61.

[**46**] Torres J, Buades MJ, Almansa JF, Guerrero R, Lallena AM. Dosimetry characterization of ^{32}P intravascular brachytherapy source wires using Monte Carlo codes PENELOPE and GEANT4. Med Phys 2004;31:296-04.

[**47**] Kawrakow I, Fippel M, Friedrich K. 3D Electron Dose Calculation using a Voxel based Monte Carlo Algorithm. Med Phys 1996;23:445-57.

[**48**] Kawrakow I, Bielajew AF. "On the presentation of electron multiple-scattering distributions for Monte Carlo calculations". Nucl Instrum Methods Phys Res B 1998;134:325-36.

[**49**] Fippel M. Fast Monte Carlo dose calculations for photon beams based on the VMC electron algorithm. Med Phys 1999;26:1466-75.

[**50**] Kawrakow I, Fippel M. Investigation of variance reduction techniques for Monte Carlo photon dose calculations using XVMC. Phys Med Biol 2000;45:2163-83.

[**51**] Kawrakow I. VMC++, Electron and photon Monte Carlo calculations optimized for Radiation Treatment Planning in "Advanced Monte Carlo for Radiation Physics, particle transport simulation and applications", Proceedings of the Monte Carlo conference, Lisbon, 23-26 October 2000, p. 229-36.

Chapter 3

Publication 1: Evaluation of a commercial VMC++ MC-based TPS

Physica Medica (2009) 25, 111-121

ORIGINAL PAPER

Evaluation of a commercial VMC++ Monte Carlo based treatment planning system for electron using EGSnrc/BEAMnrc simulations and measurements

P. Edimo[a, b], C. Clermont[a], M.G. Kwato[b], S. Vynckier[a]

[a]Radiotherapy Department, Université catholique de Louvain, Cliniques Universitaires Saint-Luc, Avenue Hippocrate 10, B-1200 Brussels, Belgium
[b]University of Douala, Centre for Atomic Molecular Physics and Quantum Optics, P.O. Box 8580 Douala, Cameroon

---

Thesis submitted in fulfillment of the requirements for the degree of "Docteur en Sciences Médicales - Orientation : Physique Médicale" - september 11, 2012.

Received 26 November 2007; received in revised form 1 July 2008; accepted 4 July 2008
Available online 21 August 2008

Abstract

In the present work, Monte Carlo (MC) models of electron beams (energies 4, 12 and 18 MeV) from an Elekta SL25 medical linear accelerator were simulated using EGSnrc/BEAMnrc user code. The calculated dose distributions were benchmarked by comparison with measurements made in a water phantom for a wide range of open field sizes and insert combinations, at a single source-to-surface distance (SSD) of 100 cm. These BEAMnrc models were used to evaluate the accuracy of a commercial MC dose calculation engine for electron beam treatment planning (Oncentra MasterPlan Treament Planning System (OMTPS) version 1.4, Nucletron) for two ener, 4 and 12 MeV. Output factors were furthermore measured in the water phantom and compared to BEAMnrc and OMTPS. The overall agreement between predicted and measured output factors was comparable for both BEAMnrc and OMTPS, except for a few asymmetric and/or small insert cutouts, where larger deviations between measurements and the values predicted from BEAMnrc as well as OMTPS computations were recorded. However, in the heterogeneous phantom, differences between BEAMnrc and measurements ranged from 0.5 to 2.0% between two ribs and 0.6-1.0% below the ribs, whereas the range difference between OMTPS and measurements was the same (0.5-4.0%) in both areas. With respect to output factors, the overall agreement between BEAMnrc and measurements was usually within 1.0% whereas differences up to nearly 3.0% were observed for OMTPS. This paper focuses on a comparison for clinical cases, including the effects of electron beam attenuations in a heterogeneous phantom. It, therefore, complements previously reported data (only based on measurements) in one other paper on commissioning of the VMC++ dose calculation engine.
These results demonstrate that the VMC++ algorithm is more robust in predicting dose distribution than Pencil beam based algorithms for the elec-

tron beams investigated.

KEYWORDS: Monte Carlo; Electron beam dosimetry; Electron treatment planning; Output factors

3.1 Introduction

The aim of radiotherapy is to deliver enough radiation to the tumor so as to destroy it while maintaining the dose to the surrounding tissues as low as possible. Accurate knowledge of dose distributions for electron beam radiotherapy treatment is still challenging because electron scattering is strongly affected by changes in density and composition in the patients. Since accurate dose calculations in the patient is one of the major steps in the radiotherapy treatment planning process, many problems in radiation dosimetry have been addressed by the Monte Carlo (MC) technique because the complexity of electron and photon transport in matter renders analytical solutions intractable. Several investigations have reported discrepancies of up to 40% in the calculated dose distributions [1-6] with respect to measurements or MC computations, especially when the irradiated volume contains heterogeneities of low (lung and air cavities) or high (bone structures) densities. MC methods are considered as the most accurate approach of performing many radiations dosimetry calculations and, thus, can reduce these uncertainties up to an accuracy of acceptance levels (2%/2 mm and 3%/3 mm, for small dose gradient/large dose gradient in the homogeneous phantom and heterogeneous phantom, respectively) suggested by the Netherlands Commission on Radiation Dosimetry subcommittee, NCS Report 15 [7]. This level of accuracy, and an even better one, can be achieved from accurate knowledge of information about the beam characteristics such as energy, angular and spatial distributions of the particles in the clinical beam. One way to determine the electron beam characteristics is to simulate their transport through the treatment head of a clinical linear accelerator used in radiotherapy. A number of groups have attempted to model various

linear accelerators by using this technique for many purposes [8-13] thus, demonstrating the usefulness of MC simulation in radiation therapy. One of the important developments in the MC technique was the release of the BEAMnrc [14] user code based on EGSnrc [15] coupled photone-electron transport code system developed at the National Research Council (NRC) of Canada for modeling radiotherapy units. As the MC method is by its nature very time consuming and impractical for radiotherapy applications, a number of approximations and simplifications to speed up calculations have been included in the commercial MC dose calculation engines, leading to the development of fast MC algorithms [16-21]. The clinical implementation of these three dimensional (3D) fast electron beam dose calculation engines requires performing a careful evaluation to find their accuracy and their limits. This has been the subject of interest for several teams for a limited number of medical linear accelerators [22-26]. In March 2006, Nucletron released a new version "MasterPlan version 1.4, Service Pack 4" treatment planning system which implements a VMC++ Kawrakow's algorithm [16, 17] for electron beam dose calculation. Due to the lack of reported data in the literature for MC modeling of an Elekta accelerator on the one hand and the evaluation of the accuracy of the new release of Oncentra MasterPlan treatment planning system (OMTPS) for Elekta series on the other hand, we used measurements, BEAMnrc MC simulations and OMTPS calculations to investigate dose distributions and output factors in the electron beams from an Elekta SL25 medical linear accelerator used for routine patient treatment in our Radiotherapy Department. Percentage depth dose and off-axis profiles were measured in a homogeneous water phantom, for a wide range of open field sizes and several insert cutouts at a single source-to-surface distance (SSD) of 100 cm, for three clinical energies 4, 12 and 18 MeV. Our BEAMnrc MC models were validated against homogeneous water phantom measurements and compared to OMTPS predictions. The accuracy of OMTPS in reproducing dose perturbations in the presence of heterogeneities of high density has been investigated in this work by studying the effects of electron beam attenuation in a heterogeneous phantom simulating a patient's

thorax. Results obtained from OMTPS calculations in the thorax phantom were benchmarked by comparison with BEAMnrc computations and KODAK EDR2 film measurements. Commissioning of the VMC++ dose calculation engine has already been investigated by Cygler et *al.* [23], however, the results of their previous publication are only based on measurements. Our approach uses both measurements and MC simulation to investigate the accuracy of OMTPS calculations at very low (4 MeV) and high (12 MeV) electron beam energies, in both a homogeneous water phantom and a heterogeneous phantom constructed of tissue equivalent materials, with densities close to realistic human tissues and appropriate dimensions.

3.2 Materials and methods

3.2.1 Dosimetry measurement

Homogeneous water phantom measurements

In order to evaluate the accuracy of our BEAMnrc MC models, dose distributions, i.e., central axis depth dose and off-axis profiles, as well as output factors were measured in the water phantom using a Wellhöfer data acquisition system. Measurements were carried out for open field sizes of 6×6 cm^2, 10×10 cm^2, 20×20 cm^2 and 10 insert cutouts with sizes ranging from 3×3 cm^2 to 14×14 cm^2, at a single SSD of 100 cm. All correction factors such as effective detector position and water/air stopping-power ratios were performed in accordance with the recommendations of the IAEA, TRS 398 protocol [27]. Percentage depth dose and off-axis profiles were measured with a Wellhöfer type CC01 thimble ionization chamber having 0.01 cm^3 collecting volume. Output factors measurements at the depth of maximum dose, d_{max} obtained from percentage depth dose measurements, were performed with two ionization chambers; a plane parallel ionization chamber type NACP17-02, active volume 0.16 cm^3, for large field size measurements and a Scanditronix- Wellhöfer IC13 thimble ionization chamber, having a cavity volume of 0.13 cm^3, for measurements in small field sizes. Depth

ionization curves were converted to the percentage depth dose by multiplying the ionization charge at each measurement depth by the corresponding water/air stopping-power ratios derived from the IAEA, TRS 398 protocol [27]. All cross-beam profiles were measured at d_{max} and at the depth R_{50} at which the dose at the central axis falls off by 50% of the maximum dose. In the present work, output factors (OF) for a given beam energy E, field size S and SSD, are defined as the ratios of the maximum dose D_{max}(E, S, SSD) along the central axis of the field of interest to the maximum dose D_{max}(E, 10×10 cm^2, SSD), where 10×10 cm^2 is our reference field size.

Heterogeneous phantom measurements

We used the thorax phantom constructed by Seutjens et *al.* [28], which has densities close to realistic human tissues and appropriate dimensions (see Fig. 3.1) and which they used in their study of the comparison of measured and calculated dose distributions in lung tissue after electron beam treatment of the chest wall. The phantom is composed of three layers of tissues-equivalent materials with thickness obtained from averaged measurements on CT-scan of a group of 18 patients performed by the authors. The first layer with 11 mm thickness is polyethylene (density 0.96 g/cm^3) simulating adipose tissue, followed by 12 mm PMMA material representing muscle (density 1.18 g/cm^3) in which a series of equidistant solid Teflon cylinders (simulating ribs) having a mass density 2.13 g/cm^3 with 8 mm diameter (center-to-center distance of 20 mm) are embedded. The 16 cm-thick third layer is composed of cork material having a mass density of 0.25 g/cm^3 for the simulation of lung tissue. The accuracy of OMTPS calculation in the presence of heterogeneities was investigated from off-axis profile measurements in the thorax phantom described above and results were compared both to BEAMnrc calculations and measurements. Measurements were carried out with KODAK EDR2 film dosimeters at various depths, spaced by 1 cm for 12 MeV and 0.5 cm for 4 MeV beam. The field sizes were defined by cutouts 6×6, 10×10 and 14×14 cm^2 inserted in the 20×20 cm^2 applicator. This enabled the quantification of both the effect of heterogeneities in dose

distribution in lung tissue and the accuracy of OMTPS in reproducing dose perturbations in the presence of heterogeneities of high density such as bone structures irradiated with electron beam from a SL25 Elekta linear accelerator. The normalization was performed at the average dose, D_{av}, as follows:

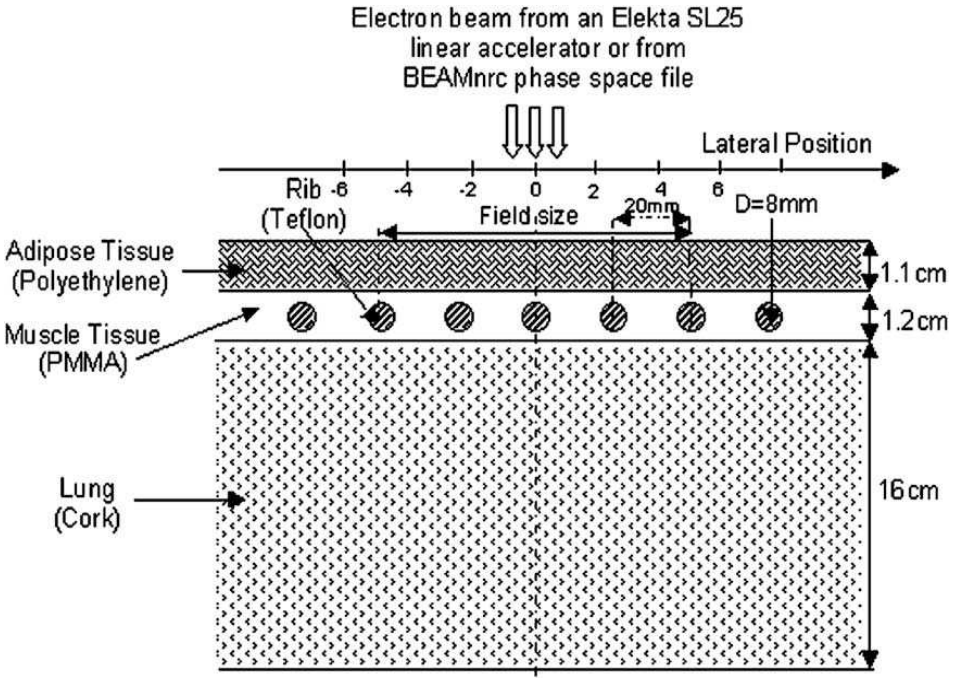

Figure 3.1. Graphic representation of the thorax phantom. It consists of three layers of different tissue equivalent materials: adipose tissue (polyethylene, density 0.96 g/cm^3), striated muscle (PMMA, density 1.18 g/cm^3) in which a series of equidistant solid Teflon cylinders (simulating ribs), with a mass density of 2.13 g/cm^3 and an 8 mm diameter (center-to-center distance of 20 mm), are embedded. The third layer (16 cm-thick) is composed of cork material (cork, density 0.25 g/cm^3) simulating lung tissue.

for each field size at the depth of interest, let D_{max} be the average maximum dose between two ribs and D_{min} the average minimum dose beneath the ribs, respectively. D_{max} and D_{min} are calculated from equations (3.1) and (3.2)

as follows:

$$D_{max} = \left(\frac{1}{m}\right) \sum_{j=1}^{m} D_{max}(j) \tag{3.1}$$

$$D_{min} = \left(\frac{1}{m-1}\right) \sum_{j=1}^{m-1} D_{min}(j) \tag{3.2}$$

where "m" is the number of maximum peaks dose involved in each field size at the depth of interest. The normalization has been performed at the average dose D_{av}=(D_{max}+D_{min})/2. Conversion of optical density to dose was based on the calibration curves established for both 4 and 12 MeV electron beam energies. Calibration was performed in a polystyrene phantom material. Films were positioned at the reference depth Z_{ref} in water using the following equation [27]:

$$Z_{ref,\,pl} = Z_{ref}/C_{pl} \qquad (Z_{ref} \;\; in \;\; g/cm^2) \tag{3.3}$$

where C_{pl} is the scaling factor corresponding to the polystyrene material. The doses given to the films scanned with a VIDAR-XVR16 densitometer and analyzed with OMNIPRO software were of the order of 1-2 Gy. In this region, optical density was confirmed to be linear with absorbed dose, as reported by Gerbi et *al.* [29].

3.2.2 Monte Carlo simulation

Monte Carlo simulation model of the SL25 linear accelerator

The SL25 linear accelerator manufactured by Elekta has nine electron beams with nominal energies of 4, 6, 8, 10, 12, 15, 18, 20 and 22 MeV. It is equipped with a dual scattering foil system. The tantalum (Ta, Z=73) primary scattering foil, automatically positioned in the beam when the energy is selected, provides scatter of electrons in order to produce a broad beam profile which is then flattened by a low atomic number (Al, Z=13) secondary flattening foil. The latter scatters and attenuates the beam to a high degree of uniformity.

The SL25 linear accelerator is provided with four applicators to produce open field sizes of 6×6 cm^2, 10×10 cm^2, 14×14 cm^2 and 20×20 cm^2 at the isocenter (100 cm SAD). When an electron applicator is inserted into the linear accelerator head, upper and lower jaws are automatically opened to a field size preset by the manufacturer and these settings are energy and field size dependent. Each applicator is constructed with four apertures, the one closest to the patient being at 5 cm above the phantom surface. A Cerrobend cutout can be inserted into the lowest aperture in order to define a field size with irregular or asymmetric shape. We used the MC EGSnrc/ BEAMnrc [14] code, which is based on the EGSnrc [15] coupled photone-electron transport code developed at the NRC of Canada, to simulate electron beams from this linear accelerator. The accelerator head was broken into 11 component modules (CMs), which represent the exit window, primary scattering foil, primary collimator, secondary flattening foil, monitor chamber, mirror, upper and lower jaws, Mylar screen and applicator, as depicted in Fig. 3.2. The last scraper of the applicator was simulated with a BLOCK CM to enable the simulation of the cutout. The manufacturer provided detailed information about geometry, material composition and dimensions of each CM under a confidential agreement. The simulation was divided into two main steps. In the first step, the transport of the particles inside the accelerator head was simulated and a phase space file was created at the end of the CM "APPLICAT" (top of the CM "BLOCK", level A) since this part of linear accelerator head is identical for all insert cutouts for a given open applicator. This avoids repeated calculations and thus saves computing time. The second step was to use this phase space file as input for the simulation of the rest of the linear accelerator for all insert cutouts of interest, leading to the creation of a second phase space file at the end of the last "BLOCK" CM (level B). This second phase space file was used as input file to compute dose distribution in the water phantom and in the heterogeneous phantom by using the EGSnrc/DOSXYZnrc [30] MC code. This phase space created at the so-called "scoring plane", contains information about the position (X, Y, Z), direction (U, V, W), energy, type and origin (LATCH) of each particle

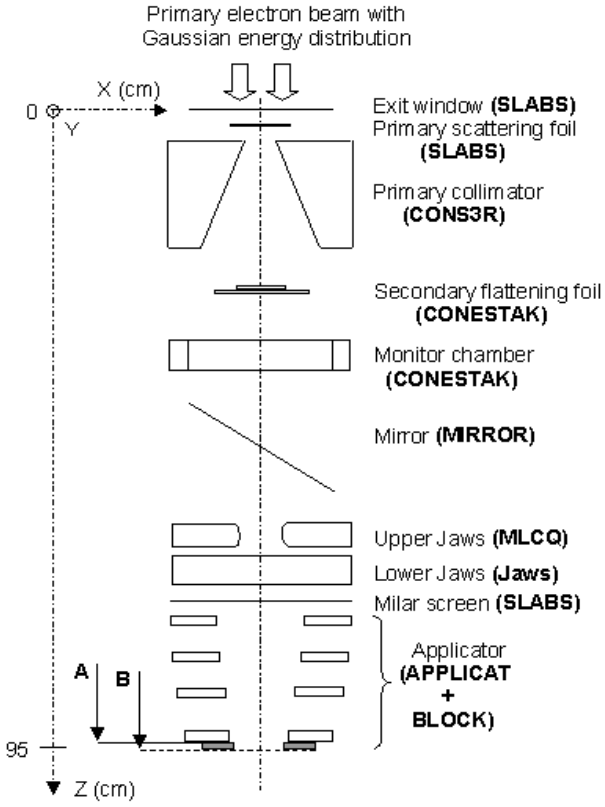

Figure 3.2. Schematic representation of the MC model for the SL25 linear accelerator as simulated with the BEAMnrc code. Indicated are the exit window, primary scattering foil, primary collimator, secondary flattening foil, monitor chamber, mirror, upper and lower jaws, Mylar screen and applicator. The BEAMnrc CMs that were used in the model are given between brackets.

crossing it. For both BEAMnrc and DOSXYZnrc, the transport parameters AP=PCUT=10 keV and AE=ECUT=521 keV were selected, AP and AE corresponding to the low-energy thresholds for production of secondary Bremsstrahlung photons and knock-on electrons, respectively, while PCUT and ECUT define the global cutoff energy for photon and electron transport, respectively. The boundary crossing algorithm (BCA) was set to PRESTA-I and spin effects were invoked. The fractional energy loss per electron-step,

ESTEPE, was controlled by the PRESTA-II electron-step transport algorithm and the electron range rejection was set to save computing time with a global cutoff energy of 1 MeV. Electron spectra having Gaussian energy distribution with sometimes smaller peaks at low energies were used for the simulation. This was necessary to "match" the measured and calculated depth dose. The beam spectra parameters that were used for the simulation are summarized in Table 1. The simulation was repeated by varying the mean energy and full width at half maximum (FWHM) of the spectra until the difference between measured and BEAMnrc calculated depth dose parameter R_{50} was less than 1 mm. The simulation was performed on a Mandrake Linux 10.1 operating system with g77 compiler installed on Pentium 4 with double processor Xeon 3.0 GHz, 1.0 GB RAM. As depicted in Fig. 3.2, the last CM ended at 95.0 cm from the reference plane set at the exit windows (Z=0). Particles from the second phase space file generated by the BEAMnrc code in the second step were thus first simulated in the 5 cm slabs air before striking the phantom surface. The water phantom was simulated using DOSXYZnrc, an EGSnrc user code for 3D absorbed dose calculations in Cartesian coordinates. Its dimensions were 40×40×40 cm^3 with its front surface at the isocenter (100 cm SAD). Voxel sizes were defined in many ways depending on energy, field size and whether depth dose calculations or off-axis profiles were concerned. A typical voxel size of 0.25×0.25×0.1 cm^3 was selected in the depth dose calculation for 6×6 cm^2 field size for 4 MeV calculations, whereas 0.5×0.5×0.2 cm^3 voxel sizes were selected for 10×10 cm^2 and 20×20 cm^2 field sizes for 12 and 18 MeV electron beam calculations. About (3-6)×10^8 particle histories were simulated both in the BEAMnrc and DOSXYZnrc, depending on the energy and field size to keep a statistical uncertainty less than 1% for all calculations (depth dose as well as off-axis profile). About (3-400)×10^6 particles (photons and electrons) were stored in the constructed phase space files. We set the DOSXYZnrc parameter NRCYCL=0 (NRCYCL parameter determines the number of times that each particle from a phase space source is recycled) allowing BEAMnrc to automatically calculate the NRCYCL value based on

the number of histories and the total number of particles in each phase space file. However, while BEAMnrc automatically assigned this value, in some calculations, the simulations involved recycling of the phase space file, but no more than once. This is unlikely to affect uncertainties in the dose calculations. For both BEAMnrc and DOSXYZnrc codes, the CPU times per history was dependent on energy, field size as well as parameters of simulation.

3.2.3 Oncentra MasterPlan dose calculation

The Radiotherapy Department of Saint-Luc Hospital (Brussels, Belgium) recently bought a license of the new version of the "MasterPlan version 1.4, Service Pack 4" treatment planning system for two energies, 4 and 12 MeV. OMTPS is a radiotherapy treatment planning system developed by

Table 3.1. Energy spectrum parameters of electron beams used for the simulation. FWHM=full width at half maximum. Parameters of smaller peaks sometimes introduced in the spectrum are omitted here.

Nominal energy (MeV)	Peak energy (MeV)	FWHM (MeV)
4	5.05	1.45
12	12.70	2.63
18	18.38	2.90

Nucletron for planning patient treatments with either photon or electron beams. The dose planning is performed on a 3D density matrix constructed in OMTPS from patients CT-scans. The Hounsfield number assigned to each standard tissue is mapped from the precalculated electron density using relations given by Knöös et *al.* [31], but the user can also request that the entire patient be represented by pure water. The used formalism in OMTPS is general enough in order to handle various clinical beam geometries. Thanks to the use of models, absolute dose per Monitor Units (MU) or treatment times can be calculated by the OMTPS for all fields relative to the dose in

the calibration field and point. The use of OMTPS starts with the characterization of the treatment unit. The characterization procedure is divided into four main steps, particularly for the electron beam

Accelerator design
The user has to provide geometrical details of all CMs of the accelerator head such as exit window, primary scattering foil, primary collimator, secondary flattening foil, monitor chamber, mirror, upper and lower jaws, Mylar screen and applicators. For each CM, information concerning thickness, size, position, shape and material composition is furthermore required.

Air fluence profiles
Air fluence measurements are carried out free in air (along the central axis in the inplane and crossplane directions at two SSDs) without having an electron applicator mounted on the linear accelerator.

Depth doses and off-axis profiles in water
For each energy, an open field depth dose measurement at 100 cm SSD, normalized to 100.0% at a depth defined by Nucletron is required. The normalization depth depends on the beam energy. Further measurements (with the applicator in position) of depth doses and off-axis profiles for each energy and applicator are required by the manufacturer.

Absolute dose measurements
As the system calculates the absolute dose to the medium, a direct representation of the dose in terms of MU for a given applicator in a specific electron beam requires an absolute dose measurement for a fixed number of MU for each applicator and energy. The recommended depth and SSD are chosen according to the nationally recommended dosimetry protocol used [27].
These data are collected by Nucletron (files in a specified format for processing) which performs the characterization of the radiation treatment unit.

In this process, beams are "tuned" by the manufacturer and the user is provided with a ready-to-use virtual treatment unit. Calculations in the OMTPS were performed with the maximum number of particles/cm^2 available for each energy (10^6 particles/cm^2).

3.3 Results

3.3.1 Homogeneous water phantom calculations

Central axis depth dose and off-axis profiles

We have validated our BEAMnrc MC models by comparing depth dose and off-axis profile between BEAMnrc and measurements performed in a homogeneous water phantom. The accuracy of OMTPS calculation in the water phantom has been investigated by similar comparisons. Fig. 3.3 shows the comparison of depth dose profiles for three energies (4, 12 and 18 MeV) for open field sizes of 6×6 cm^2, 10×10 cm^2 and 20×20 cm^2. Agreement of R_{50}, i.e., the difference between calculations and measurements, between OMTPS and measurements was better than 1 mm. Similar results were obtained for open applicators with various cutouts, results not presented here. However, the comparison demonstrates serious limitations of OMTPS to match depth dose curve in the build-up region and beyond R_{50} in the case of a 4 MeV electron beam, with a maximum discrepancy of about 2 mm beyond R_{50} and the projected practical range values, R_p, predicted from OMTPS calculation are overestimated by about 1.9 mm. Off-axis profiles in the inplane and crossplane directions at the depth of maximum dose (see Fig. 3.4) and the depth of R_{50} (results not presented here) were also calculated from BEAMnrc, OMTPS and compared to measurements. The overall agreement between BEAMnrc and measurements on the one hand and between OMTPS and measurements on the other hand was better than 1%/1 mm in the low-dose/high-dose gradient regions. Table 3.2 summarizes these results for a depth dose profile comparison of the R_{50} parameter. Similar calculations were also performed for three applicators (6×6, 10×10 and 20×20

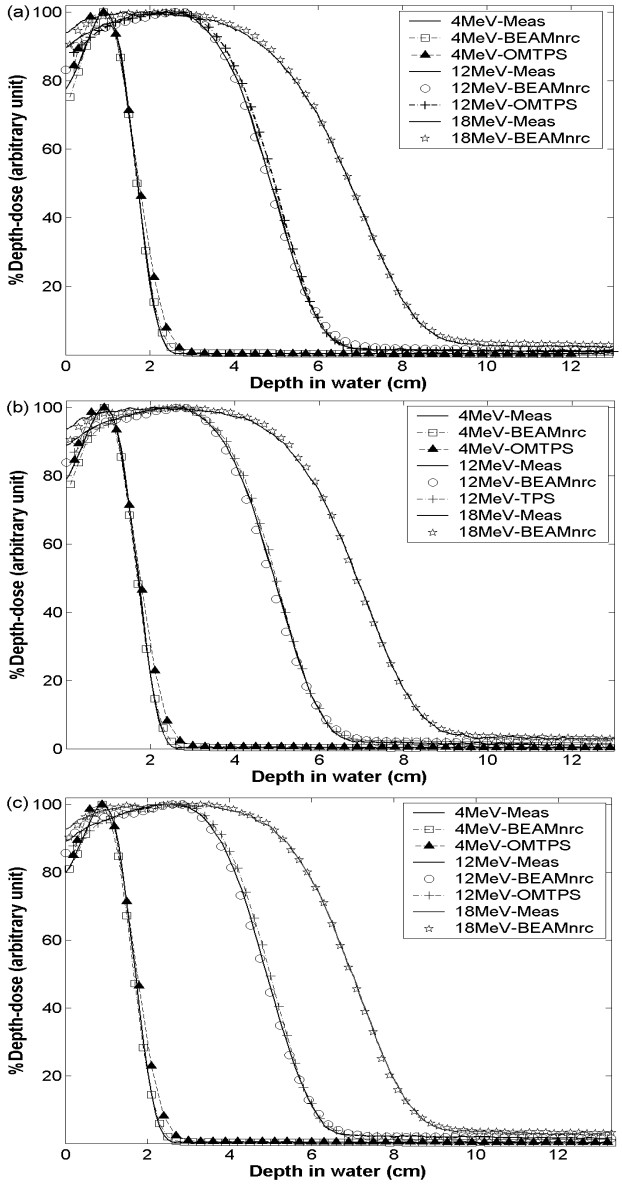

Figure 3.3. Central axis depth dose curves for 6×6 cm^2 (a), 10×10 cm^2 (b) and 20×20 cm^2 (c) field size for 4, 12 and 18 MeV at 100 cm SSD. Comparison between measurements (Meas) and treatment planning system (OMTPS) calculations (4 and 12 MeV) on the one hand and between Meas and BEAMnrc calculations (4, 12 and 18 MeV) on the other hand. Dose normalization is performed at the depth of maximum dose along the central axis. Agreement (difference between calculations and measurements) of R_{50} between each other was better than 1 mm.

cm^2) with many cutout combinations. Results, though not presented here, were found to be in good agreement (differences less than 1%/1 mm in the low dose/high-dose gradient regions) with measurements both in the inplane and crossplane directions.

Output factor comparison

In addition to the comparison of relative dose distributions, we have performed output factors comparison between measurements and the values predicted from BEAMnrc and OMTPS computations. Table 3 summarizes results obtained for 4, 12 and 18 MeV where both OMTPS and BEAMnrc calculations are compared to measurements. In most cases, differences between BEAMnrc predictions and measurements were around 1.0%, especially for 12 MeV energy. Despite the fact that for the 4 MeV beam we obtained a very good fit between measured and calculated relative dose distributions for 3×3 and 5×2.5 cm^2 cutouts within 6×6 cm^2 applicator, the predicted output factors from BEAMnrc simulations remained significantly lower than the measured ones, although we have tried to model these inserts as accurately as possible. Similar discrepancies were observed for OMTPS, with overall disagreements somewhat worse than for BEAMnrc. The results are summarized in table 3.2, where differences larger than ±2% are made bold in columns four and five for OMTPS and BEAMnrc, respectively. The OMTPS voxel size (in terms of the length of the voxel side in each direction) internally set by the dose calculation algorithm was 0.5 cm. The above deviations could be possibly ascribed to the combined facts that (1) output factor measurements are well known to be prone to errors for small field size measurements, due to the nonflatness of lateral dose profiles. Any mismatch (1 mm) between the measured dose point and the calculated voxel can lead to large deviations in the region around the depth of maximum dose. A more accurate measurement of output factors should be done with a small enough dosimeter so that the nonflatness of the dose profile has a little effect on the dose integration. Furthermore, percentage depth dose for small field sizes exhibits a narrow peak around the depth of maximum dose; thus, small er-

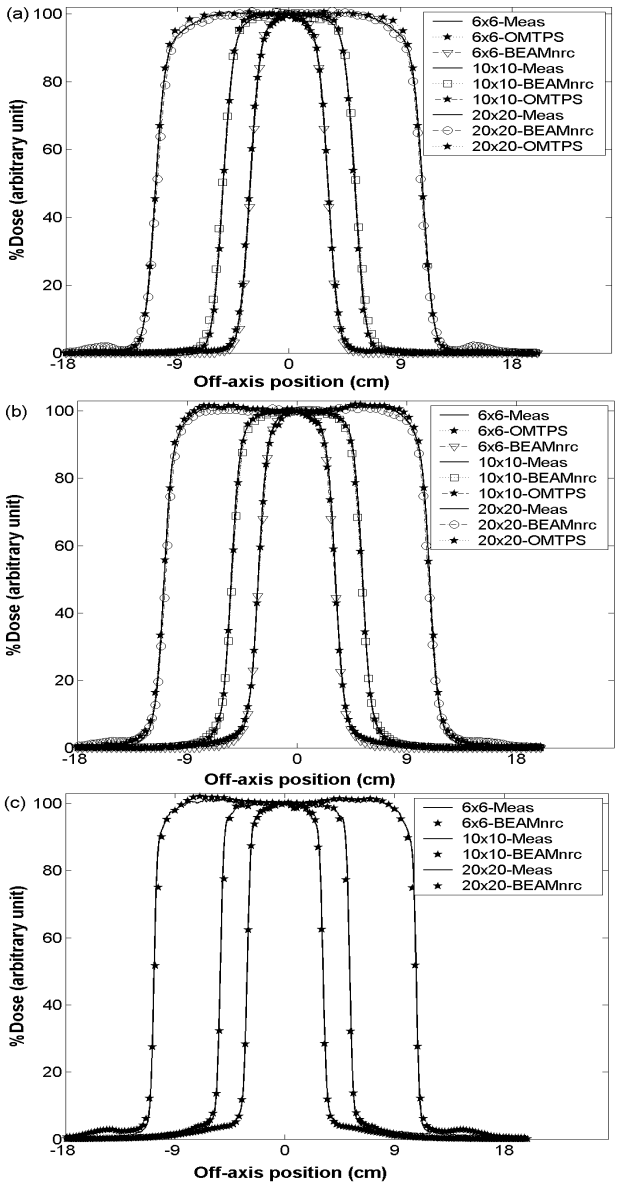

Figure 3.4. Off-axis profiles (inplane direction, normalized at the central axis dose) for three open field sizes 6×6 cm^2, 10×10 cm^2 and 20×20 cm^2 at 100 cm SSD. Comparison between measurements (Meas), BEAMnrc simulation and treatment planning system (OMTPS) for 4 MeV electron beam energy (a), 12 MeV electron beam energy (b) and 18 MeV electron beam energy (c). The depth of comparison in the water phantom is the depth of maximum dose along the central axis and data were normalized at this depth.

rors in detector positioning can lead to large deviations of the measured dose at the depth of maximum dose, (2) electron output factor can be broken into two dose components [9-11]; direct particles whose contribution to the dose at the depth of maximum dose, d_{max}, is predominant and scattered particles from which contribution to the dose at d_{max} may be significantly reduced for the smallest insert cutouts size, because the insert blocks particles from the applicator scrapers. These two components behave differently. The scattered component of the electron beam is strongly dependent of the shape of the insert as pointed out by Turian et *al.* [11], which make it difficult to predict electron output factors. Therefore, small inaccuracy to match the simulated cutout with the experimental one is likely to introduce dosimetry errors between calculated and measured data, (3) finally, the relatively large voxel size (the length of the voxel side in each direction was 0.5 cm) automatically set by OMTPS during the calculation can also lead to deviations when predicting output factors. Ideally the dimension of the detector as well as the scoring voxels in the MC simulations that are used to perform output factors should closely match the voxel size in the OMTPS.

Table 3.2. Comparison of measured (Meas) and calculated R_{50} values. Diff.1=(Meas-BEAMnrc) and Diff.2=(Meas-OMTPS). Agreement with measurements was found to be less than 1 mm for both OMTPS and BEAMnrc calculations.

Field size	**4 MeV/R_{50} (cm)**			**12 MeV/R_{50} (cm)**			**18 MeV/R_{50} (cm)**	
(cm^2)	Meas	Diff.1	Diff.2	Meas	Diff.1	Diff.2	Meas	Diff.1
6×6	1.71	-0.03	-0.05	4.88	-0.03	-0.08	6.77	0.01
10×10	1.71	0.02	-0.07	4.94	0.07	-0.07	6.89	0.04
20×20	1.71	-0.01	0.05	4.90	0.02	-0.09	7.00	0.08

3.3.2 Heterogeneous thorax phantom calculations

The accuracy of the OMTPS calculation in the presence of heterogeneities has been investigated by comparison with calculations of off-axis profile (in-plane direction) in the cork material (thorax phantom depicted in Fig. 1)

simulating lung tissue at various depths spaced by 1 cm and 0.5 cm for 12 and 4 MeV electron beam calculations, respectively. The thorax phantom was scanned and CT-scan data were introduced in DOSXYZnrc using CTCREATE. In the heterogeneous phantom calculations, distances were referred from the lung surface: 1 cm from the lung surface was thus equivalent to 3.3 cm (because of 2.3 cm of adipose tissue equivalent material on top of the lung surface) from the top of the phantom surface for 12 MeV calculations. Due to the shorter range of lower energy electrons, calculations were performed in the thorax phantom without the first 1.1 cm layer of polyethylene material in the case of the 4 MeV electron beam irradiation. Therefore, 1 cm from the lung surface was equivalent to 2.2 cm from the top of the phantom surface. The 4 MeV electron beam is obviously not of clinical interest for chest wall irradiation but this energy was chosen to evaluate the accuracy of OMTPS calculation for low electron beams irradiation. Fig. 3.5 shows a comparison between BEAMnrc, OMTPS and measurements for 12 MeV electron beam calculations (field size 6×6 cm^2). As expected, overall agreement between BEAMnrc and measurements was better than between OMTPS and measurements. Both algorithms, full BEAMnrc MC simulation as well as OMTPS, slightly underestimated the dose between two ribs and overestimated it below the ribs. This is consistent with published data from Cygler et *al.* [23]. Depending on the field size and the measurement depth, differences between BEAMnrc and measurements were less than 1% (0.5-0.8% between two ribs) and ≈0.6% below the ribs, whereas differences between OMTPS and measurements were up to 4% (2.4% between two ribs and 2.0-4.0% below the ribs). The agreement between OMTPS and measurements was much better far from the heterogeneities, where the effect of ribs perturbations becomes less pronounced or disappeared [23, 24, 28, 32]. This can be seen in Fig. 5, case (c) where at 3 cm from the lung surface for a 12 MeV beam, ribs are no longer seen and a good agreement was observed. This is also valid for other field sizes that are not presented here. As in the case of 12 MeV beam energy, Fig. 3.6 shows a comparison between BEAMnrc, OMTPS and measurements for a 4 MeV electron beam (field

size 6×6 cm^2). The depths of comparison were 0.5, 1.0 and 1.5 cm from the lung surface. For both OMTPS and BEAMnrc calculations agreement was worse for 4 MeV than for 12 MeV beam. Deviations (depending on the field size and the depth of measurements) ranged between two ribs from 0.8 to 2.0% for BEAMnrc calculations and 0.5-4.0% for OMTPS calculations, whereas below the ribs, they were ≈1.0% for BEAMnrc and ranged from 0.5 to 4.0% for OMTPS calculations. Away from the penumbra region in the case of 12 MeV electron beam irradiation, large discrepancies between BEAMnrc as well as OMTPS with measurements were observed; this might come from the energy response of the KODAK EDR2 films irradiated at 200/300 MU for 12/4 MeV calculations in that region. The film's response is not constant with energy and it is known to be oversensitive at low photon/electron energies. The sensitivity of the film, therefore, increases with increasing scatter-to-primary ratio, which is the case outside the penumbra region. The dependence of optical density of KODAK EDR2 films (irradiated with electron beams) with dose and energy as reported by Gerbi et *al.* [29] may thus yield to dosimetric errors away from the penumbra region.

Table 3.3. Comparison between measured (Meas) and calculated output factors for 4, 12 and 18 MeV electron beams. Diff.1=[(Meas-OMTPS)/Meas], and Diff.2=[(Meas-BEAMnrc)/Meas].

Applicator	**Insert**	**4 MeV**			**12 MeV**			**18 MeV**	
(cm^2)	(cm^2)	Meas	Diff.1 (%)	Diff.2 (%)	Meas	Diff.1 (%)	Diff.2 (%)	Meas	Diff.2 (%)
6×6	3×3	0.730	**-2.74**	**2.88**	0.911	**-2.96**	0.88	0.976	1.32
	5×2.5	0.725	**-2.62**	**2.07**	0.921	-1.30	1.74	0.951	1.28
10×10	3×3	0.897	**-2.56**	0.00	0.914	**-2.52**	0.00	0.955	0.20
	5×2.5	0.904	-1.66	0.95	0.924	-1.41	0.11	0.956	0.00
	6×6	1.003	-0.50	-0.3	0.983	-0.71	-0.61	0.983	0.20
20×20	6×6	1.036	0.40	-0.97	0.974	0.62	0.92	0.971	-1.03
	6×16	1.040	-1.57	0.72	0.976	**2.15**	0.10	0.970	-1.03
	10×16	1.040	**-2.90**	-0.95	0.979	-1.12	0.31	0.967	-0.30
	10×10	1.046	0.76	-0.97	0.977	-0.51	-0.72	0.971	-1.34
	14×14	1.055	0.86	0.19	0.976	-0.20	-0.62	0.962	-1.56

3.4 Discussion

The accuracy of OMTPS has been investigated for two energies 4 and 12 MeV both in the homogeneous water phantom and heterogeneous phantom. We compared measured dose distributions with those calculated by OMTPS and full MC simulation, respectively. We showed that OMTPS was able to predict dose distribution accurately for 12 MeV calculations in the homogeneous phantom as well as in the heterogeneous phantom. However, large discrepancies between measurements and OMTPS prediction of percentage depth dose at lower energy (4 MeV) were found for all field sizes investigated. This might partially be due to systematic uncertainty associated with relatively large voxel size (parameter for which the user has no control) automatically set by OMTPS during computation (especially when the phantom size is too large). The accuracy of OMTPS seem thus to be more sensitive to voxel size at lower energy than higher energy. This trend was also observed when performing calculations in the heterogeneous phantom. The highest deviations found for the energies investigated corresponded to 4 MeV energy calculations. This suggests that one has to be more careful when performing calculations with OMTPS at very low energies and demonstrates the need to perform a full MC simulation in this case. The calculations performed in water as well as in the heterogeneous phantom demonstrated that the EGSnrc/BEAMnrc MC code is more robust in predicting dose distribution accurately under the tested conditions.

The previous study by Cygler et *al.* [23] was only based on measurements, whereas Ding et *al.* [24] performed a direct comparison of a VMC++ algorithm with a Pencil beam algorithm. The above authors (Cygler et *al.* [23] and Ding et *al.* [24]) used the same heterogeneous phantoms and some of their measurements were performed closer to the heterogeneities. Moreover, off-axis profiles were determined in the solid water phantom instead of a low-density lung equivalent material in both of these previous studies. Unlike the latter reports, our studies focused on both very low (4 MeV) and high (12 MeV) electron beam energies, high density material inhomogeneity (Teflon rib) and measurements comparably deeper in the phantom, which explains

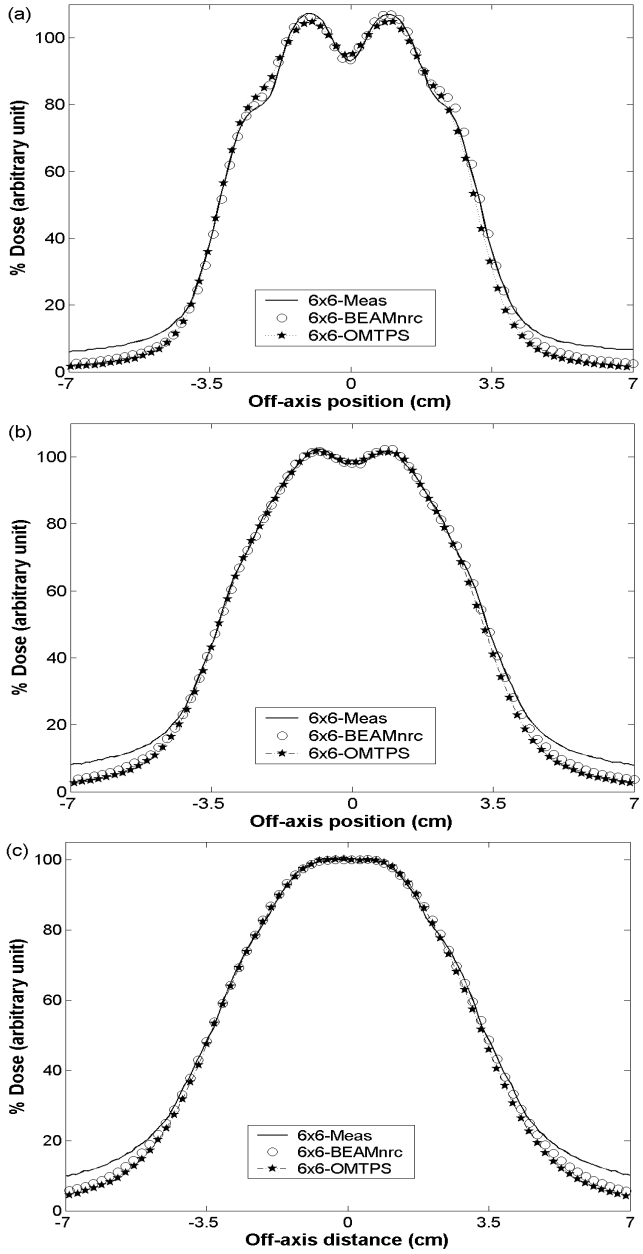

Figure 3.5. Off-axis profiles (inplane direction) for an open field size of 6×6 cm^2 at 100 cm SSD. Comparison between measurements (Meas), BEAMnrc simulation and treatment planning system (OMTPS) for 12 MeV electron beam. Depth from the lung surface: 1 cm (a), 2 cm (b) and 3 cm (c).

why our calculation results were not the same. Although the framework of our investigations was not the same as that of the above mentioned authors, the VMC++ algorithm implemented in the OMTPS underestimated the dose between two ribs and overestimated it beneath the ribs in all studies.

3.5 Conclusions

In the present work, we developed BEAMnrc MC models for an Elekta SL25 linear accelerator for 4, 12 and 18 MeV electron beam energies. In addition to comparing normalized dose distributions between measurements and those calculated by with BEAMnrc and OMTPS calculations, absolute dose has been validated by comparison of measured output factors and those predicted from BEAMnrc and OMTPS computations. The overall agreement was usually within 1.0% for BEAMnrc calculations. We have demonstrated that accurate (agreement less than 1%/1 mm in the low-dose/high-dose gradient regions) dose distributions in water could be calculated from these models. From results obtained with BEAMnrc calculations (discrepancies less or equal to 2.0% between two ribs and around 1.0% below the ribs) in the heterogeneous phantom, we conclude that our BEAMnrc MC models are able to predict dose perturbations caused by rib heterogeneities. The evaluation of the accuracy of OMTPS has been investigated in two main steps. Firstly, we compared dose distributions between measurements and OMTPS calculations in the water phantom and we validated OMTPS absolute dose calculations by comparing output factors with measurements. Dose distributions predicted from OMTPS calculations were found to be in good agreement with measurements (discrepancies around 1.0% or smaller than 2 mm in the low-dose/high-dose gradient regions, respectively) whereas for output factors, discrepancies up to nearly 3% were observed between measurements and OMTPS predictions. Secondly, off-axis profiles were measured in the heterogeneous phantom containing bone structures and compared to OMTPS calculations. Agreement was found to be in the range of 0.5-4.0% between two ribs as well as beneath the ribs with highest dis-

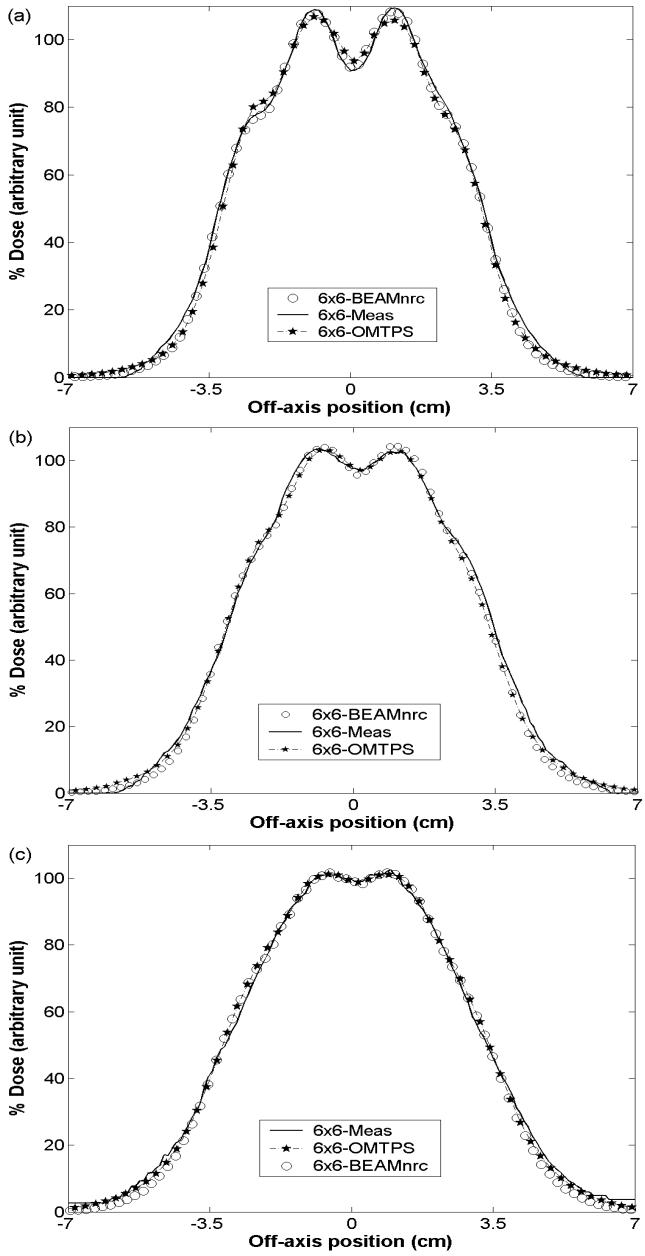

Figure 3.6. Off-axis profiles (inplane direction) for an open field size of 6×6 cm^2 at 100 cm SSD. Comparison between measurements (Meas), BEAMnrc simulation and treatment planning system (OMTPS) for 4 MeV electron beam. Depth from the lung surface: 0.5 cm (a), 1 cm (b) and 1.5 cm (c).

crepancies occurring at lower energy calculations (4 MeV). As expected, the agreement between OMTPS and measurements was much better in areas far from heterogeneities, where the effect of rib perturbations disappeared. The tolerances for electron beam dose calculations suggested by NCS [7] working group were 2%/2 mm and 3%/3 mm, for small dose gradient/large dose gradient in the homogeneous phantom and heterogeneous phantom, respectively. In view of our results, the deviations observed were within these criteria of acceptability and even much better for BEAMnrc MC simulation and in most cases for OMTPS calculations, demonstrating the reliability of using this version 1.4 of OMTPS in comparison with Pencil Beam Algorithms for planning treatment of cancer patients with electron beams [24]. However, significant deviations found in the case of 4 MeV electron beam calculations demonstrated the need to perform a detailed MC simulation when using OMTPS at lower energy, especially when the patient's anatomy based on the CT-scan images is too large and/or when calculations are performed in the high dose gradient regions.

Acknowledgments

This work was partly supported by the ICTP through CEPAMOQ (OEA-project-71) at the University of Douala (Cameroon) and the Fellowships Program of the "Agence Universitaire de la Francophonie (AUF)". We would like to thank the Elekta group, Dr. Janet Rickard in particular, for supplying the information that allowed us to program the SL25 linear accelerator of the Cliniques Universitaires Saint-Luc. The authors are greatly indebted to the radiation oncology physicists M. Tomsej and J. M. Denis of the Radiotherapy Department of Cliniques Universitaires Saint-Luc (Brussels, Belgium) for their help in measurements performed in the water phantom and they thank Dr. C. Craddock-de Burbure for revising the manuscript.

3.6 Bibliography

[**1**] Shiu AS, Hogstrom KR. Pencil-beam redefinition algorithm for electron dose distributions. Med Phys 1991;18:7-18.

[**2**] Cygler J, Battista JJ, Scrimger JW, Mah E, Antolak J. Electron dose distributions in experimental phantoms: a comparison with 2D pencil beam calculations. Phys Med Biol 1987;32:1073-86.

[**3**] Mah E, Antolak J, Scrimger JW, Battista JJ. Experimental evaluation of 2D and 3D electron pencil beam algorithm. Phys Med Biol 1989;34:1174-94.

[**4**] Hogstrom KR, Mills MD, Almond PR. Electron beam dose calculations. Phys Med Biol 1981;26:445-59.

[**5**] Hogstrom KR, Mills MD, Meyer JA, Palta JR, Mellenberg DE, Meoz RT, et al. Dosimetric evaluation of a pencil-beam algorithm for electrons employing a twodimensional heterogeneity correction. Int J Radiat Oncol Biol Phys 1984;10:561-9.

[**6**] Ostwald PM, Metcalfe PE, Denham JW, Hamilton CS. A comparison of three electron planning algorithms for a 16 MeV electron beam. Int J Radiat Oncol Biol Phys 1994;28:731-40.

[**7**] Bruinvis IAD, Keus RB, Lenglet WJM, Meijer GJ, Mijnheer BJ, van't Veld AA, et al. Quality assurance of 3-D treatment planning systems for external photon and electron beams: practical guidelines for acceptance testing, commissioning and periodic quality control of radiation therapy treatment planning systems. NCS Report 2006;15.

[**8**] Ma CM, Faddegon BA, Rogers DWO, Mackie TR. Accurate characterization of Monte Carlo calculated electron beams for radiotherapy. Med Phys 1997;24:401-16.

[**9**] Zhang GG, Rogers DWO, Cygler JE, Mackie TR. Monte Carlo investigation of electron beam output factors versus size of square cutout. Med Phys 1999;26:743-50.

[**10**] Kapur A, Ma CM, Mok EC, David OF, Arthur LB. Monte Carlo cal-

culations of electron beam output factors for a medical linear accelerator. Phys Med Biol 1998;43:3479-94.

[**11**] Turian JV, Smith BD, Bernard DA, Griem KL, Chu JC. Monte Carlo calculations of output factors for clinically shaped electron fields. J Appl Clin Med Phys 2004;5:42-62.

[**12**] Pavon EC, Sanchez-Doblado F, Leal A, Capote R, Lagares JI, Perucha M, et al. Total skin electron therapy treatment verification: Monte Carlo simulation and beam characteristics of large non-standard electron fields. Phys Med Biol 2003;48:2783-96.

[**13**] Popescu IA, Shaw CP, Zavgorodni SF, Beckham WA. Absolute dose calculations for Monte Carlo simulations of radiotherapy beams. Phys Med Biol 2005;50:3375-92.

[**14**] Rogers DWO, Faddegon BA, Ding GX, Ma CM, We J, Mackie TR. BEAM: a Monte Carlo code to simulate radiotherapy treatment units. Med Phys 1995;22:503-24.

[**15**] Kawrakow I. Accurate condensed history Monte Carlo simulation of electron transport. I. EGSnrc, the new EGS4 version. Med Phys 2000;27:485-98.

[**16**] Kawrakow I, Fippel M. VMC++, a fast MC algorithm for radiation treatment planning. In: XIII international conference on the use of computers in radiation therapy. Heidelberg, Germany: Springer-Verlag; 2000. p. 126-8.

[**17**] Kawrakow I. VMC++, electron and photon Monte Carlo calculations optimised for radiation treatment planning. In: Kling LA, Barao F, Nakagawa M, Tavora L, Vaz P, editors. Advanced Monte Carlo for radiation physics, particle transport simulation and applications: proceeding of the Monte Carlo 2000 meeting. Berlin: Springer; 2001. p. 229-36.

[**18**] Kawrakow I, Fippel M. Investigation of variance reduction techniques for Monte Carlo photon dose calculation using XVMC. Phys Med Biol 2000;45: 2163-83.

[**19**] Fippel M, Kawrakow I, Friedrich K. Electron beam dose calculations with the VMC algorithm and the verification data of the NCI working group. Phys Med Biol 1997;42:501-20.

[**20**] Fippel M. Fast Monte Carlo dose calculation for photon beams based on the VMC electron algorithm. Med Phys 1999;26:1466-75.

[**21**] Ma CM, Li JS, Pawlicki T, Jiang SB, Deng J, Lee MC, et al. A Monte Carlo dose calculation tool for radiotherapy treatment planning. Phys Med Biol 2000;47:1671-89.

[**22**] Doucet RM, Olivares M, DeBlois F, Podgorsak EB, Kawrakow I, Seuntjens J. Comparison of measured and Monte Carlo calculated dose distributions in inhomogeneous phantoms in clinical electron beams. Phys Med Biol 2003;48:2339-54.

[**23**] Cygler JE, Daskalov GM, Chan GH, Ding GX. Evaluation of the first commercial Monte Carlo dose calculation engine for electron beam treatment planning. Med Phys 2004;31:142-53.

[**24**] Ding GX, Cygler JE, Yu WC, Kalach Nina I, Daskalov G. A comparison of electron beam dose calculation accuracy between treatment planning systems using either a pencil beam or a Monte Carlo algorithm. Int J Radiat Oncol Biol Phys 2005;63:622-33.

[**25**] Popple AR, Weinberg R, Antolak AJ, Sung-Joon Y, Prem NP, Duan J, et al. Comprehensive evaluation of a commercial macro Monte Carlo electron dose calculation implementation using a standard verification data set. Med Phys 2006;33:1540-51.

[**26**] Ding GX, Duggan MD, Coffey WC, Parvaneh S, Cygler JE. First macro Monte Carlo based commercial dose calculation module for electron beam treatment planning - new issues for clinical consideration. Phys Med Biol 2006;51:2781-99.

[**27**] Andreo P, Burns DT, Hohlfeld K, Huq MS, Kanai T, Laitano F, et al. Absorbed dose determination in external beam radiotherapy: an International Code of Practice for dosimetry based on standards of absorbed dose

to water. IAEA TRS 2000;398.

[**28**] Seutjens J, Van der Plaetsen A, Thierens H, Piessens M. Comparison of measured and calculated dose distributions in lung after electron beam treatment of the chest wall. Med Phys 1994;21:1959-68.

[**29**] Gerbi JB, Dimitroyannis DA. The response of Kodak EDR2 film in high-energy electron beams. Med Phys 2003;30:2703-5.

[**30**] Walters BRB, Rogers DWO. DOSXYZnrc user manuel. Ottawa: National Research Council of Canada; 2004. NRCC Report No. PIRS-794 rev A.

[**31**] Kn*öö*s T, Nilsson M, Ahlgren L. A method for conversion of Hounsfield number to electron density and prediction of macroscopic pair production cross-sections. Radiother Oncol 1986;5:337-45.

[**32**] Ding GX, Cygler JE, Yu MK. Evaluation of a commercial threedimensional electron beam treatment planning system. Med Phys 1999;26: 2571-80.

Chapter 4

Publication 2: Validation of XiO eMC-based TPS

Physica Medica (2012)

ORIGINAL PAPER

Validation of XiO Electron Monte Carlo-based calculations by measurements in a homogeneous phantom and by EGSnrc calculations in a heterogeneous phantom

P. Edimo[a, b], M.G. Kwato[b], S. Vynckier[a]

[a]Radiotherapy Department, Université catholique de Louvain, Cliniques Universitaires Saint-Luc, Avenue Hippocrate 10, B-1200 Brussels, Belgium
[b]University of Douala, Centre for Atomic Molecular Physics and Quantum Optics, P.O. Box 8580 Douala, Cameroon

Thesis submitted in fulfillment of the requirements for the degree of "Docteur en Sciences Médicales - Orientation : Physique Médicale" - september 11, 2012.

Received 25 Febuary 2012; received in revised form 3 August 2012; accepted 11 August 2012

Abstract

The purpose of the present study is to perform a clinical validation of a new commercial Monte Carlo (MC) based treatment planning system (TPS) for electron beams, i.e. the XiO 4.60 electron MC (XiO eMC). Firstly, MC models for electron beams (4, 8, 12 and 18 MeV) have been simulated using BEAMnrc user code and validated by measurements in a homogeneous water phantom. Secondly, these BEAMnrc models have been set as the reference tool to evaluate the ability of XiO eMC to reproduce dose perturbations in the heterogeneous phantom. In the homogeneous phantom calculations, differences between MC computations (BEAMnrc, XiO eMC) and measurements are less than 2% in the homogeneous dose regions and less than 1 mm shifting in the high dose gradient regions. As for the heterogeneous phantom, the accuracy of XiO eMC has been benchmarked with predicted BEAMnrc models. In the lung tissue, the overall agreement between the two schemes lies under 2.5% for the most tested dose distributions at 8, 12 and 18 MeV and is better than the 4 MeV one. In the non-lung tissue, a good agreement has been found between BEAMnrc simulation and XiO eMC computation for 8, 12 and 18 MeV. Results are worse in the case of 4 MeV calculations (discrepancies $\approx$ 4%). XiO eMC can predict dose perturbation induced by high-density heterogeneities for 8, 12 and 18 MeV. However, significant deviations found in the case of 4 MeV demonstrate that caution is necessary in using XiO eMC at lower electron energies.

KEYWORDS: Treatment planning; Electron beams dosimetry; Heterogeneous phantom; XiO Electron Monte Carlo.

4.1 Introduction

In the patient radiotherapy treatment process, accurate dose calculation is one of the important steps between the dose prescription to the clinical target volume and the actual dose delivery. Ensuring treatment quality in radiation therapy requires that the best equipment and techniques should be available for treatment planning. This includes the actual purchase and clinical implementation of a treatment planning system (TPS) which is able to compute absorbed dose distributions with an acceptable accuracy, especially if tissue heterogeneities are present. Monte Carlo (MC) methods have proven to be among the best tools for computing radiotherapy dose [1-4]. One of the important developments in the MC technique was the release of the BEAMnrc [5], an EGSnrc-based [6] radiotherapy simulation package. As the MC method is by its nature very time consuming and impractical for radiotherapy applications, a number of approximations and simplifications to speed up calculations have been included in the commercial MC dose calculation engines, leading to the development of fast MC algorithms [7-12] implemented in some TPS for patients dose computation. Traditionally, the clinical implementation of every MC based TPS involves design compromises with possible errors. Therefore, it is important to perform independent validation under conditions similar to those found in clinic [13-15]. Recently, our radiotherapy department of the University Hospital Saint-Luc, bought a license of a new MC based TPS for four electron beam energies 4, 8, 12 and 18 MeV. The above TPS, XiO 4.60 electron MC (XiO eMC) is developed and commercialized by ELEKTA CMS SOFTWARE group (ECMSSG). In the present study, we followed the commissioning approach already presented in our previous work [15]. As this TPS was not yet studied for ELEKTA SL25 linear accelerators, we have been careful in configuring XiO eMC. In addition to dosimetric data for beam characterization (percentage depth dose, off-axis profiles and output factors), as specified in the user manual, the accuracy of XiO eMC model for a given linear accelerator type depends on other manufacturer specifications, e.g. the opening jaws for each field size, the applicator designs, applicator material and serial numbers.

4.2 Materials and methods

4.2.1 Measurements

Homogeneous water phantom measurements

Dose distributions in the water thank (40×40×40 cm^3) for electron beam of 4, 8, 12 and 18 MeV delivered by an ELEKTA SL25 medical linear accelerator have been measured within an IBA computerized water phantom system and analyzed with OmniPro-Accept, version 6.6B software. Measurements have been carried out for open field sizes of 6×6 cm^2, 10×10 cm^2, 14×14 cm^2, 20×20 cm^2 and the 5×5 cm^2 insert within the 14×14 cm^2 open applicators, at two SSDs of 100 and 115 cm. Percentage depth dose and off-axis profiles have been measured with a Wellhöfer type CC01 thimble ionization chamber having 0.01 cm^3 collecting volume. Depth ionization curves have been converted to the percentage depth dose by multiplying the ionization charge at each measurement depth by the corresponding water/air stopping-power ratios derived from the IAEA, TRS 398 protocol [16]. Output factors have been measured for open field size of 6×6 cm^2, 10×10 cm^2, 14×14 cm^2 and 20×20 cm^2 open applicators and several highly asymmetric insert cutouts. Measurements have been performed at the individual depth, R_{100}, of each field based on its PDD, with two ionization chambers: a Plane-parallel ionization chamber type NACP17-02, active volume 0.16 cm^3 for large field sizes measurements and a Scanditronix-Wellhöfer IC13 thimble ionization chamber, having a cavity volume of 0.13 cm^3, for measurements in small field sizes. All cross-beam profiles have been measured at several depths, namely, R_{100}, R_{90}, R_{80}, R_{50}, R_{20} and at 2 cm away from the practical range (Rp + 2 cm), where R_J is the depth, beyond the depth of maximum dose R_{100}, at which the dose at the central axis falls off by J% of the maximum dose. In this work, output factors (OF) are defined as:

$$OF = \frac{D_{max}(E, S, SSD)}{D_{max}(E, 10 \times 10\ cm^2, SSD)} \tag{4.1}$$

where D_{max}(E, S, SSD) is the maximum dose along the central axis of the field of interest for a given beam energy E, field size S and SSD. The factor

in the denominator has the same meaning and the 10×10 cm^2 open applicator has been set for the normalization. The evaluation of the accuracy of XiO eMC in the water as well as in the heterogeneous phantom has been performed at a single SSD of 100 cm.

Heterogeneous phantom description

We have used the thorax phantom constructed by Seuntjens et *al.* [17], which has densities close to realistic human tissues and appropriate dimensions (see Fig. 4.1). This phantom is composed of three layers of tissue-equivalent materials with thicknesses obtained from averaged measurements on CT-scan of a group of 18 patients performed by the authors. A detailed description (composition and density) of the above phantom can be found elsewhere [15, 17]. This phantom has been scanned and CT-scan data have been introduced in DOSXYZnrc [18] using CTCREATE. Distances have been referred from the lung surface for all calculations, i.e., 1 cm depth is equivalent to 3.3 cm for 8, 12 and 18 MeV (because of 2.3 cm of adipose and polyethylene tissue-equivalent materials on top of that surface). Due to the shortest range of lower electron beam energy, calculations have been performed in the thorax phantom without the first 1.1 cm layer of polyethylene material in the case of the 4 MeV electron beam irradiation. Thus, 1 cm from the lung surface was equivalent to 2.2 cm from the top of the phantom surface. The 4 MeV electron beam is obviously not of clinical interest for chest wall irradiation, but this energy was chosen to evaluate the accuracy of XiO eMC for low electron beams irradiation. The accuracy of XiO eMC in the presence of heterogeneities has been investigated from off-axis profile and PDD calculations in the thorax phantom described above and results were compared with the reference BEAMnrc data at one SSD of 100 cm. In the lung tissue, calculations have been carried out at several depths from the lung surface, spaced by 0.5 cm for 4 MeV, 0.6 cm for 8 and 12 MeV, and 1 cm for 18 MeV beam energies. Off-axis profiles have also been calculated in the non-lung tissue (1.2 cm-thick of PMMA) at -0.6 cm from the lung surface. In the above selected depths, hot and cold spots are more pronounced. Therefore,

the evaluation of the ability of XiO eMC to reproduce dose perturbation due to ribs inhomogeneities, which are narrow, compared to the field size, can be considered as a severe test at these depths. The field sizes have been 6×6 cm^2, 10×10 cm^2 and 14×14 cm^2 open applicators. This has enabled the quantification of both the effect of heterogeneities in dose distributions in the lung and non-lung tissues, and the accuracy of XiO eMC in reproducing dose perturbations in the presence of heterogeneities of high density such as bone structures irradiated with electron beam. The normalization has been performed at the average dose, D_{av}, as follows: For each field size at the depth of interest, let D_{max} be the average maximum dose between two ribs and D_{min} the average minimum dose beneath the ribs. D_{max} and D_{min} are calculated from equations (4.2) and (4.3) given below

$$D_{max} = \left(\frac{1}{m}\right) \sum_{j=1}^{m} D_{max}(j) \tag{4.2}$$

$$D_{min} = \left(\frac{1}{m-1}\right) \sum_{j=1}^{m-1} D_{min}(j) \tag{4.3}$$

where "m" is the number of maximum peaks dose involved in each field size at the depth of interest. The normalization has been performed at the average dose D_{av}=(D_{max}+D_{min})/2.

4.2.2 Monte Carlo simulations

Monte Carlo simulation model of the ELEKTA SL25 linear accelerator

A MC model of an ELEKTA SL25 linear accelerator has been built for 4, 8, 12 and 18 MeV electron beams, using the popular MC code BEAMnrc, an EGSnrc-based radiotherapy simulation package. A detailed description of the simulation process can be found in our early work [15] aimed on the evaluation of VMC++ MC based TPS using experimental measurements and the BEAMnrc MC simulation. So that, this part will be briefly presented, with the emphasis being on the differences between the two works, namely,

the number of history and the electron beam spectra parameters. In this work, new models have been built in order to "match" the measured and calculated depth dose in the water phantom. To this end, the mean energy and full width at half maximum (FWHM) have been slightly adjusted. The above parameters are summarized in Table 4.1. The code has been run repeatedly by varying these two parameters until the difference between measured and BEAMnrc calculated depth dose parameter R_{50}, representing the beam quality, was less than 0.5 mm. About (0.6-2)$\times 10^9$ particle histories have been simulated in BEAMnrc and DOSXYZnrc, depending on the energy and field size in order to keep a statistical uncertainty under 0.5% for all calculations (depth dose as well as off-axis profile). (3-400)$\times 10^6$ particles (photons and electrons) were stored in the constructed phase space files. For both BEAMnrc and DOSXYZnrc codes, the CPU time per history depends on energy, field size as well as parameters of simulation.

4.2.3 XiO Electron Monte Carlo dose calculation

The XiO is a new commercial TPS developed by ECMSSG. An Electron Monte Carlo (eMC) algorithm has been incorporated into the XiO TPS as a powerful choice for dose calculation with electron beams. The XiO eMC algorithm is based on the original X-ray Voxel MC (XVMC) initially developed by Universitätsklinikum Tubingen [11] to provide raw calculations that involved electron and photon transport for research in the clinical radiotherapy oncology. To be used as eMC dose engine in the XiO TPS, the base code was modified by ECMSSG in order to greatly extend its modeling capabilities. For instance, a flexible and expandable set of primary source modeling routine was developed to provide accurate reproduction of broad variety of incident electron beams' characteristics. An electron fluence function was included in order to account for electron scattering in air. The use of XiO eMC starts with the characterization of the treatment unit from conventional measurements. This characterization procedure can be summarized below in three main steps.

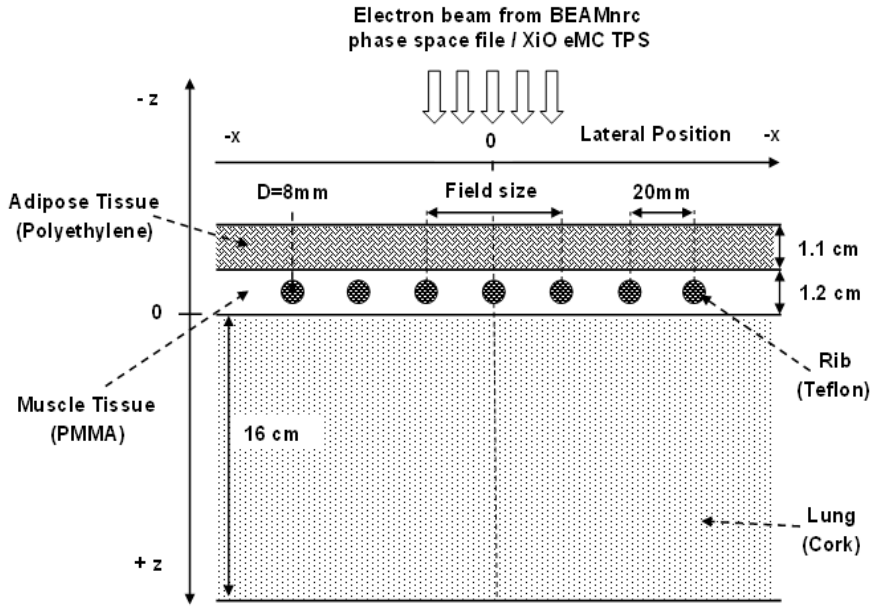

Figure 4.1. Graphic representation of the thorax phantom. It consists of three layers of different tissue-equivalent materials: adipose tissue (polyethylene), striated muscle (PMMA) in which are embedded a series of seven equidistant solid Teflon (ribs), and lung tissue (cork). The radiation beam is interring on the top surface at 100 cm SSD and the beam axis is perpendicular to the central rib axis. 200 MU have been used for all computations and the statistical uncertainty was less than 1% for each calculation.

Collimation geometry

The user has to provide the X- and Y-jaws setting for every combination of energy and applicator. For patient specific applicator (cutout): the material composition, thickness, and distance from the nominal source position of the accelerator to lower surface of the cutout must be provided. The accuracy of XiO eMC depends also slightly on the serial number for a given type of applicator.

Scanning measurements in the water

Scanning measurements with applicator in place

For each energy and applicator at 100 and 115 cm SSD, depth dose and

off-axis profiles at several depths (R_{100}, R_{90}, R_{80}, R_{50}, R_{20} and Rp+2 cm) are required by the manufacturer.

Scanning measurements with no applicator in place

Further measurements (depth dose and lateral dose profiles) with no applicator in position and the jaws opening to 40×40 cm^2, 15×15 cm^2, 10×10 cm^2 and 5×5 cm^2 are needed for each energy. Depth dose and lateral dose profiles have been used to determine the energy spectrum and off-axis fluence variations of the beam, respectively.

Table 4.1. Energy spectrum parameters of electron beams used for the BEAMnrc simulation. FWHM = full width at half maximum. Parameters of smaller peaks sometimes introduced in the spectrum are omitted here.

Nominal energy (MeV)	Peak energy (MeV)	FWHM (MeV)
4	4.85	1.45
8	8.59	2.0
12	13.15	2.62
18	18.71	2.90

Non-scanning measurements in the water

Before clinical use, the electron output produced by external beam radiotherapy machines must be calibrated. This is one of the important steps constituting the chain representing an accurate dose delivery to the patient. The calibration has been performed at reference depth, Z_{ref} (Z_{ref}=0.6R_{50}-0.1 cm), according to the NCS Report 18 protocol [19]. As XiO eMC calculates the absolute dose to the medium, a direct representation of the dose in terms of monitor unit (MU) for a given applicator in a specific electron beam requires an absolute dose measurement for a fixed number of MU. Measurements have been performed at 100 and 115 cm SSD for the four open applicators 6×6 cm^2, 10×10 cm^2, 14×14 cm^2, 20×20 cm^2 and the 5×5 cm^2 insert cutout within the 14×14 cm^2 applicator. These data have been

used to model the amount of scatter in the beam.
All the above data have been collected by ECMSSG which performs the characterization of the radiation treatment unit. In this process, beams are "tuned" by the manufacturer and the user is provided with a ready-to-use virtual treatment unit.

4.2.4 User control parameters affecting the accuracy of XiO eMC dose calculation

There are three parameters that XiO eMC user can modify to qualitatively improve the final result during the patient dose calculation, namely:

(1) The number of history that can be manually fixed and changed, with a maximum value of 1.0E+12, until the isodose lines are smooth;

(2) The mean relative statistical uncertainty (MRSU). As specified in the user manual, the MRSU fixes the largest average uncertainty the user is willing to accept for the final dose calculation. XiO eMC will generate as many histories as necessary to achieve the MRSU value set by the user (as long as it is not more than maximum number of history allowed). The manufacturer advises typical values in the range between 1% and 2%, although, smaller values which require a long computation time can be set. In the present study, we fixed the MRSU at 0.5% and checked periodically when isodose lines were smoothed before stopping calculation;

(3) The voxel size. This parameter can be independently set for each one of the three directions.

4.3 Results

4.3.1 Homogeneous water phantom calculations

Central axis depth dose and off-axis profiles

After the fine-tuning of the primary electron spectrum energy, simulations

have been performed to verify the BEAMnrc MC models with respect to measured dose distributions in the water. The verification has been done by comparing depth dose and off-axis profiles obtained from BEAMnrc models and measurements in a homogeneous water phantom. The accuracy of XiO eMC calculation in the water phantom has been investigated by similar comparisons. The results for depth dose profiles corresponding to 4, 8, 12 and 18 MeV for open field sizes of 10×10 cm^2 and 14×14 cm^2 are displayed in Fig. 4.2 (a, b), respectively. Agreement of R_{50} representing the beam quality (see Table 4.3), i.e. the difference between calculations and measurements was better than 0.5 mm for both BEAMnrc and XiO eMC. Similar results have been obtained for the open 6×6 cm^2, 20×20 cm^2 applicators and other insert cutouts. Off-axis profiles in the inplane and crossplane directions at the depth of maximum dose [see Fig. 4.3 (a, b)] and other depths R_{90}, R_{80}, R_{50}, R_{20} have also been calculated with both codes and compared to measurements. Their agreement with measurements is better than 0.5 mm in the penumbra region and less than 1% in the homogeneous region. However, in the case of 4 MeV, some limitations of XiO eMC values to match lateral dose profiles near the field edge are evident for the open applicators 14×14 cm^2 (Fig. 4.3a) in both directions, and 20×20 cm^2 in the inplane direction, respectively. Table 4.3 summarizes the above results for a depth dose profile comparison of the R_{50} parameter. We also found good agreement (discrepancies of 0.5 mm or less) for the depths of maximum dose computation (BEAMnrc, XiO eMC) relative to the measurements.

Output factors comparison

As XiO eMC computes absolute dose for a fixed number of MU, we have compared experimental and predicted XiO eMC output factors, for open applicators of 6×6 cm^2, 10×10 cm^2, 14×14 cm^2 and 20×20 cm^2 and several highly asymmetric insert cutouts. The accelerator is calibrated to deliver 1 cGy/MU at R_{100} and output factors have been measured according to the NCS Report 18 calibration protocol [19]. The 10×10 cm^2 open applicator has been set as the reference field for normalization. Before performing calcula-

tions, the absolute dose predicted from XiO eMC has been firstly compared to the calibrated one in the reference conditions. As presented in Table 4.2, agreement is under 0.8% with a maximum discrepancy at 4 MeV. Moreover, output factors calculated with XiO eMC for opened field size of 6×6 cm^2, 14×14 cm^2 and 20×20 cm^2 and several highly asymmetric insert cutouts have been compared with measurements for all energies. As expected, we have found good coincidence between XiO eMC and measurements for all open applicators (differences are below 1%). A comparison between measured cutout factors and those predicted from BEAMnrc simulation as well XiO eMC calculation is shown in Tables 4.4 and 4.5. XiO eMC predicts worse results at lower electron beam energy in the most cases.

Table 4.2. Absolute dose per monitor units (MU) calculated with XiO eMC in the homogeneous water phantom in the reference conditions. Computations have been performed for a standard field size of 10×10 cm^2 at 100 cm SSD.

Nominal energy (MeV)	**Dose (cGy/MU)**
4	0.992
8	1.001
12	1.000
18	1.006

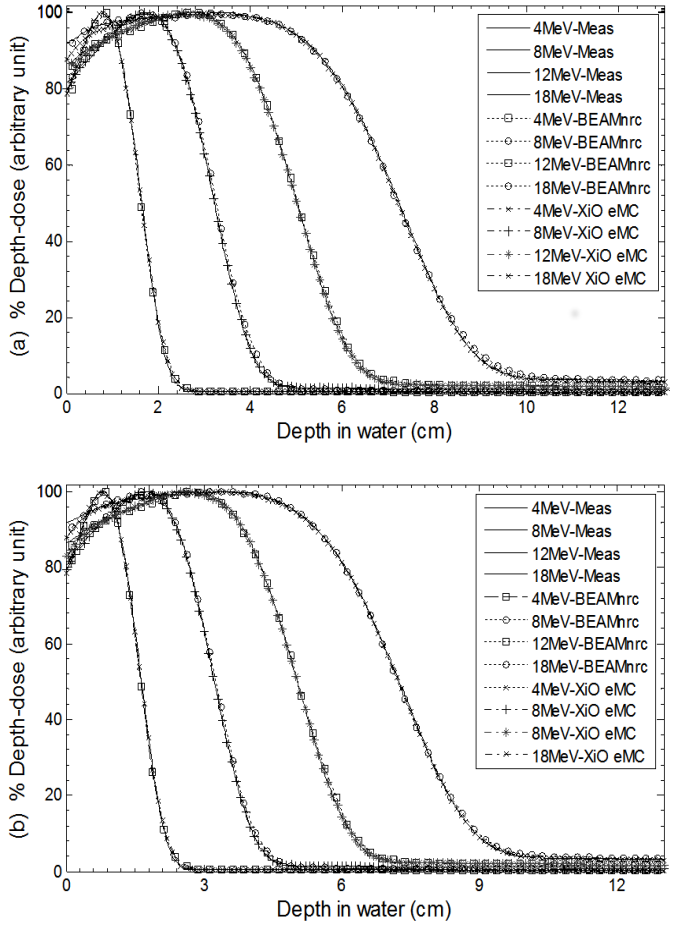

Figure 4.2. Central axis depth dose curves for 10×10 cm^2 (a) and 14×14 cm^2 (b) field size for 4, 8, 12 and 18 MeV at 100 cm SSD. Measurements (Meas) are compared to XiO TPS (XiO eMC) and BEAMnrc values. The normalization has been performed at the depth of maximum dose along the central axis.

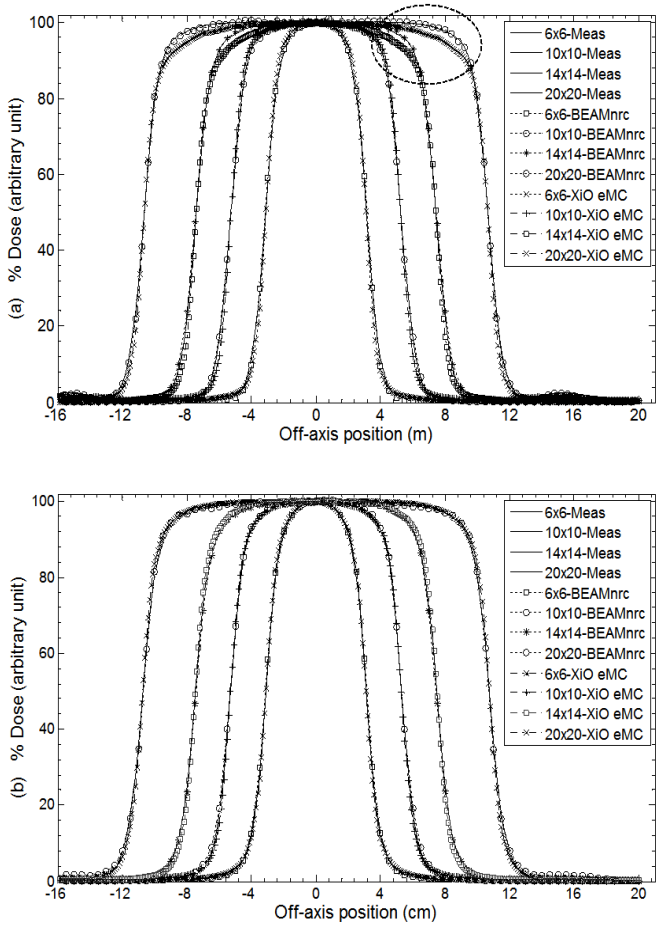

Figure 4.3. Off-axis profiles (crossplane direction) for four open field sizes of 6×6 cm^2, 10×10 cm^2, 14×14 cm^2 and 20×20 cm^2 at 100 cm SSD. Comparison between measurements (Meas), BEAMnrc simulation and XiO eMC for 4 MeV (a) and 8 MeV (b) electron beam energies. The depth of comparison in the water phantom is the depth of maximum dose along the central axis. Data have been normalized at this depth.

Table 4.3. Comparison of R_{50} between BEAMnrc/XiO eMC values and measurements (Meas) at 100 cm SSD. Diff.1=(Meas-BEAMnrc) and Diff.2 =(Meas-eMC). Good coincidence was achieved between BEAMnrc computations measurements as well as between XiO eMC calculations and measurements.

Field size	**4 MeV/R_{50} (cm)**			**8 MeV/R_{50} (cm)**			**12 MeV/R_{50} (cm)**			**18 MeV/R_{50} (cm)**		
(cm^2)	Meas	Diff.1	Diff.2	Meas	Diff.1	Diff.2	Meas	Diff.1	Diff.2	Meas	Diff.1	Diff.2
6×6	1.71	-0.03	-0.05	4.88	-0.03	-0.08	6.77	0.01	0.01	0.01	0.01	0.01
10×10	1.71	-0.03	-0.05	4.88	-0.03	-0.08	6.77	0.01	0.01	0.01	0.01	0.01
14×14	1.71	-0.03	-0.05	4.88	-0.03	-0.08	6.77	0.01	0.01	0.01	0.01	0.01
20×20	1.71	-0.03	-0.05	4.88	-0.03	-0.08	6.77	0.01	0.01	0.01	0.01	0.01

Thesis submitted in fulfilment of the requirements for the degree of "Docteur en Sciences Médicales - Orientation : Physique Médicale" - september 11, 2012.

Table 4.4. Comparison between measured (Meas) and calculated output factors for 4 and 8 MeV electron beams. Dif.1=[(Meas-BEAMnrc)/Meas], Dif.2=[(Meas-XiO eMC)/Meas] and Field Z.=field size.

Field Z.	**Insert**	**4 MeV**			**8 MeV**		
(cm^2)	(cm^2)	Meas	Dif.1 (%)	Dif.2 (%)	Meas	Dif.1 (%)	Dif.2 (%)
6×6	5×2.5	0.762	**3.24**	**4.19**	0.892	1.90	1.34
10×10	2.5×5	0.929	1.45	0.55	0.922	0.32	**2.17**
14×14	5×5	1.036	-1.93	-1.86	0.979	-1.63	0.92
	3×8	1.042	1.06	**4.22**	0.943	-1.25	0.34
	5×10	1.035	0.97	-0.77	1.050	-1.30	1.25
20×20	6×16	1.020	1.08	**-3.71**	0.991	0.20	-1.92
	10×16	1.024	1.27	**-3.42**	1.003	1.29	-0.26

Table 4.5. Comparison between measured (Meas) and calculated output factors for 12 and 18 MeV electron beams. Dif.1=[(Meas-BEAMnrc)/Meas], Dif.2=[(Meas-XiO eMC)/Meas] and Field Z.=field size.

Field Z.	**Insert**	**12 MeV**			**18 MeV**		
(cm^2)	(cm^2)	Meas	Dif.1 (%)	Dif.2 (%)	Meas	Dif.1 (%)	Dif.2 (%)
6×6	5×2.5	0.914	1.28	-1.31	0.941	1.83	-1.53
10×10	2.5×5	0.908	0.67	-0.55	0.973	-1.78	1.68
14×14	5×5	0.964	-1.03	-0.73	0.980	1.36	1.33
	3×8	0.939	-0.73	1.06	0.979	1.92	**2.35**
	5×10	0.967	0.41	-1.34	0.999	-0.70	**-2.43**
20×20	6×16	0.956	-0.26	-1.78	0.966	0.38	-0.62
	10×16	0.961	-0.21	-1.98	0.974	-0.9	0.31

4.3.2 Heterogeneous thorax phantom calculations

Percentage depth dose comparison

Percentage depth dose have been calculated with XiO eMC and compared to those predicted from BEAMnrc simulation for three open applicators of 6×6 cm^2, 10×10 cm^2 and 14×14 cm^2. The comparison has been made for the four energies of 4, 8, 12 and 18 MeV at 100 cm SSD. Results presented

in the Fig. 4.4 (a, b) show a good match between both calculations in the case of 4 MeV (a) and 18 MeV (b). Similar agreement has been observed for 8 and 12 MeV electron beam energies.

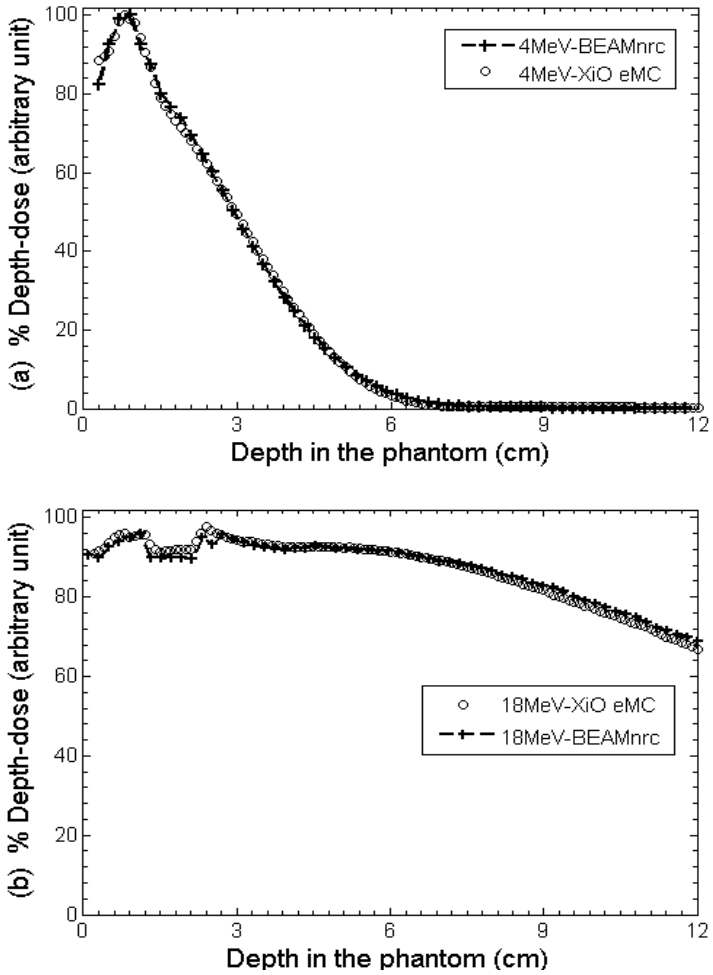

Figure 4.4. Comparison of central axis depth dose curves in the heterogeneous phantom for 4 MeV (a) and 18 MeV (b). Field size 10×10 cm^2. Data have been normalized at the depth of maximum dose along the central axis for 4 MeV. For the 18 MeV, data have been normalized relative to the maximum dose along the central axis in the homogeneous water phantom of the corresponding field size.

Off-axis profile in the non-lung tissue

The evaluation of XiO eMC to accurately reproduce dose distribution in the non-lung tissue has been investigated from off-axis profile computation in the muscle tissue (1.2 cm-thick of PMMA) at - 0.6 cm from the lung surface. Calculations were carried out for the four energies involved 4, 8, 12 and 18 MeV at 100 cm SSD. The field sizes were 6×6 cm^2, 10×10 cm^2 and 14×14 cm^2 open applicators. We have found very good coincidence between XiO eMC and BEAMnrc set as reference, for calculation with 8, 12 and 18 MeV (differences are less than 1%). Fig. 4.5 (a, b) shows a comparison between both computations for 8 MeV (a) and 12 MeV (b). At 4 MeV XiO eMC results are somewhat less accurate (differences up to 4% were observed).

Off-axis profile in the lung tissue

The ability of XiO eMC to accurately predict dose perturbation in the presence of heterogeneities has been investigated in the lung tissue. To this end, off-axis profiles in the direction perpendicular to the ribs in the cork material (thorax phantom depicted in Fig. 4.1) simulating lung tissue have been evaluated using XiO eMC and compared with the predicted BEAMnrc models, set as the reference. Computations have been done at several depths from the lung surface located approximately at 0.2 cm beneath the ribs. For each energy and field size, computations have been carried out in depth until where the effect of heterogeneity is less pronounced, namely, 2.0 cm (4 MeV), 1.8 cm (8 MeV), 2.4 cm (12 MeV) and 4 cm (18 MeV). Both in the XiO eMC and BEAMnrc/DOSXYZnrc, voxel size has been set in the same way to 0.25×0.25×0.25 cm^3. We have found similar agreement for 8, 12 and 18 MeV calculations for all field sizes. Fig. 4.6 (a, b) shows a comparison between BEAMnrc and XiO eMC in the case of 10×10 cm^2 open applicator at 8 MeV energy. The latter slightly underestimated the dose between two ribs and overestimated it below the ribs. For the above three energies (8, 12 and 18 MeV), discrepancies between BEAMnrc models and XiO eMC are around 2.5% (2.0-2.6% between two ribs and 2.0-2.5% below the ribs). The depths of comparison from the lung surface were 0.6 cm (a) and 1.2 cm (b).

As expected, the agreement is quite good (differences are less than 1.0%) beyond these depths for the three energies. Results are less accurate in the case of 4 MeV, which probably stems from the fact that XiO eMC dose algorithm has been developed for electron beam energies in the range 6-25 MeV. Deviations between BEAMnrc and XiO eMC lie within 2.0-3.5% between two ribs as well as below the ribs. Large deviations have been found at the large field size of 14×14 cm^2. The depth of comparison is 0.5 cm from the lung surface. At 1 cm to this surface, the above deviations decrease slightly within 2.0-2.4%. As expected, the accuracy of XiO eMC can be improved with the number of histories generated. In the present study, the number of histories needed to obtain smooth isodose lines (statistical uncertainty less than 1% in all cases) depends on energy, field and voxel sizes. Typical values in the range of (3-20)×10^7 histories were used for all energies and field sizes investigated. No much qualitative improvement to the dose distribution has been found beyond these numbers of histories. We have studied the accuracy of XiO eMC with additional voxel size variation, i.e. 0.55×0.55×0.55 cm^3, 0.45×0.45×0.45 cm^3, 0.35×0.35×0.35 cm^3 and 0.15×0.15×0.15 cm^3 for all previous electron beam energies. The general trend is that the accuracy of XiO eMC increases with the decrease of the voxel size. In the case of 8 MeV (field size 10×10 cm^2) at 0.6 cm depth, deviations up to 4.5% have been found for calculations with the sizes of 0.55×0.55×0.55 cm^3 and 0.45×0.45×0.45 cm^3. Similar behavior has been found for calculations performed with 4, 12 and 18 MeV electron beam energies. Changing the voxel size from 0.25×0.25×0.25 cm^3 to 0.15×0.15×0.15 cm^3 does not significantly affect the accuracy of XiO eMC. Deviations between the two calculations are less than 0.8% for 10×10 cm^2 open applicator at the depths of comparison of 0.5 cm (4 MeV), 0.6 cm (8 and 12 MeV) and 1 cm (18 MeV). As XiO eMC uses several simplifications to speed up calculations, we compared the CPU times between BEAMnrc simulation and XiO eMC in the heterogeneous phantom calculation, for three field sizes of 6×6 cm^2, 10×10 and 14×14 cm^2. However, this is a rough estimation since calculations have been performed on personal computers (PCs) with different characteristics.

BEAMnrc models have been built under a Mandriva 2010.2 operating system with g77 compiler installed on a cluster composed with a set of five connected computers. Each computer was equipped with a double processor Xeon 3.0 GHz and 2.0 GB RAM, whereas, XiO eMC engine has been installed on a virtual machine (VMware Player 4.0.3) installed on a PC with a processor Intel(R) Core(TM) i5, 3.47 GHz and 4.0 GB RAM. About 80% of CPU times indicated for BEAMnrc simulation has been devoted to the generation of the phase space file. Results summarized in the Table 4.6 show clearly that XiO eMC is faster than BEAMnrc user code, while maintaining a level of accuracy which is clinically acceptable.

Table 4.6. Comparison of CPU times in hours (h) between BEAMnrc and XiO eMC calculations in the heterogeneous phantom for the entire dose distribution (PDD and lateral dose profile) with a voxel size of 0.25×0.25×0.25 cm^3 and a treatment distance of 100 cm SSD.

Field size	**4 MeV/CPU Times (h)**		**8 MeV/CPU Times (h)**		**12 MeV/CPU Times (h)**		**18 MeV/CPU Times (h)**	
(cm^2)	BEAMnrc	XiO eMC	BEAMnrc	XiO eMC	BEAMnrc	XiO eMC	BEAMnrc	XiO eMC
6×6	158	0.28	386	0.47	592	1.05	721	0.92
10×10	446	0.35	540	0.65	634	1.15	761	1.28
14×14	460	0.48	560	0.67	792	1.35	787	1.58

Thesis submitted in fulfilment of the requirements for the degree of "Docteur en Sciences Médicales - Orientation : Physique Médicale" - september 11, 2012.

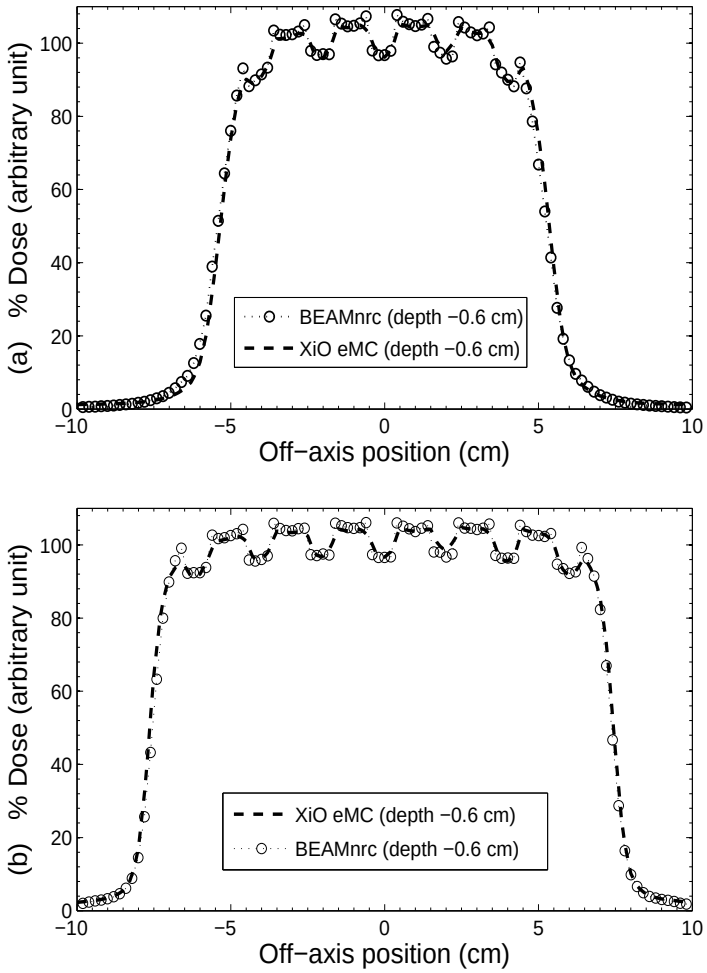

Figure 4.5. Off-axis profiles in the muscle tissues (1.2 cm-thick of PMMA) in the crossplane direction at 100 cm SSD. Comparison between BEAMnrc simulation and XiO eMC for 8 MeV and 10×10 cm^2 field size (a), 12 MeV and 14×14 cm^2 field size (b).

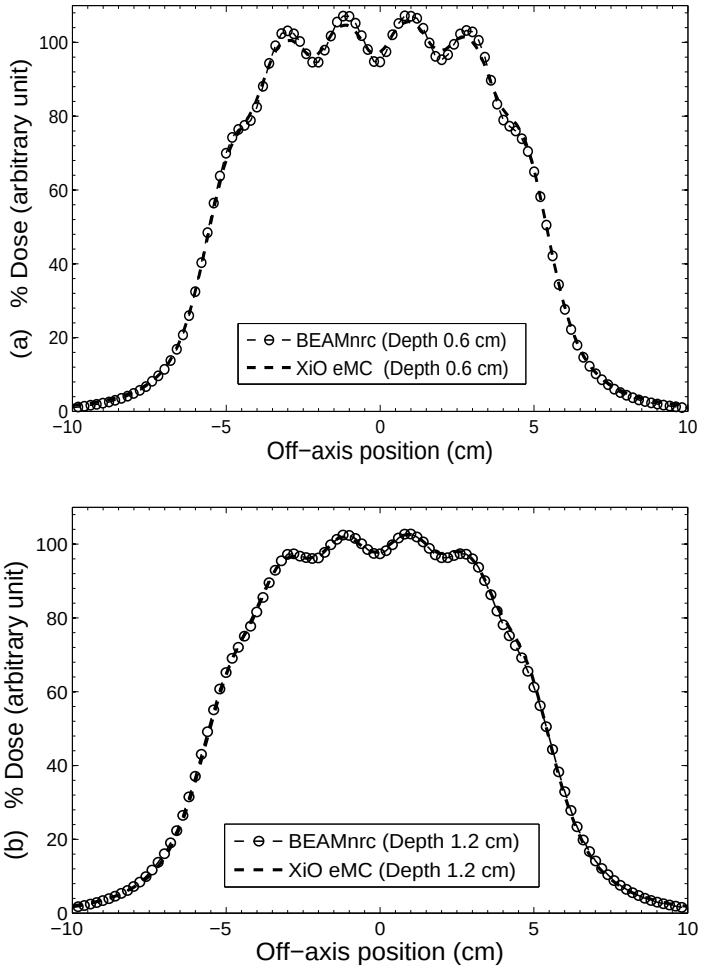

Figure 4.6. Off-axis profiles in the lung tissue, in the crossplane direction for an open field size of 10×10 cm^2 at 100 cm SSD. XiO eMC and BEAMnrc are compared for 8 MeV electron beam energy. Depths from the lung surface are 0.6 cm (a) and 1.2 cm (b).

4.4 Discussion and conclusion

All MC calculations in the present study are in very good agreement with measurements data performed in the water phantom, providing a proof of the accuracy of our BEAMnrc models. Discrepancies between BEAMnrc and

measurements are almost always under 2% in the homogeneous dose regions, and 0.5 mm shifting in the high dose gradient regions. These have been our acceptance criteria based on the NCS Report 15 [20] recommendations (2%/2 mm for small dose/large dose gradient in the homogeneous phantom), for MC modeling as well as a prerequisite before considering BEAMnrc models as reference tool in the heterogeneous phantom calculations. Accuracy of XiO eMC is benchmarked for a wide range of electron beam energies of 4, 8, 12 and 18 MeV both in the homogeneous water phantom and heterogeneous phantom. We have compared experimental dose distributions with predicted values from XiO eMC and full MC simulation. For all field sizes that have been tested in the water phantom calculations, a good agreement is found between BEAMnrc/XiO eMC results and measurements for 8, 12 and 18 MeV. Similar accuracy is obtained in the case of 4 MeV, except the large field sizes of 14×14 cm^2 and 20×20 cm^2 for which off-axis profiles do not match measurements near the edge of the field. Note that BEAMnrc models agree well with measurements in these cases. We have also found that XiO eMC can predict MU with good accuracy for open field size. Cutout factors computed with XiO eMC are quite similar to those predicted from BEAMnrc simulation, except at low energy for which the results are worse in the most cases. In the heterogeneous phantom, we have found good coincidence of dose distribution (PDD and lateral dose profile) between BEAMnrc simulation and XiO eMC in the non-lung tissue for 8, 12 and 18 MeV (differences less than 1%). PDD obtained from XiO eMC are in good agreement with BEAMnrc simulation at 4 MeV, while deviations up to 4% were observed for lateral dose profile at the same energy. In the lung tissue, discrepancies between BEAMnrc and XiO eMC are around 2.5% for 8, 12 and 18 MeV and 3.5% for 4 MeV. Results from 4 MeV calculations are not surprising because XiO eMC dose algorithm was developed for electron beam energies range 6-25 MeV. Discrepancies between BEAMnrc and XiO eMC for the other energies may be partially explained from some aspects. Firstly, the depth of comparison is closer to the bone structure where the effects of heterogeneities are more pronounced in that region. A $\pm$ 0.1 cm positional

uncertainty in the depth analysis may lead up to 1% difference in dose. Moving away from the heterogeneity rapidly reduces the disagreement and a good consistency is achieved. Secondly, at this region, scattered electrons from two ribs contribute to the increase in dose (i.e. increase in electron fluence) laterally to both sides of the ribs and the decrease in dose beneath the ribs (i.e. decrease in primary electron fluence). This phenomenon seems not to be well modeled, probably due to simplifying approximations used in the implementation of electrons transport and secondary particles creation in the XiO eMC algorithm. Accuracy of XiO eMC can be improved by decreasing the voxel size. However, reducing it from $0.25\times0.25\times0.25$ cm^3 to $0.15\times0.15\times0.15$ cm^3 does not lead to significant change in accuracy. Thus, the reduction of the voxel size does not indefinitely improve XiO eMC dose calculation. We have found that the size $0.55\times0.55\times0.55$ cm^3 can be considered as large and leads to wrong results. A typical voxel size in the range $0.25\times0.25\times0.25$ cm^3 - $0.35\times0.35\times0.35$ cm^3 can be considered as acceptable for dose calculation. However, smaller voxel sizes should be selected for the calculations of dose distribution in some critical situations where three-dimensional heterogeneities are always encountered (e.g. in head and neck area).

A Similar study has been reported by Edimo et *al.* [15] on the commissioning of Oncentra MasterPlan TPS (OMTPS) which implements a VMC++ Kawrakov' algorithm [7, 8] for two electron beam energies, 4 and 12 MeV. The Similarities between the two studies are:

(a) the use of the same heterogeneous phantom and commissioning approach;

(b) the calculations depths are identical for 4 MeV and comparable for 12 MeV.

The ability of both TPSs to predict dose perturbation is compared here for the above two energies. For 4 MeV, at the same depth, both TPSs predict dose perturbation caused by ribs heterogeneities with similar accuracy. However, XiO eMC is more robust in the case of 12 MeV. Deviations range from 2.0-4.0% for OMTPS and they are less than 1% for XiO eMC at comparable depths. Moreover, the capability for the user control over the voxel size is

a good feature compared to OMTPS in which it is automatically assigned by the system. However, as mentioned in the MC simulation paragraph, the BEAMnrc Peak energy and FWHM are different between the two works, which could limit our findings in the above comparison. The classic paper of Van Dyk et *al.* [21] suggests that an electron dose calculation engine should achieve 2% accuracy along the central axis ray (except around the dose maximum region) and 4%/4 mm accuracy throughout the dose distribution. The goal of ECMSSG was to exceed those criteria and to achieve 2%/2 mm accuracy throughout most of the dose distributions. In view of our results, the above criteria have been achieved in the homogeneous phantom calculations. Deviations observed between BEAMnrc and XiO eMC in the heterogeneous phantom are close to these criteria of acceptability for the most tested dose distribution, demonstrating the reliability of using XiO eMC 4.60 for planning treatment of cancer patients with electron beams. However, significant deviations found in the case of 4 MeV electron beam calculations with XiO TPS demonstrate the need to be careful when using XiO at lower electron beam energies.

Acknowledgments

This work was partly supported by the ICTP through CEPAMOQ (OEA-AC-71 project) at the University of Douala (Cameroon) and the Fellowships Program of the "Agence Universitaire de la Francophonie (AUF)". The authors are greatly indebted to the radiation oncology physicists J. M. Denis and A. Delor of the Radiotherapy Department of Cliniques Universitaires Saint-Luc (Brussels, Belgium) for their help in measurements performed in the water phantom and wish to thank M. Coevoet for his technical support during the entire work. Finally, we are also grateful to the referees for their pertinent comments and helpful suggestions which have been used in this work.

4.5 Bibliography

[**1**] Mackie TR. Applications of the Monte Carlo method in radiotherapy. In: The Dosimetry of Ionizing Radiation 3, editors Kase KR, Bjamgard BE, Attix FH (San Diego, CA: Academic); 1990. p. 541-620.

[**2**] Mohan R, Antolak J. Monte Carlo techniques should replace analytical methods for estimating dose distributions in radiotherapy treatment planning. Med Phys 2001;28:123-26.

[**3**] Rogers DWO, Bielajew AF. Monte Carlo techniques of electron and photon transport for radiation dosimetry. In: The Dosimetry of Ionizing Radiation 3, editors Kase KR, Bjamgard BE, Attix FH (San Diego, CA: Academic); 1990. p. 427-539.

[**4**] Rogers DWO. The role of Monte Carlo simulation of electron transport in radiation dosimetry. Int J Radiat Appl Instrum 1991; A42: 965-74.

[**5**] Rogers DWO, Faddegon BA, Ding GX, Ma CM, We J, Mackie TR. BEAM: a Monte Carlo code to simulate radiotherapy treatment units. Med Phys 1995;22:503-24.

[**6**] Kawrakow I. Accurate condensed history Monte Carlo simulation of electron transport. I. EGSnrc, the new EGS4 version. Med Phys 2000; 27:485-98.

[**7**] Kawrakow I, Fippel M. VMC++, a fast MC algorithm for radiation treatment planning. In: XIII international conference on the use of computers in radiation therapy. Heidelberg, Germany: Springer-Verlag; 2000. p. 126-8.

[**8**] Kawrakow I. VMC++, electron and photon Monte Carlo calculations optimized for radiation treatment planning. In: Kling LA, Barao F, Nakagawa M, Tavora L, Vaz P, editors. Advanced Monte Carlo for radiation physics, particle transport simulation and applications: proceeding of the Monte Carlo 2000 meeting. Berlin: Springer; 2001. p. 229-36.

[**9**] Kawrakow I, Fippel M. Investigation of variance reduction techniques for Monte Carlo photon dose calculation using XVMC. Phys Med Biol 2000;45:

2163-83.

[**10**] Fippel M, Kawrakow I, Friedrich K. Electron beam dose calculations with the VMC algorithm and the verification data of the NCI working group. Phys Med Biol 1997;42:501-20.

[**11**] Fippel M. Fast Monte Carlo dose calculation for photon beams based on the VMC electron algorithm. Med Phys 1999;26:1466-75.

[**12**] Ma CM, Li JS, Pawlicki T, Jiang SB, Deng J, Lee MC, et al. A Monte Carlo dose calculation tool for radiotherapy treatment planning. Phys Med Biol 2000;47:1671-89.

[**13**] Cygler JE, Daskalov GM, Chan GH, Ding GX. Evaluation of the first commercial Monte Carlo dose calculation engine for electron beam treatment planning. Med Phys 2004;31:142-53.

[**14**] Ma CM, Mok E, Kapur A, Pawlicki T, Findley D, Brain S, et al. Clinical implementation of a Monte Carlo treatment planning system. Med Phys 1999;26:2133-43.

[**15**] Edimo P, Clermont C, Kwato MG, Vynckier S. Evaluation of a commercial VMC++ Monte Carlo based treatment planning system for electron beams using EGSnrc/BEAMnrc simulations and measurements. Physica Medica 2009;25:111-21.

[**16**] Andreo P, Burns DT, Hohlfeld K, Huq MS, Kanai T, Laitano F, et al. Absorbed dose determination in external beam radiotherapy: an International Code of Practice for dosimetry based on standards of absorbed dose to water. IAEA TRS 398:2000.

[**17**] Seutjens J, Van der Plaetsen A, Thierens H, Piessens M. Comparison of measured and calculated dose distributions in lung after electron beam treatment of the chest wall. Med Phys 1994;21:1959-68.

[**18**] Walters BRB, Rogers DWO. DOSXYZnrc User Manuel, National Research Council of Canada, Ottawa, NRCC Report No. PIRS-794 rev A:2004.

[**19**] Aalbers AHL, Hoornaert MT, Minken A, Palmans H, Pieksma MWH, De Prez LA, et al. Code of Practice for the Absorbed Dose Determination in High Energy Photon and Electron Beams. NCS Report 18 2008;23-29.

[**20**] Bruinvis IAD, Keus RB, Lenglet WJM, Meijer GJ, Mijnheer BJ, Van't Veld AA, et al. Quality assurance of 3-D treatment planning systems for external photon and electron beams: Practical guidelines for acceptance testing, commissioning and periodic quality control of radiation therapy treatment planning systems. NCS Report 15 2006.

[**21**] Van Dyk J, Barnett RB, Cygler JE, Shragge PC. Commissioning and quality assurance of treatment planning computers. Int J Radiat Oncol Biol Phys 1993;26:261-73.

Chapter 5

Discussion-conclusion and Future prospects

5.1 Discussion

The accuracy of dose calculation is essential in the radiation planning process if one needs to reduce the overall uncertainty to the dose delivered to the patient. The ability of available analytical dose computation models to accurately reproduce dose distribution for radiotherapy treatments planning is limited. Deviations from true dose distributions are often clinically significant in many cases [1-6]. During the last decade, many efforts have been devoted on the improvement of dose calculation algorithms implemented in the TPSs in order to reproduce all beam geometries, beam modification devices and to account for the effects of inhomogeneities in the 3D patient geometry. To this end, MC methods have proven to be the most accurate way of performing patient dose calculation [2, 7-17].
In the present work, BEAMnrc MC models have been built for electron beams of 4, 8, 12 and 18 MeV delivered by an ELEKTA SL25 medical linear accelarator. As application, the above models have been used for the clinical evaluation of two commercial electron MC based TPSs, OMTPS and XiO eMC. A new approach based the validation on three steps is presented,

namely:

(a) Validation in the homogeneous water phantom;

(b) Validation in the heterogeneous phantom simulating the patient chest wall using film measurements;

(c) Validation through a benchmarking with full MC simulation using the EGSnrc/BEAMnrc MC models.

In the following subsections, we summarize results obtained in the homogeneous as well as in the heterogeneous phantom. A comparison between both TPSs (XiO eMC, OMTPS) with their integrated PBA is presented for computations performed in the homogeneous water phantom and in the heterogeneous phantom, followed by a brief discussion.

5.1.1 Homogeneous water phantom validation

Considering the results obtained in the homogeneous water phantom (PDD and lateral dose profiles), we can conclude that both TPSs are suitable for their use in the homogeneous media at the SSD of 100 cm, for all open field sizes and energies investigated. In this context, OMTPS and XiO eMC TPSs do not provide a significative added value compared to pencil beam implemented into both TPSs. This is also valid for output factors calculated for large open field sizes. In the case of small or highly asymmetric inserts cutouts presented in the table 5.1 for OMTPS, results obtained from PBA (HELAX-TMS) implemented in the OMTPS show large divergences with measurements whereas those predicted from the voxel MC (VMC++) algorithm are much closer to measurements in the most cases. The large deviations between measurements and the PBA HELAX-TMS can be explained from the small angle approximation inherent to this class of algorithm. In fact, electrons scattered at large angles into the insert (and even in the water phantom) are not considered for the dose scoring at the point of calculation. This scattered effect is more pronounced for small field sizes

Table 5.1. Comparison between measured (Meas) and calculated output factors for 4 and 12 MeV electron beams. Dif.1=[(Meas-OMTPS)/Meas], Dif.2=[(Meas-PBA)/Meas] and PBA=HELAX-TMS.

Applicator	**Insert**	**4 MeV**			**12 MeV**		
(cm^2)	(cm^2)	Meas	Dif.1 (%)	Dif.2 (%)	Meas	Dif.1 (%)	Dif.2 (%)
6×6	3×3	0.730	**-2.74**	**-7.80**	0.911	**-2.96**	**-4.85**
	5×2.5	0.725	**-2.62**	**-8.60**	0.921	-1.30	-1.61
10×10	3×3	0.897	**-2.56**	**-11.04**	0.914	**2.52**	**-3.58**
	5×2.5	0.904	-1.66	**-9.86**	0.924	-1.41	**-2.23**
	6×6	1.003	-0.50	-0.43	0.983	-0.71	-0.50
20×20	6×6	1.036	0.40	**3.93**	0.974	0.62	**2.44**
	6×16	1.040	-1.57	0.72	0.976	**2.15**	**3.03**
	10×16	1.040	**-2.90**	1.03	0.979	-1.12	-1.59
	10×10	1.046	0.76	0.63	0.977	-0.51	1.72
	14×14	1.055	0.86	0.68	0.976	-0.20	-0.98

and highly asymmetric cutouts than at large field sizes.

Tables 5.2 and 5.3 summarize similar results obtained when comparing output factors measured with those computed with XiO eMC and the PBA available as optional choice for electron dose calculation.

At low energy, 4 MeV, results obtained from both calculations, XiO eMC as well as PBA, are not clinically acceptable in the most cases. They are especially worse for small or highly asymmetric cutouts. At medium energy (8 and 12 MeV) the added value of MC-based TPS clearly appears. Calculations at high 18 MeV electron beam energy show globally similar accuracy.

5.1.2 Heterogeneous phantom validation

Results from the heterogeneous phantom are less accurate in the case of 4 MeV calculation for both eMC-based TPSs (VMC++ and XiO eMC). In the case of OMTPS calculations, deviations (depending on the field size and the depth of measurements) ranged from 0.5-4.0% between two ribs, whereas they were between 0.5 to 4.0% below the ribs. Results from XiO eMC exhibit

similar behavior with percent deviations from 2.0 to 3.5% between two ribs as well as below the ribs. The above results, although still remain clinically unacceptable, represent a major advance with regard to PBA.
High degree of confidence for dose calculation has been achieved at 12 MeV (respectively at 8, 12 and 18 MeV) for OMTPS (respectively for XiO eMC). We found good coincidence between BEAMnrc and XiO eMC for lateral dose profile calculated in the non-lung tissue (1.2 cm-thick of PMMA) for 8, 12 and 18 MeV (deviations are less than 1%), whereas disagreements up to 4% have been observed at 4 MeV electron beam energy. This level of accuracy can not be achieved with PBA, as shown in Fig. 5.1. Both BEAMnrc model and XiO eMC predict the presence of the bone structure in the 1.2 cm-thick of PMMA, while PBA calculates a homogeneous lateral dose profile. This is due to the slab geometry approximation inherent to the PBA.

Table 5.2. Comparison between measured (Meas) and calculated output factors for 4 and 8 MeV electron beams. Dif.1=[(Meas-XiO eMC)/Meas], Dif.2=[(Meas-PBA)/Meas] and Field Z.=field size.

Field Z.	**Insert**	**4 MeV**			**8 MeV**		
(cm^2)	(cm^2)	Meas	Dif.1 (%)	Dif.2 (%)	Meas	Dif.1 (%)	Dif.2 (%)
6×6	5×2.5	0.762	**4.19**	-0.56	0.892	1.34	**-7.86**
10×10	2.5×5	0.874	0.55	**-13.90**	0.922	**2.17**	**-8.12**
14×14	5×5	1.036	-1.86	-1.19	0.979	0.92	**-2.72**
	3×8	1.042	**4.22**	-0.66	0.943	0.34	**-6.24**
	5×10	1.035	-0.77	-1.35	1.050	1.25	4.29
20×20	6×16	1.020	**-3.71**	**-4.51**	0.991	-1.92	-1.72
	10×16	1.024	**-3.42**	**-4.10**	1.003	-0.26	-0.50

Table 5.3. Comparison between measured (Meas) and calculated output factors for 12 and 18 MeV electron beams. Dif.1=[(Meas-XiO eMC)/Meas], Dif.2=[(Meas-PBA)/Meas] and Field Z.=field size.

Field Z.	**Insert**	**12 MeV**			**18 MeV**		
(cm^2)	(cm^2)	Meas	Dif.1 (%)	Dif.2 (%)	Meas	Dif.1 (%)	Dif.2 (%)
6×6	5×2.5	0.914	-1.31	**-9.61**	0.941	-1.53	**-10.97**
10×10	2.5×5	0.908	-0.55	**-9.12**	1.005	**4.77**	0.72
14×14	5×5	0.964	-0.73	**-2.63**	0.980	1.33	-0.58
	3×8	0.939	1.06	**-4.54**	0.979	**2.35**	0.20
	5×10	0.967	-1.34	**2.17**	0.999	**-2.43**	1.40
20×20	6×16	0.956	-1.78	-1.99	0.966	-0.62	0.31
	10×16	0.961	-1.98	-1.46	0.974	0.31	1.13

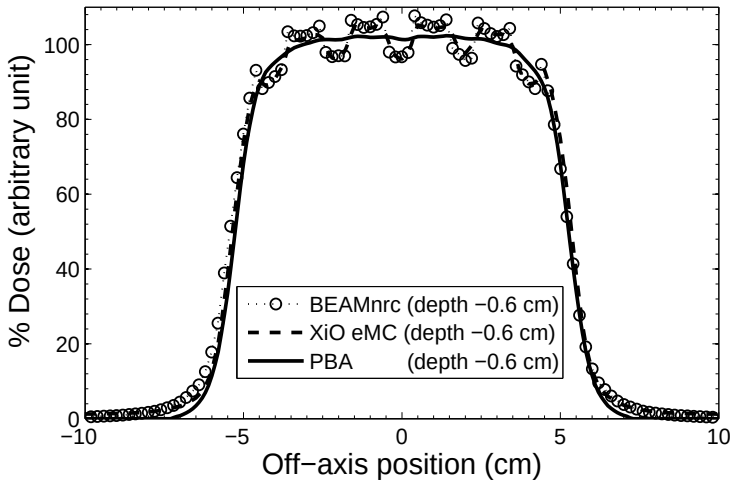

Figure 5.1. Off-axis profiles in the crossplane direction for an open field size of 10×10 cm^2 at 100 cm SSD. PBA is compared to XiO eMC and BEAMnrc for 8 MeV electron beam energy in the non-lung tissue (1.2 cm-thick of PMMA) at -0.6 cm from the lung surface.

5.1.3 Hounsfield values to relative electron densities conversion file

The physical densities (g/cm^3) stated for the heterogeneous phantom described in chapter 3 were not assigned at their exact values in both TPSs,

OMTPS as well as XiO eMC. Instead, we used the CT values to the relative electron densities conversion file of each TPS. However, Calculations have been performed in DOSXYZnrc user MC code with physical densities. In fact, the stand-alone program DOSXYZnrc/CTCREATE uses ramps that allow material and mass density data within each voxel to be derived from the Hounsfield number. This represents a more realistic way for the simulation of an anthropomorphic phantoms and, therefore, improve the accuracy of patients radiation dose calculations. It is therefore expected that some of the differences (difficult to quantify since setting mass density in both TPSs is not possible) observed between computations performed with DOSXYnrc and those performed with both TPSs could be due to these differences in the representation of the phantom (physical density versus relative electron density).

5.1.4 Measurements with KODAK EDR2 film

Although the main results were already discussed in different papers, one additional point of chapter 3 deserves to be reviewed in this section. In fact, the accuracy of OMTPS in the heterogeneous phantom has been performed using full BEAMnrc MC simulation and KODAK EDR2 film measurement. The Fig. 3.5 depicts a comparison of lateral dose profiles (inplane direction) between measurements (KODAK EDR2 Film), BEAMnrc simulation and treatment planning system (OMTPS), for 12 MeV (open field size of 6×6 cm^2 at 100 cm SSD) at different depths. Away from the penumbra region, in the case of 12 MeV, there is a good coincidence between BEAMnrc prediction and OMTPS calculation. However, large discrepancies between both calculations relative to KODAK EDR2 film measurement are evident. The dose seems therefore to be overestimated from KODAK EDR2 film measurement. This has been explained by arguing the higher response of the KODAK EDR2 film away from the penumbra region, but this argument seems to work in the opposite direction of the published data by Gerbi et *al.* [20] which show an under-response at low electron energies compared to higher electron beam

energies. No other explanation about this overestimation of the dose away from the penumbra region has been found.

5.2 Conclusion

Results presented through this work provide a proof of the added value of MC simulation for patient dose calculation. The accuracy of both algorithms are clinically acceptable for 8, 12 and 18 MeV electron beam energies. The use of both TPSs at 4 MeV is not recommended although the results obtained at this energy are better than those that can be predicted with PBA. A new approach combining measurements and full MC simulation, on the commissioning of MC-based TPS has been presented and provides another realistic way to evaluate the accuracy of eMC TPS, although this method needs more computing time and disk space. However, an alternative to overcome these two drawbacks could be the reconstruction of the beam phase space data [18-19]. Furthermore, the development of MC based TPSs is still an ongoing process, thus, our BEAMnrc MC models can be used thereafter for the evaluation of other electron MC based TPSs, especially in the conditions where measurements are limited or impossible (e.g. of measurements of PDD and lateral dose profile measurement in the non-lung tissue in our case).

5.3 Future prospects

An interesting study that could be integrated in the commissioning process is to compare dose distribution (dose plans calculated from patient's CT data) between BEAMnrc models and XiO eMC predictions, for a sample of clinical cases (e.g. of a nasal cavity treatment). Also, our calculations are limited on one SSD of 100 cm and multiple gantry angles have not been concerned. Integrating the above aspects in the commissioning process could provide more confidence on the limits of any eMC algorithm aimed for patient dose calculation.

Recently, our radiation therapy department commissioned a new medical linear accelerator, ELEKTA SP18, an ELEKTA synergy acceleration capable to deliver electron beam of 6, 8, 10, 12 and 18 MeV. These energies were tuned to the one delivered by the SL25 in which this work was performed. The question is: Are the MC models, built for the SL25, valid for the SP18?. This could be an interesting topic to be investigated.
Electron treatment sometimes uses electron beams in combination with photons. In the last past decades, others complex techniques have been introduced such as the electron intensity modulated radiotherapy [21-25] similar to the intensity modulated radiotherapy with photons. The clinical implementation of the above technique requires an extensive verification to ensure the correct target dose delivery into the patient according to ICRU report 60 [26] recommendations. To this end, MC simulation is the best tool beside measurements and our MC Models may be used for this purpose although the simulation of the electron multileaf collimator will be necessary.

5.4 Bibliography

[**1**] Almon SS, Kenneth RH. Pencil-beam redefinition algorithm for electron dose distributions. Med Phys 1991;18:7-18.

[**2**] Cygler J, Battista JJ, Scrimger JW, Mah E, Antolak J. Electron dose distributions in experimental phantoms: a comparison with 2D pencil beam calculations. Phys Med Biol 1987;32:1073-86.

[**3**] Mah E, Antolak J, Scrimger JW, et al. Experimental evaluation of 2D and 3D electron pencil beam algorithm. Phys Med Biol 1989;34:1174-94.

[**4**] Hogstrom KR, Mills MD, Almond PR. Electron beam dose calculations. Phys Med Biol 1981;26:445-59.

[**5**] Hogstrom KR, Mills MD, Meyer JA, et al. Dosimetric evaluation of a pencil-beam algorithm for electrons employing a two-dimensional heterogeneity correction. Int J Radiat Oncol Biol Phys 1984;10:561-69.

[**6**] Ostwald PM, Metcalfe PE, Denham JW, et al. A comparison of three electron planning algorithms for a 16 MeV electron beam. Int J Radiat Oncol Biol Phys 1994;28:731-40.

[**7**] Mackie TR. Applications of the Monte Carlo method in radiotherapy. In: The Dosimetry of Ionizing Radiation 3, editors Kase KR, Bjamgard BE, Attix FH (San Diego, CA: Academic); 1990. p. 541-620.

[**8**] Mohan R, Antolak J. Monte Carlo techniques should replace analytical methods for estimating dose distributions in radiotherapy treatment planning. Med Phys 2001;28:123-26.

[**9**] Rogers DWO, Bielajew AF. Monte Carlo techniques of electron and photon transport for radiation dosimetry. In: The Dosimetry of Ionizing Radiation 3, editors Kase KR, Bjamgard BE, Attix FH (San Diego, CA: Academic); 1990. p. 427-539.

[**10**] Rogers DWO. The role of Monte Carlo simulation of electron transport in radiation dosimetry. Int J Radiat Appl Instrum 1991; A42: 965-74.

[**11**] Rogers DWO, Faddegon BA, Ding GX, Ma CM, We J, Mackie TR. BEAM: a Monte Carlo code to simulate radiotherapy treatment units. Med Phys 1995;22:503-24.

[**12**] Ma CM, Faddegon BA, Rogers DWO, Mackie TR. Accurate characterization of Monte Carlo calculated electron beams for radiotherapy. Med Phys 1997;24: 401-16.

[**13**] Zhang GG, Rogers DWO, Cygler JE, Mackie TR. Monte Carlo investigation of electron beam output factors versus size of square cutout. Med Phys 1999;26:743-50.

[**14**] Kapur A, Ma CM, Mok EC, David OF, Arthur LB. Monte Carlo calculations of electron beam output factors for a medical linear accelerator. Phys Med Biol 1998;43:3479-94.

[**15**] Turian JV, Smith BD, Bernard DA, Griem KL, Chu JC. Monte Carlo calculations of output factors for clinically shaped electron fields. J Appl Clin Med Phys 2004;5:42-62.

[**16**] Pavon EC, Sanchez-Doblado F, Leal A, Capote R, Lagares JI, Perucha M, et al. Total skin electron therapy treatment verification: Monte Carlo simulation and beam characteristics of large non-standard electron fields. Phys Med Biol 2003;48:2783-96.

[**17**] Popescu IA, Shaw CP, Zavgorodni SF, Beckham WA. Absolute dose calculations for Monte Carlo simulations of radiotherapy beams. Phys Med Biol 2005;50:3375-92.

[**18**] Ma CM, Faddegon BA, Rogers DWO, et al. Accurate characterization of Monte Carlo calculated electron beams for radiotherapy. Med Phys 1997;24:401-16.

[**19**] Ma CM, Characterization of computer simulated radiotherapy beams for Monte Carlo treatment planning. Radiat Phys Chem 1998;35:329-44.

[**20**] Gerbi JB, Dimitroyannis DA. The response of Kodak EDR2 film in high-energy electron beams. Med Phys 2003;30:2703-5.

[**21**] Magnus GK, Mikael K, Ma CM. Electron beam collimation with focused and curved leaf end MLCs-Experimental verification of Monte Carlo optimized designs. Med Phys 2002;29:631-7.

[**22**] Magnus GK, Mikael K. Treatment head design for multileaf collimated high-energy electrons. Med Phys 1999;26:2161-7.

[**23**] Magnus GK, Mikael K, Zackrisson B. Intensity modulation with electrons: calculations, measurements and clinical applications. Phys Med Biol 1998;43:1159-69.

[**24**] Lee MC, Jiang SB, Ma CM. Monte Carlo and experimental investigations of multileaf collimated electron beams for modulated electron radiation therapy. Med Phys 2000;27:2708-18.

[**25**] Ma CM, Pawlicki T, Lee MC, Jiang SB, Li JS, Deng J, Yi B, Mok E, Boyer AL. Energy-and intensity-modulated electron beams for radiotherapy. Phys Med Biol 2000;45:2293-311.

[**26**] Prescribing, Recording and Reporting Photon Beam Therapy (Supplement to ICRU Report 50), Rep. 62, ICRU, Bethesda, MD (1999).

Université catholique de Louvain
Faculté de Médecine
Pôle d'Imagerie Moléculaire, Radiothérapie et Oncologie
MIRO-Avenue Hippocrate, 54, bte B1.54.07
1200 Woluwe-Saint-Lambert (Belgique)
Tél. +32 (0) 2 764 54 31-Fax: +32 (0) 2 764 94 25

Université de Douala
Faculté des Sciences
Centre de Physique Atomique Moléculaire et Optique Quantique
B.P. 8580 Douala (Cameroun)
Téléfax: (+237) 33 43 46 08

The present study is focused on the clinical validation of two electron Monte Carlo (eMC) based treatment planning systems (TPS), Oncentra MasterPlan TPS (OMTPS) and XiO eMC. We present a new approach on the commissioning process based on, (a) homogeneous water phantom validation, (b) heterogeneous phantom validation with film measurements and, (c) Full MC validation.

As a first step, MC models of electron beams (4, 8, 12 and 18 MeV) from an Elekta SL25 medical linear accelerator were build using the popular EGSnrc/BEAMnrc user MC code. The calculated dose distributions were benchmarked by a comparison with the measurements made in the water phantom for a wide range of open field sizes and insert combinations, at a single source to surface distance (SSD) of 100 cm. These BEAMnrc models were used to evaluate the accuracy of OMTPS (respectively XiO eMC) for two energies 4 and 12 MeV (respectively for 4, 8, 12 and 18 MeV) in a homogeneous water phantom.

As a second step, the accuracy of both TPSs has been evaluated by comparing dose distributions in a heterogeneous phantom containing ribs structures. Dose distributions in the lung and non-lung tissue predicted from BEAMnrc simulation were compared with those computed with OMTPS and XiO eMC. In the case of OMTPS calculations, differences between BEAMnrc simulation and measurements range from 0.5%-2.0% between two ribs and 0.6%-1.0% below the ribs, whereas the range difference between OMTPS and measurements was the same (0.5-4.0%) in both areas. BEAMnrc models have been set as reference in the case of XiO eMC computation and the overall agreement between the two schemes lies under 2.5% for the most tested dose distributions at 8, 12 and 18 MeV and is better than the 4 MeV one.

The present work demonstrates the added value of MC TPS compared to pencil beam algorithms. Results show that OMTPS and XiO eMC can predict dose perturbation induced by high-density heterogeneities for the electron beam energies investigated, except at 4 MeV electron beam energy in which significant deviations have been found with both algorithms. This demonstrates that caution is necessary in using both TPSs at low energies.